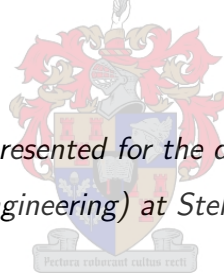


**COUPLED FULLY THREE-DIMENSIONAL
MATHEMATICAL MODELLING OF SEDIMENT
DEPOSITION AND EROSION IN RESERVOIRS**

by

Ousmane Sawadogo

*Dissertation presented for the degree of Doctor of
Philosophy (Engineering) at Stellenbosch University*



Promoter:

Prof. G.R. Basson

March 2015

Declaration

By submitting this dissertation electronically, I declare that the entirety of the work contained therein is my own, original work, that I am the sole author thereof (save to the extent explicitly otherwise stated), that reproduction and publication thereof by Stellenbosch University will not infringe any third party rights and that I have not previously in its entirety or in part submitted it for obtaining any qualification.

Signature: Ousmane Sawadogo

Date : March 2015

Copyright © 2015 Stellenbosch University

All rights reserved

Abstract

The investigation of reservoir sedimentation has become an important and valuable research topic in engineering practice. Sediment deposition in reservoirs can affect flood levels, drainage for agriculture land, pumpstation and hydropower operation and navigation.

An extensive review of the technical literature pertaining to suspended sediment transports as well as deposited sediment flushing from reservoirs has shown that most studies on sediment are still based on empirical formulas and experimental work, despite the availability of sophisticated computers. This is because sediment transport and particularly sediment deposition and erosion are complex processes, that involve the interaction of many physical factors which are not easily modelled numerically. In addition, most of the existing three-dimensional numerical models are not coupled hydrodynamic and sediment transport models. They first simulate the velocity field and water depth and then the concentration and bed change are calculated. Furthermore, they are not fully three-dimensional models for using layer-averaged approaches in conjunction with Saint-Venant equations.

The key objective of the present research was to develop a coupled fully three-dimensional (3D) numerical model based on Navier-Stokes equations which includes both the sediment transport component and hydrodynamic parameters. In this regard, a physical model was set up in a laboratory flume in order to investigate the bottom outlet sediment flushing under pressure in a controlled environment. The proposed coupled fully 3D numerical model was used to simulate the experimental tests. Results from these simulations were in good agreement with the measurements. The geometric features of the scour hole (temporal and spatial hole development) upstream of the bottom outlet were reasonably well predicted compared to the experimental data. Furthermore, the velocity field upstream of the bottom outlet was in good agreement with measurements. The proposed numerical model can be considered reliable provided that the model is correctly set up to reflect the condition of a particular case study. Finally, the coupled fully 3D numerical model for turbulent suspended sediment transport in reservoirs was validated against a range of typical reservoir sediment transport and deposition laboratory flume cases. The proposed suspended sediment transport model successfully predicted both sediment deposition and entrainment processes and therefore, it can be used for turbulent suspended sediment transport assessments in reservoirs.

Opsomming

Die ondersoek van damtoeslikking het 'n belangrike navorsing onderwerp in ingenieurswese praktyk geword. Sedimentdeponering in damme kan vloed vlakke, dreinerings van landbou grond sowel as pompstasie en hidrokrag werking en navigasie beïnvloed.

'n Omvattende ontleding van die tegniese literatuur met betrekking tot gesuspendeerde sedimentvervoer asook die spoel van gedeponeerde sediment uit reservoirs het getoon dat die meeste studies oor sediment steeds op empiriese formules en eksperimentele werk gebaseer is, ten spyte van die beskikbaarheid van gesofistikeerde rekenars. Dit is omdat sedimentvervoer en veral sedimentafsetting en -erosie komplekse prosesse is, wat die interaksie van baie fisiese faktore behels en nie moeiteloos numeries gemodelleer kan word nie. Daarbenewens, in die meeste van die bestaande drie -dimensionele numeriese modelle is die hidrodinamika en sedimentvervoer modelle nie gekoppel nie. Die numeriese modelle simuleer eerstens die snelheid veld en waterdiepte en dan word die sedimentkonsentrasie en bedverandering bereken. Verder is die bestaande modelle nie ten volle driedimensioneel nie, en gebruik laag-gemiddelde benadering in samewerking met Saint-Venant vergelykings.

Die hoofdoelwit van die huidige navorsing was om 'n gekoppelde volle drie -dimensionele (3D) numeriese model gebaseer op Navier-Stokes-vergelykings wat beide die sediment vervoer komponent en hidrodinamiese parameters insluit, te ontwikkel. In hierdie verband is 'n fisiese model opgestel in 'n laboratorium kanaal om die bodem uitlaat spoel van sediment onder druk in 'n beheerde omgewing te ondersoek. Die voorgestelde gekoppelde 3D numeriese model is gebruik om die eksperimentele toets na te boots. Resultate van hierdie simulaties het goed ooreengestem met die metings. Die geometriese eienskappe van die erosie gat (tyd en ruimtelike gatontwikkeling) stroomop van die bodemuitlaat was redelik goed voorspel vergeleke met die eksperimentele data. Verder is die snelheid veld stroomop van die bodem uitlaat ook goed voorspel. Die voorgestelde numeriese model kan beskou word as betroubaar met die wete dat die model korrek opgestel is om die toestand van 'n bepaalde gevallestudie te weerspieël. Ten slotte, is 'n gekoppelde 3D numeriese model vir turbulente gesuspendeerde sediment vervoer in reservoirs ontwikkel en getoets teen 'n reeks laboratorium kanaal eksperimente. Die voorgestelde gesuspendeerde sediment vervoer model voorspel suksesvol beide die sediment afsetting- en erosieprosesse en daarom kan dit gebruik word vir die simulasie van turbulente gesuspendeerde sediment vervoer in damme .

Acknowledgements

First and foremost I would like to acknowledge my supervisor, Professor Gerrit R. Basson, for his endless support and invaluable guidance throughout the execution of this dissertation.

I am grateful to the African Institute for Mathematical Sciences (AIMS) for giving me the opportunity to pursue my studies here in South Africa.

I am also grateful to the University of Stellenbosch for the financial support. Appreciation is also expressed to QFINSOFT Co. for providing the ANSYS FLUENT software package as well as software training.

I equally acknowledge the profound assistance offered by Dr. S. Schneiderbauer of Johannes Kepler University, Austria, regarding ANSYS FLUENT software setup.

Similarly, I extend my appreciation to my colleagues and friends in the postgraduate student office (S417), especially Vincent Msadala and staff of the Institute for Water and Environmental Engineering (IWEEUSU), particularly Mr. Christiaan Visser and Mr. Wageed Kamish for their assistance and encouragement.

I would also like to thank my fellow Burkinabe Nationals in Cape Town for their precious advice and support, especially my close friend, Dr. S. Lougue and his wife. My special gratitude goes to my friends Issahaka and Kassim for proof reading my work.

Last but not least, I express my deep gratitude to my family for the incredible support thus far in my life. Special mention to my parents and my old sister, Salimata for instilling in me values of confidence, dedication and perseverance without which this work could not be executed successfully. Uncle Zackaria equally rendered me immense support but passed away when I was finalising this dissertation. May the souls of my late dad and uncle rest in peace. To all my siblings, with whom I shared a good childhood, I appreciate your love and encouragement.

To my wife Haoua, my daughter Zeynab and my son Tariq Yamba, I say thank you for their unconditional encouragement, love and patience.

Most importantly, praise be to Almighty Allah for giving me the strength and good health to complete this study.

Contents

Declaration	i
Abstract	ii
Opsomming	iii
Acknowledgements	iv
List of Figures	x
List of Tables	xv
List of Symbols	xvii
List of Abbreviations	xxiv
1 Introduction	1
1.1 Background and Motivation	1
1.2 Objectives	2
1.3 Methodology	3
2 Literature Review	4
2.1 Sediment Characteristics	4
2.1.1 Introduction	4
2.1.2 Individual Properties of Sediment	4
2.1.3 Bulk Properties of Sediment	9
2.1.4 Summary	12

2.2	Sediment Transport in Rivers	12
2.2.1	Introduction	12
2.2.2	Bed-Load Transport	13
2.2.3	Suspended Load Transport	13
2.2.4	Wash Load Transport	13
2.2.5	Total Load Transport	13
2.2.6	Summary	14
2.3	Reservoir Sedimentation Processes	14
2.3.1	Introduction	14
2.3.2	Sediment Transport in Reservoirs	15
2.3.3	Sediment Deposition in Reservoirs	15
2.3.4	Sedimentation Control in Reservoirs	16
2.3.5	Summary	21
2.4	Overview on Bottom Outlet Sediment Flushing under Pressure	21
2.4.1	Introduction	21
2.4.2	Previous Studies done on Bottom Outlet Flushing	23
2.5	Theoretical Considerations of Suspended Load Transport	31
2.5.1	Introduction	31
2.5.2	Diffusion Models of Suspension	32
2.5.3	The Energy Approach of Suspension	34
2.5.4	Statistical Models of Suspension	35
2.5.5	Numerical Models of Suspension	35
2.5.6	Summary	36
2.6	Overview on Mathematical Modelling of Turbulent Suspended Sediment Transport	36

2.6.1	Introduction	36
2.6.2	One-Dimensional Models	36
2.6.3	Two-Dimensional Models	38
2.6.4	Three-Dimensional Models	39
2.6.5	Summary	41
3	Experimental Investigations of Bottom Outlet Flushing under Pressure	42
3.1	Introduction	42
3.2	Physical Model Setup	42
3.3	Laboratory Test Procedure	49
3.4	Physical Model Test Results	50
3.4.1	Visual Observations of the Scour Process	50
3.4.2	Test Results of Scour Depth and Extent	52
3.4.3	Test Results of Scour Bed Profiles	54
3.4.4	Experimental Test Limitations	58
3.5	Summary	58
4	Three-Dimensional Numerical Bottom Outlet Flushing Model Development	59
4.1	Introduction	59
4.2	Computational Fluid Dynamics Modelling	59
4.2.1	Governing Equations	59
4.2.2	Turbulence Model	60
4.3	Sediment Transport Modelling	62
4.3.1	Sediment Erosion and Deposition Model	64
4.3.2	Modelling of the Packed Bed Surface Deformation	71

4.3.3	Estimation of Water Induced Shear Stress for Hydrodynamic Entrainment	75
4.4	Summary	77
5	Three-Dimensional Numerical Simulation of the Bottom Outlet Flushing	78
5.1	Introduction	78
5.2	Numerical Model Setup	78
5.2.1	Computational Fluid Dynamics Software	79
5.2.2	Model Geometry and Grid Cells	80
5.2.3	Model Boundary Conditions	82
5.2.4	Numerical Solution Technique and Procedure	83
5.3	Simulation Results	86
5.3.1	Model Calibration	86
5.3.2	Bed Deformation Results	86
5.3.3	Hydrodynamic Results	88
5.4	Validation of the Simulation Results against Experimental Data	92
5.4.1	Comparison of Bed Deformation	92
5.4.2	Comparison of Scour Hole Profiles	94
5.4.3	Comparison of Flow Velocity	99
5.5	Sensitivity Analysis of the Proposed Numerical Model	100
5.5.1	Creeping Parameter	100
5.5.2	Diffusion Coefficient	101
5.5.3	Packing Ratio	102
5.5.4	Sediment Size	102
5.5.5	Sediment Roughness	103
5.5.6	Sediment Density	103

5.5.7	Mesh Size	104
5.6	Summary	105
6	Three-Dimensional Suspended Sediment Transport Model Development	106
6.1	Introduction	106
6.2	Hydrodynamic Modelling	106
6.2.1	Continuity and Momentum Equations	106
6.2.2	Turbulence Model	107
6.2.3	Boundary Conditions	107
6.3	Transport Model	108
6.3.1	Convection-Diffusion Equation	108
6.3.2	Boundary Conditions for Sediment Transport	108
6.4	Model Solver: ANSYS FLUENT	109
6.5	Summary	109
7	Three-Dimensional Suspended Sediment Transport Model Testing	110
7.1	Overview on Experimental Cases Simulated by the Model	110
7.2	Numerical Solution Procedure	111
7.3	Dye-Mixing Simulation	112
7.4	Sediment Transport Simulation with Known Net Flux at the Bed	113
7.4.1	Zero Net Flux at the Bed	113
7.4.2	Net Deposition to a Fixed Bed	114
7.5	Sediment Transport Simulation with Net Entrainment and Net Deposition Model	116
7.5.1	Net Entrainment from a Loose Bed	116
7.5.2	Net Entrainment on a Fixed Bed	116

7.5.3	Net Deposition on a Fixed Bed	117
7.6	Summary	118
8	Conclusions and Recommendations	119
8.1	Physical Modelling of the Bottom Outlet Flushing under Pressure	120
8.2	Coupled and Fully 3D Numerical Modelling of the Bottom Outlet Flushing under Pressure	120
8.3	Coupled and Fully 3D Numerical Modelling of Suspended Sediment Transport	121
8.4	Recommendations for Further Research	121
	References	123
	Appendices	131
A	Experimental Test Results	131
A.1	Experimental Results for Test 2	132
A.2	Experimental Results for Test 3	134
B	Simulation Test Results	136
B.1	Simulation Results for Test 2	137
B.2	Simulation Results for Test 3	140
B.3	Simulation Results for Test 4	143

List of Figures

2.1	Relation between C_d and R_e for sphere (Wu, 2008)	8
2.2	Normal and cumulative frequency curve (Yang, 2003)	10
2.3	Composition of sediment transport	14
2.4	Longitudinal sediment deposition patterns in reservoirs (Shen, 1999)	19
2.5	Sediment erosion during flushing operation in reservoirs (Shen, 1999)	20
2.6	Isovelocity contours upstream of orifices of different shapes (Shammaa et al., 2005)	23
2.7	Velocity profile comparison with measurement (Bryant et al., 2008)	24
2.8	Flow through a sluice gate - definition sketch (Rajaratnam and Humphries, 1982)	25
2.9	Pressure head dropped on the bed (Rajaratnam and Humphries, 1982)	26
2.10	Typical velocity upstream of the gate (Rajaratnam and Humphries, 1982)	26
2.11	Simplified flow pattern at bottom outlet (Scheuerlein, 2004)	30
2.12	Distribution of suspended load in a flow (Raudkivi, 1998)	34
3.1	Experimental flume layout	44
3.2	Laboratory flume view from upstream	45
3.3	Packed bed levelled with the outlet invert	46
3.4	Measurement instruments	47
3.5	Sediment size distribution curve (Stephan, 2013)	48
3.6	Scour hole extent and scouring process based on visual observations	51
3.7	Scour hole for Test 1	53
3.8	3D bed surface mapping for Test 1	53
3.9	Cartesian coordinate system	54
3.10	Observed lateral cross sections of the scour hole for Test 1	55

3.11	Observed longitudinal cross sections of the scour hole for Test 1	56
3.12	Lateral cross section variation with flow rate	57
3.13	Longitudinal cross section variation with flow rate	57
4.1	Sketch of particle impact at the surface of the packed bed	68
4.2	Sketch of Immersed Boundary Method	73
5.1	Computational model geometry	80
5.2	Computational grid cell	81
5.3	The proposed numerical model flowchart	85
5.4	Simulated longitudinal variation of the scour hole with time for Test 1	87
5.5	Simulated scour hole for Test 1 (after 1800 s)	88
5.6	Simulated static pressure distribution at the bed	89
5.7	Contours of simulated flow velocity for Test 1 (after 1800 s)	90
5.8	Simulated flow streamline for Test 1 (after 1800 s)	90
5.9	Contours of the simulated eddy viscosity for Test 1 (after 1800 s)	91
5.10	Contours of the simulated bed shear stress for Test 1 (after 1800 s)	91
5.11	Plan view of final bed level for Test 1	92
5.12	Plan view of final bed level for Test 2	93
5.13	Plan view of final bed level for Test 3	93
5.14	Lateral bed profile results comparison for Test1	95
5.15	Longitudinal bed profile results comparison for Test 1	96
5.16	Lateral bed profile results comparison for Test2	96
5.17	Longitudinal bed profile results comparison for Test 2	97
5.18	Lateral bed profile results comparison for Test3	97

5.19	Longitudinal bed profile results comparison for Test 3	98
5.20	Lateral bed profile results comparison for Test 4	98
5.21	Results comparison of velocity variation on the vertical plane	99
5.22	Results comparison of velocity variation on the horizontal plane	99
5.23	Results comparison of velocity variation on the centreline	100
5.24	Results of sensitivity analysis for creeping parameter	101
5.25	Results of sensitivity analysis for diffusion coefficient	101
5.26	Results of sensitivity analysis for packing ratio parameter	102
5.27	Results of sensitivity analysis for sediment size	103
5.28	Results of sensitivity analysis for sediment roughness	103
5.29	Results of sensitivity analysis for sediment density	104
5.30	Results of sensitivity analysis for mesh sensitivity	104
7.1	Zoomed view of simulated geometry and grid cells	111
7.2	Comparison of simulated dye-concentration profiles with experimental data	113
7.3	Comparison of simulated concentration profiles with experimental data for zero net flux at the bed	114
7.4	Comparison of simulated concentration profiles with experimental data for net deposition to a fixed bed	115
7.5	Downstream development of suspended load in net deposition case	115
7.6	Downstream development of near-bed concentration in net deposition case	115
7.7	Comparison of simulated sediment concentration profiles with experiment data in case of net entrainment from a loose sand bed	116
7.8	Comparison of simulated sediment concentration profiles with experiment data in case of net entrainment on a fixed bed	117

7.9 Comparison of simulated sediment concentration profiles with experiment data in case of net deposition on a fixed bed	118
A.1 Scour hole for Test 2	132
A.2 3D bed surface mapping for Test 2	132
A.3 Observed lateral cross sections of the scour hole for Test 2	133
A.4 Observed longitudinal cross sections of the scour hole for Test 2	133
A.5 Scour hole for Test 3	134
A.6 3D bed surface mapping for Test 3	134
A.7 Observed lateral cross sections of the scour hole for Test 3	135
A.8 Observed longitudinal cross sections of the scour hole for Test 3	135
B.1 Simulated scour hole for Test 2	137
B.2 Contours of simulated flow velocity for Test 2	137
B.3 Simulated flow streamline for Test 2	138
B.4 Contours of the simulated eddy viscosity for Test 2	138
B.5 Contours of the simulated bed shear stress for Test 2	139
B.6 Simulated scour hole for Test 3	140
B.7 Contours of simulated flow velocity for Test 3	140
B.8 Simulated flow streamline for Test 3	141
B.9 Contours of the simulated eddy viscosity for Test 3	141
B.10 Contours of the simulated bed shear stress for Test 3	142
B.11 Simulated scour hole for Test 4	143
B.12 Contours of simulated flow velocity for Test 4	143
B.13 Simulated flow streamline for Test 4	144
B.14 Contours of the simulated eddy viscosity for Test 4	144

B.15 Contours of the simulated bed shear stress for Test 4 145

List of Tables

3.1	Experimental results	52
5.1	Details of generated mesh	82
5.2	Summary of result comparisons	95
7.1	Experimental measurements	111

List of Symbols

A	Orifice area
	Cross section area
a	Settling probability for particle to deposit at the bed
a, b, c	Three orthogonal particle axes
a_x	Entrainment particle constant
$C_{1\varepsilon}, C_{2\varepsilon}, C_\mu$	Turbulence model coefficients
C_b	Reference concentration
	Near-bed concentration
C_{bmax}	Reference concentration value at equilibrium
C_c	Contraction coefficient of discharge
C_D	Drag coefficient
C_{ref}	Initial discharge concentration
C_j	Sum of cells for which cell j is the nearest neighbour cell located along the steepest descent
C_v	Dimensionless coefficient for particle entrainment
C_η	Empirical coefficient for particle entrainment
C'_η	Dimensionless coefficient for particle entrainment
c	Concentration
c_a	Concentration at reference level a
c_a, c_h	Impacting empirical coefficients
c_i	Velocity scale
c_s	Fraction of energy not converted to heat after impact
D	Orifice diameter
	Coefficient of diffusion
D_G	Diameter of the bottom outlet
D_h	Hydraulic diameter
D_{ij}	Turbulent eddy diffusivity tensor
D_M	Molecular diffusion
D_{scour}	Scour depth
d	Particle diameter

	Rate of deposition
d_p	Diameter of particulate phase
d_{50}	Size of sediment for which 50% of the sample is finer
d_m	Mean sediment diameter
d_g	Geometric mean size
e	Rate of entrainment
F_C	Critical drag force per unit cross-sectional horizontal area
F'_C	Critical drag force
F_D	Drag force
F_L	Lift force acting on a particle
\mathbf{F}_q	Additional volumetric forces of phase q
f_r	Roughness function
G	Gradation coefficient
G_k	Production of turbulence kinetic
G_r	Gradation coefficient
G_s	Relative density
g	Gravitational acceleration
H	Total available head
H_0	Pressure head above the outlet
H_s	Deposited sediment height
H_v	Velocity head
$\bar{\mathbf{I}}$	Unity tensor
h	Water depth
K_1, K_2	Head coefficients
K_s	Average roughness size
k	Kinetic energy of turbulence
k_p	Kinetic energy of turbulence at first fluid cells
L_{scour}	Scour length
m	Mass of particle
m_{im}	Impacting particle mass
m_{pq}	Mass transfer from phase p to phase q
m_{qp}	Mass transfer from phase q to phase p

m_{sp}	Splashed particle mass
N_A, N'_A	Number of sand grains entrained per unit time and per unit area
N_{EpI}	Number of ejected particles per impact
N_{im}	Number of impact per unit time
n	Number of time step
P	Porosity
	Quantity rate across unit area normal to y-axis
	Cross section perimeter
	Dynamic pressure
p	Pressure for all phases
p_r	Probability of particle entrainment into surface rolling transport mode
p_{re}	Probability of particle rebound
p_{re}^{max}	Probability of impacting particle with high velocity
p_{tr}	Probability of trapped particle
Q	Outlet discharge
Q_s	Suspended load
q	Phase
Re	Particle Reynolds number
Re_p	Relative Reynolds number
R_{pq}	Interface momentum exchange term
r	Radial distance of a sphere-shaped isotach from the bottom outlet
	Sediment particle radius
	Physical roughness height
S	Surface of the packed bed
SD_{C-M}	Maximum scour depth
S_{de}^{sl}	Amount of deposition due to shearing slide
S_{er}^{sl}	Amount of erosion due to shearing slide
S_L	Scour length
S_k	Source term for turbulent kinematic energy k
S_p	Shape factor
S_q	Mass source term of phase q
S_{rol}	Contributing mass source for rolling particles

S_{rol}^e	Total mass per unit volume and unit time for particles entrained into surface rolling
S_{rol}^{ej}	Total mass per unit volume and unit time for splashed particles due to particle impact at the packed bed surface
S_{rol}^{de}	Total mass per unit volume and unit time of deposition of rolling particles
S_{sal}	Contributing mass source for saltating particles
S_{sal}^e	Total mass per unit volume and unit time for particles entrained into saltation
S_{sal}^{ej}	Total mass per unit volume and unit time for ejected particles due to impacting saltating particles
S_{sal}^{de}	Total mass per unit volume and unit time of deposition of saltating particles
S_{sd}	Source term accounting for erosion and deposition at the packed bed
S_t	Time scaling factor
S_W	Scour width
S_ε	Turbulent dissipation rate ε
$\overline{\mathbf{T}}_q$	Stress-strain tensor of phase q
$\overline{\mathbf{T}}_2$	Second invariant of the rate-of-strain tensor of the mixture
t	Time
t_{end}	Time end
t_f	Fluid time scale
t_h	Packed bed surface deformation time scale
t'_s	Mean travel time for saltating particles
U_*	Shear velocity
U_0	Average orifice velocity
U_E	Ejecting particle velocity
U_I, U_{Im}	Impacting particle velocity
U_j	Component of local time-averaged flow velocities
U_m	Mean velocity
U_R	Rebounding particle velocity
$U_{t,sp}^*$	Threshold of the shear velocity

U^*	Dimensionless velocity
$u_{i,o}$	Initial ejection velocity of the particle
$\overline{u'_i u'_j}$	Reynolds stresses
u_j	Component of local time-averaged flow velocities
u_p	Mean velocity at first fluid cells
u_s^*	Shear velocity at the surface of the packed bed
u_{x0}	Mean lift-off particle velocity in x direction
u^*	Wall shear velocity
V	Velocity
	Volume of a grid cell adjacent to the packed bed
\mathbf{V}	Velocity of the mixture
\mathbf{V}_p	Volume of particle
\mathbf{V}_q	Velocity of phase q
V_s	Total volume of sediment excluding voids
	Volume of the flushing cone
V_t	Total volume of sediment including voids
V_v	Volume of voids
W_s	Width of the flushing cone
W_{scour}	Scour width
v_r	Flow velocity at distance r
Y^*, Y^+	Dimensionless distance from the wall
y	Elevation
y_b	Cell-wall distance
Z	Flow depth
α_b	Volume fraction of the packed bed
α_E	Ejecting angle
α_I	Impacting angle
α_{pr}	Packing ratio
α_q	Volume fraction
α_R	Angle of rebound
α_r	Volume fraction of rolling particle phase
α_s	Volume fraction of saltating particle phase

α_w	Volume fraction of water phase
β	Differences between diffusion of solids and fluid Mean drag level
γ	Ratio of maximum to mean drag and lift on the particle
γ_s	Sediment specific weight
δ	Size of a discrete shearing slide
δ_{ij}	Kronecker delta
ε	Momentum diffusion in fluid Rate of dissipation of turbulence energy
ε_p	Turbulent dissipation rate at first fluid cells
ε_s	Diffusion coefficient for sediment
ζ_r	Restitution parameter of particle-bed collision
η	Ratio of mean drag and lift per unit area on the whole bed to mean drag and lift on the top grain entrained by the fluid
θ	Slope angle with respect to the flow direction
κ	Karman constant
μ	Dynamic viscosity
μ_G	Loss coefficient at the outlet
μ_q	Shear viscosity of phase q
μ_t	Turbulent viscosity
μ_w	Shear viscosity of water
ν	Kinematic viscosity
ν_T	Eddy viscosity
ρ	Fluid density Mixture phase density
ρ_b	Bulk density of the packed bed
ρ_p	Particle density
ρ_q	Density of phase q
ρ_s	Density of sediment
ρ_w	Density of water
σ_c	Turbulent Schmidt number
σ_g	Geometric standard deviation

$\sigma_k, \sigma_\varepsilon$	Turbulence model coefficients
ζ_s	Splash coefficient
τ_t	Fluid shear stress threshold for particle entrainment
τ_s	Shear stress at the surface
τ_w	Wall shear stress exerted by the mixture phase onto the surface of the packed bed
ϕ	Angle of slope
φ	Angle of repose
ω, ω_s	Settling velocity
Γ_b, λ_b	Packed bed diffusion coefficient
Δt	Size of time step

List of Abbreviations

<i>1D</i>	One-Dimensional
<i>2D</i>	Two-Dimensional
<i>3D</i>	Three-Dimensional
<i>ADV</i>	Acoustic Doppler Velocimeter
<i>CFD</i>	Computational Fluid Dynamics
<i>DES</i>	Detached Eddy Simulation
<i>DHI</i>	Danish Hydraulic Institute
<i>FSL</i>	Full Supply Level
<i>GSTARS</i>	Generalized Sediment Transport model for Alluvial River Simulation
<i>GUI</i>	Graphical User Interface
<i>NCCHE</i>	National Centre of Computational Hydroscience and Engineering
<i>MOBED</i>	Mobile Bed
<i>RESSASS</i>	Reservoir Survey Analysis and Sedimentation Simulation
<i>SANRAL</i>	South Africa National Road Agency
<i>SSIIM</i>	Sediment Simulation in Intakes with Multiblock Option
<i>SUTRENCH</i>	Suspended sediment Transport in Trenches
<i>UDF</i>	User-Defined Function
<i>UDS</i>	User-Defined Scalar
<i>USACE</i>	United States Army Corps of Engineering
<i>USBR</i>	United States Bureau of Reclamation

1. Introduction

1.1 Background and Motivation

With a worldwide average annual sedimentation rate of about 0.8% of the original storage capacities, reservoir sedimentation is expected to become a serious problem in many reservoirs during the next 50 years (Basson and Rooseboom, 2008). According to the same authors, reservoir sedimentation has proven to be a serious problem in South Africa and therefore, extensive research has been undertaken in this field over the past 30 years. This led to guidelines on the management of the reservoir sedimentation problems published by Basson and Rooseboom (1997).

Sediment deposition in reservoirs can consequently affect flood levels, drainage from agriculture land, pumpstation and hydropower operation and navigation. However, the loss in storage capacity for domestic or industrial supply and irrigation is the major effect of reservoir sedimentation in semi-arid climates, particularly in South Africa (Basson and Rooseboom, 1997). This loss in storage capacity has a serious impact on irrigation systems and consequently, can undermine food security in semi-arid areas due to water scarcity.

The flow of water over a mobile bed has the ability to entrain solid particles. Consequently, mixture from the interaction between water and sediment will displace itself in the watercourse. The movement of the sediment will modify the flow but also the bed in terms of its elevation, its slope and its roughness. Therefore, the interaction between the water and the sediment is described as a coupled problem. When a river enters a reservoir, sediment deposition occurs with coarser sediment which is generally deposited in the upstream part of a storage reservoir while fine sediments (clay and silt fractions) are transported much deeper into the reservoir towards the dam.

Turbulent suspended sediment transport is the dominant mechanism of sediment transport through most reservoirs. According to Graf (1998) suspended sediment consists of particles that stay occasionally in contact with the bed and they displace themselves by making more or less large jumps and remain often surrounded by water. This type of transport concerns relatively smaller sediment particles.

During the past century, a large number of sediment transport equations have been derived and calibrated in most cases by means of coefficients from laboratory and field data. Methods for the prediction of reservoir sedimentation have been the subject of several empirical studies for many years. A number

of studies conducted by White et al. (1975), Yang and Molinas (1982) and Van Rijn (1984b) have compared the accuracy of these empirical methods in the prediction of sediment transport. These studies found out that there was a wide range of results which are obtained with these equations, even under controlled laboratory conditions. The reason for this is the complicated hydraulic processes which involve simultaneously sediment transport, deposition and erosion. Therefore, the understanding of sediment transport processes has not been developed well enough, even after many years of research in this field. Sediment transport equations can basically be divided into two groups: those that predict bed load and suspended load transport separately, and those that predict a total sediment load without the distinction between bed load and suspended load. The interrelationship between bedforms, associated roughness, hydraulic and sediment transport capacities and also the change in velocity profile when sediment is being transported have not been adequately modelled (Basson and Rooseboom, 2008).

For reservoir conditions, the forecast of the transport of fine sediments (silt and clay) is also important since in many impoundments they form the main sediment body. The prediction of the transport of fine sediments within reservoirs has been based on the following approaches: use of the diffusion equation; use of sediment transport equations which were calibrated originally for sand fractions adopted to include fine sediments by recalibration with fine sediment transport data; and combinations of sediment transport equations for sand fraction and diffusion equations for fine sediments.

A better understanding of reservoir sedimentation has a potential to limit sedimentation processes and therefore, increase water storage capacity in reservoirs. At the end, adequate storage in reservoirs can provide the much needed water for irrigation purposes. In the long run, it can help stabilise food production, increase crop intensity, diversify agriculture and subsequently contribute to a significant improvement in food security.

1.2 Objectives

Most of existing three-dimensional (3D) numerical models are not coupled flow and sediment transport models. They simulate first the velocity field and water depth and then the concentration and bed change are calculated using the velocity field and water depth. Furthermore, they are not fully three-dimensional models for using layer-averaged approaches in conjunction with Saint-Venant equations.

The present research developed a fully coupled 3D numerical model based on Navier-Stokes equations which include both sediment transport component and hydrodynamic parameters. The research

contributes to the knowledge and understanding reservoir sedimentation particularly the mathematical modelling of turbulent suspended sediment transport dynamics and the bottom outlet sediment flushing process. An improved coupled fully 3D model will help in the determination of the detailed spatial and temporal pattern of the sediment concentration and also the extent of erosion during the pressurised bottom outlet flushing in reservoirs. The outcome from this proposed research contributes to the management of the reservoir sedimentation problems, such as:

- Minimising deposition in reservoirs through sluicing.
- Removing accumulated sediment from the reservoir through bottom outlet flushing.
- Diverting flow with high sediment concentration to bypass the reservoir.
- Controlling the deposition of sediment at the bottom of an intake of hydropower scheme.

1.3 Methodology

To achieve the above mentioned aims, the following methodology was followed:

1. Review of literature on reservoir sedimentation processes including the bottom outlet flushing, suspended-load sediment transport dynamics and turbulence modelling in the two-phase approach.
2. Carry out bottom outlet flushing laboratory tests in order to collect measurement data for the validation of the coupled and fully 3D mathematical model of bottom outlet sediment flushing.
3. Develop a coupled and fully 3D numerical model which is able to accurately predict the experimental test results of the bottom outlet sediment flushing.
4. Conduct sensitivity and uncertainty analysis of the proposed 3D numerical model.
5. Validate the proposed numerical model against data from literature in terms of suspended sediment transport which includes sediment deposition and entrainment processes.

2. Literature Review

2.1 Sediment Characteristics

2.1.1 Introduction

The study of sediment transport deals with the interrelationship between flowing water and sediment particles. As individual particles, the sediments have their own characteristics. Therefore, an understanding of the physical properties of sediment particles is essential to model the sediment transport. The properties of the sediments can be divided basically into two types: individual and bulk properties. Although the list of parameters describing these properties may be very extensive, only those that are relevant to the model presently developed are described in the following sections.

2.1.2 Individual Properties of Sediment

Sediment properties of a single particle that are important in the study of sediment transport are particle size, shape, density and settling velocity.

2.1.2.1 Size

Size is the basic and most readily measurable property of sediment and it has also been found to efficiently describe the physical property of the sediment particle in many practical purposes. The size of sediment particle can be determined by sieve or visual-accumulation tube analyses. There are five different definitions related to the concept of particle diameter. They are generally defined for spheres and applied to sediments.

- **Nominal Diameter** is the diameter of a sphere having the same volume as the sediment particle.
- **Sieve Diameter** is the diameter of a sphere equal to the length of the side of the square sieve opening through which the particle can just pass. The sieve diameter, as an approximation is equal to the nominal diameter.
- **Fall Diameter** is the diameter of the sphere that has a specific gravity of 2.65 and has the same average terminal fall velocity as the particle when each is allowed to settle alone in quiescent,

distilled water. Average terminal particle fall velocity is defined as being the maximum velocity reached by a particle falling in pure water at 24°C in a vessel of infinite dimensions (Simons and Sentürk, 1992).

- **Sedimentation Diameter** has the same definition as fall diameter, but the sphere specific gravity is replaced by that of the particle. This diameter, therefore, provides more realistic values for sediment particle diameter compared with nominal diameter.
- **Triaxial Diameter** is the arithmetic averaged value of the three orthogonal particle axes commonly named, a , b and c .

2.1.2.2 Shape

Shape refers to the form or configuration of a particle regardless of its size or composition. The shape of a particle affects the average velocity of the water flow, the fall velocity and the bed load transport (Campos, 2001). Although many parameters describing the particle shape are found in the literature, only three are presented in the present section due to their importance.

- **Shape Factor** is the most significant expression of particle shape from the viewpoint of simplicity and effective correlation and it is defined by the following expression (Yang, 2003):

$$S_p = \frac{c}{\sqrt{ab}} \quad (2.1)$$

In Equation 2.1, a , b and c are the lengths of the longest, the intermediate and the shortest mutually perpendicular axes through the particle respectively and S_p is the shape factor. It has a value of 1.0 for a sphere and naturally worn quartz particles have an average shape factor of 0.7 (Yang, 2003).

- **Sphericity** is the ratio between the surface area of a sphere with the same volume as the particle and the actual particle's area. Its value is 1.0 for a sphere and less than 1.0 for the other shapes. The value of the sphericity for a single particle is difficult to determine due to the multiplicity of a very small surface area on a particle, which is not easy to measure.
- **Boundness** is the ratio of the average radius of curvature of the several corners and edges to the radius of curvature of the maximum inscribed sphere or the nominal radius of the particle (Pettijohn, 1975).

2.1.2.3 Density

The density of a sediment particle refers to its mineral composition and is defined as the ratio of the weight of a single particle to its volume. Usually, specific gravity, which is defined as the ratio of specific weight or density of sediment to the specific weight or density of water, is used as an indicator of density. Commonly a specific gravity value of 2.65 is used for most non-cohesive quartz sediment particles found in natural rivers.

2.1.2.4 Settling Velocity

Settling or fall velocity is the average terminal velocity that a sediment particle attains in the settling process in quiescent, distilled water of infinite extent. It is directly related to relative flow conditions between the sediment particle and water during conditions of sediment entrainment, transportation and deposition. Settling velocity is generally considered as the most important individual property of sediment particle and can be calculated from the balance between the particle submerged weight and the resisting force resulting from fluid drag. The general drag force equation is expressed as (Yang, 2003)

$$F_D = C_D \rho A \frac{\omega^2}{2} \quad (2.2)$$

where F_D is the drag force, C_D is the drag coefficient, ρ is the density of water, A is the projected area of particle in the direction of settling and has a value of πr^2 for a sphere, and ω is the settling velocity.

The submerged weight of a spherical sediment particle is

$$W_S = \frac{4}{3} r^3 \pi (\rho_s - \rho) g \quad (2.3)$$

where r is the sediment particle radius, and ρ_s and ρ are densities of sediment and water, respectively. In the terminal stage of settling, the drag force (Equation 2.2) should be equal to the submerged weight (Equation 2.3), yielding

$$\omega = \left(\frac{8}{3} \frac{1}{C_D} \frac{\rho_s - \rho}{\rho} r g \right)^{1/2} \quad (2.4)$$

According to Equation 2.4, settling velocity can therefore, be calculated once the only remaining unknown which is the drag coefficient has been determined. The drag coefficient is a function of Reynolds number and shape factor. To determine the settling velocity, the analytical C_D expressions were first developed assuming that the sediment particle is spherical. For non-spherical particles, the first approach

was modified by introducing an additional correction factor which takes into consideration the particle shape.

- **Settling velocity of spherical particles:** In the laminar settling region, where the particle Reynolds number R_e is less than 1.0, the drag force on a spherical particle was derived by solving the Navier-Stokes equations without inertia terms. The drag coefficient thus obtain is (Graf, 1971)

$$C_D = \frac{24}{R_e} \quad (2.5)$$

where $R_e = \omega d/\nu$ and ν is the kinematic viscosity. Inserting Equation 2.5 into Equation 2.4 leads to the Stokes law for settling velocity of spherical particles:

$$\omega = \frac{1}{18} \frac{\rho_s - \rho}{\rho} g \frac{d^2}{\nu} \quad (2.6)$$

where ω is the settling velocity and d is the particle diameter.

Oseen formula was obtained by solving the Navier-Stokes equations, including some inertia terms (Wu, 2008):

$$C_D = \frac{24}{R_e} \left(1 + \frac{3}{16} R_e \right) \quad (2.7)$$

The following drag coefficient, which is a relatively complete solution of Oseen's approximation was proposed (Wu, 2008):

$$C_D = \frac{24}{R_e} \left(1 + \frac{3}{16} R_e - \frac{19}{1280} R_e^2 + \frac{71}{20480} R_e^3 + \dots \right) \quad (2.8)$$

Equation 2.8 is only valid for R_e up to 2.0 and for R_e more than 2.0, the drag coefficient usually has to be determine by experiments rather than theoretical solutions. By compiling the available experimental data, Rouse (1936) obtained the relation between C_D and R_e (see Figure 2.12), which can be used to find C_D and then the settling velocity of the spherical particles.

It can be seen from the Figure 2.12 that when R_e is beyond 1000, which corresponds to the turbulent settling region, the drag coefficient has a constant value of about 0.45, thus yielding

$$\omega = 1.72 \left(\frac{\rho_s - \rho}{\rho} g d \right)^{1/2} \quad (2.9)$$

- **Settling velocity of sediment particles:** In natural rivers, sediment particles usually have non-spherical shapes and rough surfaces and therefore yield different settling velocity in comparison

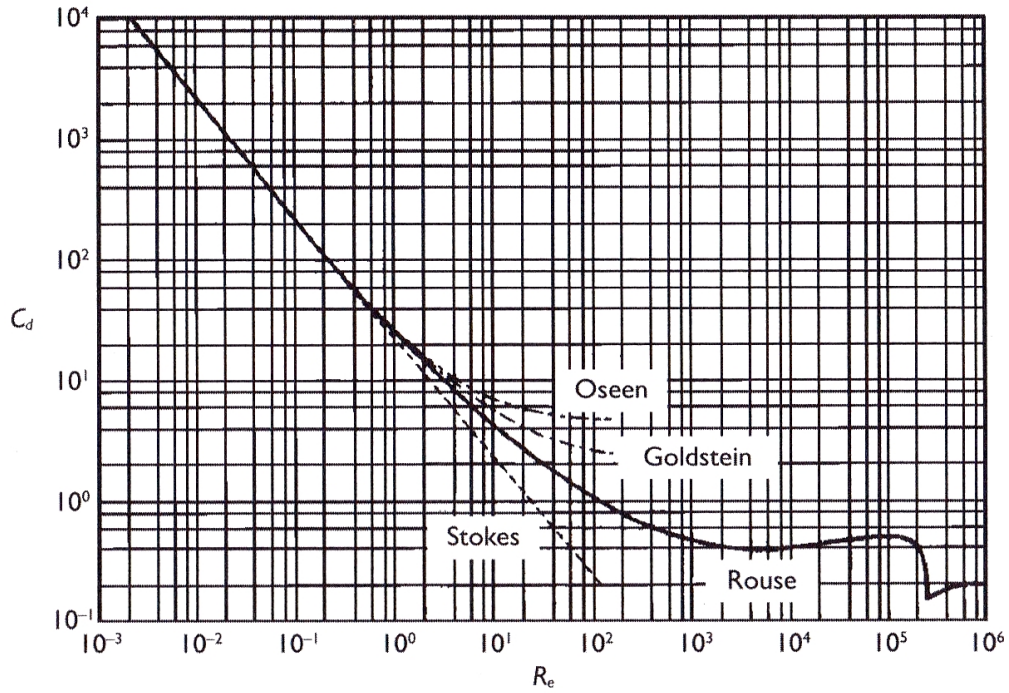


Figure 2.1: Relation between C_d and R_e for sphere (Wu, 2008)

with spherical particles. Rubey (1933) derived the following formula for settling velocity of natural sediment particles:

$$\omega = F \sqrt{\left(\frac{\rho_s}{\rho} - 1\right) gd} \quad (2.10)$$

where $F = 0.79$ for particles larger than 1 mm settling in water with temperatures between 10 and 25°C . For smaller grain sizes, F is determined by

$$F = \left[\frac{2}{3} + \frac{36\nu^2}{gd^3(\rho_s/\rho - 1)} \right]^{1/2} - \left[\frac{36\nu^2}{gd^3(\rho_s/\rho - 1)} \right]^{1/2} \quad (2.11)$$

Based on many laboratory data, Zhang (see Wu (2008)) produced the following formula for settling velocity of naturally worn sediment particle:

$$\omega = \sqrt{\left(13.95 \frac{\nu}{d}\right)^2 + 1.09 \left(\frac{\rho_s}{\rho} - 1\right) gd} - 13.95 \frac{\nu}{d} \quad (2.12)$$

Equation 2.12 can be used in a wide range of sediment sizes from laminar to turbulent settling regions. Van Rijn (1984a) recommended the use of the Stokes law (Equation 2.6) to calculate settling velocity for sediment particles smaller than 0.1 mm , the Zanke (see Wu (2008)) formula for particle sizes ranging from 0.1 to 1.0 mm :

$$\omega = 10 \frac{\nu}{d} \left\{ \left[1 + 0.01 \left(\frac{\rho_s}{\rho} - 1\right) \frac{gd^3}{\nu^2} \right]^{1/2} - 1 \right\} \quad (2.13)$$

and for particles larger than 1.0 mm the following formula is suggested by the same author:

$$\omega = 1.1 \left[\left(\frac{\rho_s}{\rho} - 1 \right) g d \right]^{1/2} \quad (2.14)$$

Cheng (1997) derived the following formula for the settling velocity that is valid for naturally worn sediment particles with shape factors ranging from 0.5 to 0.7:

$$\omega = \frac{\nu}{d} \left(\sqrt{25 + 1.2 D_*^2} - 5 \right)^{1.5} \quad (2.15)$$

where $D_* = d [(\rho_s/\rho - 1)g/\nu^2]^{1/3}$.

2.1.3 Bulk Properties of Sediment

The most important bulk properties in the study of sediment transport are size distribution, specific weight and porosity of the bed material.

2.1.3.1 Particle Size Distribution

Although the behaviour and properties of a single sediment particles are of fundamental concern, in practice the greatest interest is in groups of sediment particles. It is necessary to determine the particle size distribution due to the non-uniformity of the sediment particle. The commonly used methods for particle size distribution are the direct measurement, the sifting method and the sedimentation method.

The direct measurement method is suitable for large particle and consists in the individual measurement of the particle. In this method, the average of the three orthogonal axis of the particle is assumed to be the particle diameter.

The sifting method is appropriate to sand, medium and small gravel particles. In this method, a sediment sample is passed through a sieve series with different mesh opening sizes. After sifting the sample and weighting the remaining sediment particles, the weighted fractions are computed in each sieve. Subsequently, a statistical analysis can be conducted by representing the weighted fractions by a size-frequency distribution curve and a cumulative frequency (Figure 2.2). Analysis of a large number of samples indicates that the size-frequency curve approximates a normal probability curve as shown in Figure 2.2-(a).

The most common terms used in describing particle size distribution are median diameter, geometric mean size, geometric standard deviation and gradation deviation. The median diameter (d_{50}) is the size

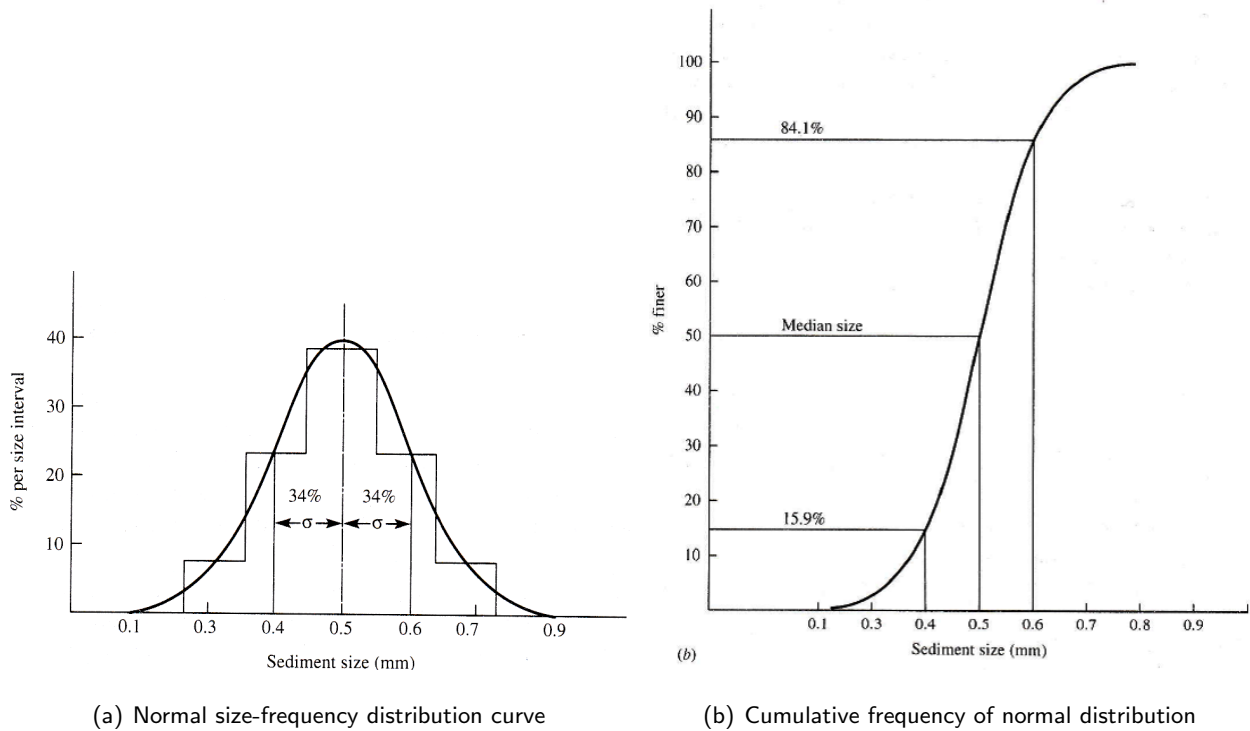


Figure 2.2: Normal and cumulative frequency curve (Yang, 2003)

of sediment for which 50% of the sample is finer. The geometric mean size (d_g) is the geometric mean of the two sizes corresponding to 84.1% and 15.9% finer, respectively. That is,

$$d_g = (d_{15.9}d_{84.1})^{1/2} \quad (2.16)$$

The geometric standard deviation (σ_g) is defined as

$$\sigma_g = \left(\frac{d_{84.1}}{d_{15.9}} \right)^{1/2} \quad (2.17)$$

The gradation coefficient (G) is defined as

$$G = \frac{1}{2} \left(\frac{d_{84.1}}{d_{50}} + \frac{d_{50}}{d_{15.9}} \right) \quad (2.18)$$

2.1.3.2 Specific Weight

Specific weight or volumetric unit gives an idea of the space occupied by deposits of sediments. It is related to the extent of consolidation of the sediment and also to the composition of the sediment mixture. Specific weight is easily obtained by weighting an amount of sediment filling a vessel with

known volume. The ratio of the sediment weight to the volume of the vessel, gives the sediment specific weight (γ_s).

2.1.3.3 Porosity

Porosity is essential in the determination of the volume of sediment deposition. It is also important in the conversion from sediment volume to sediment discharge, or vice versa. Porosity is the measure of the volume of voids per unit volume of sediment. That is

$$P = V_v/V_t = \frac{V_t - V_s}{V_t} \quad (2.19)$$

where P is porosity, V_v is volume of voids, V_t is total volume of sediment including that due to voids and V_s is volume of sediment excluding that due to voids.

2.1.3.4 Angle of Repose

The angle of repose is the slope angle formed with horizontal by granular material at the critical condition of incipient sliding. Experimental work done by Miller and Byrne (1966) has shown that the angle of repose is mainly function of various material properties such as grain shape, size and sorting of the bed as well as the ratio of particle diameter to the average bed grain diameter. The authors also concluded that the angle of repose increases with decrease in size and in sorting, in addition, the angle of repose varies from nearly 90° to less than 20° . During the bottom outlet sediment flushing the angle of repose can be used to describe the side slope of the scour hole which is excavated within the deposited sediment, if cohesive materials are absent. In case of cohesive sediments, slopes can be steeper than the angle of repose for non-cohesive material. According to Morris and Fan (1997), the angle of repose of cohesive sediment increases as a function of concentration.

2.1.3.5 Cohesive and Non-Cohesive Sediments

Cohesive sediments are very fine (less than 2 micron) negatively charge clay minerals which have a certain capacity to absorb cations (Basson and Rooseboom, 1997). They are characterised by their plasticity and cohesion due to surface physico-chemical forces. More often, deposited sediment in reservoirs contains a high percentage of clays and their interparticle cohesion forces can influence important sediment

transport parameters such as the rate of sedimentation and compaction, erosion resistance, flocculation as well as the angle of repose (Morris and Fan, 1997).

For non-cohesive sediments, particle properties such as settling velocity, particle incipient motion and erosion rate are determined by gravitational forces which are generally functions of sediment size. However the boundary between cohesive and non-cohesive sediment is not yet clearly defined and generally varies with the type of sediment (Basson and Rooseboom, 1997). Furthermore, dominance of interparticle cohesion over gravitational force increases with decreasing particle size.

2.1.4 Summary

In this section, some of the most commonly used terminology in literature, pertaining to sediment particle properties were discussed. This step was necessary because parameters describing these properties are often included in sediment transport equations. The overview on sediment characteristics is important for the description of the modes of sediment transport in rivers and also for a better understanding of the reservoir sedimentation modelling.

2.2 Sediment Transport in Rivers

2.2.1 Introduction

The flow of water over a mobile bed has the ability to entrain solid particles. Consequently, mixture from the interaction between water and sediment will displace itself in the watercourse. The material of sediment load is mainly originated by erosion of material within a catchment area. In addition landslides can also contribute to the sediment load in the stream. Sediment resulting from the erosion of catchment becomes available for transport by water flow. The river bed material displaced by the stream shear stress is also source of sediment load. The size of sediment varies along the reach and mainly depends on catchment characteristics as well as the distance of the reach to the sediment source. However, the amount of the transported sediment load is influenced by the sediment size, slope, discharge and channel and catchment characteristics. In the following sections, various sediment transport mechanisms will be presented although in most reservoirs the turbulent suspended sediment transport is the dominant mechanism of sediment transport.

2.2.2 Bed-Load Transport

Sediment transport is considered as bed-load transport if the motion of the sediment particles is rolling, sliding, or sometimes jumping along the bed. Bed-load occurs at relatively low shear stress excess and describes therefore, a movement which is generally in contact with the bed, whereby the individual particles move intermittently. Generally, the bed-load transport rate of a river is about 5 – 25% of that in suspension (Yang, 2003).

2.2.3 Suspended Load Transport

Suspended load transport occurs as the shear stress excess increases further, the amount of turbulence generated at the bed and its diffusion upwards reaches a stage where the particles lose contact with bed and are held in suspension. Furthermore, the upward diffusion of turbulence helps to maintain the particles in suspension, against gravity.

2.2.4 Wash Load Transport

Wash load transport, usually consists of transport of very fine particles of clay and silt sizes. These particles are transported into the streams by overland flow, washed off the land, and are usually not present in quantities in the bed material. Wash load can also be originated from the abrasion of sediment particles in transport. Unlike the suspended load, a certain amount of wash load is not a function of the hydraulic parameters of stream flow. The very fine particles, especially fine clay, can remain in suspension by Brownian motion, even in still water.

2.2.5 Total Load Transport

The total sediment load is the sum of bed-load, suspended load and wash load. Basically by knowing the sediment load contribution of each sediment transport mode, the total load can readily be determined. However, in many well-known sediment transport formulas such as Bagnold (1966), Engelund and Hansen (1972) and Ackers and White (1973), total load can directly be calculated using total load equations proposed by the same authors.

2.2.6 Summary

Since flow in reservoirs is brought by rivers, in this section different sediment transport mechanisms in rivers were presented and Figure 2.3 below summarises the mode of transport of sediment as well as its origin.

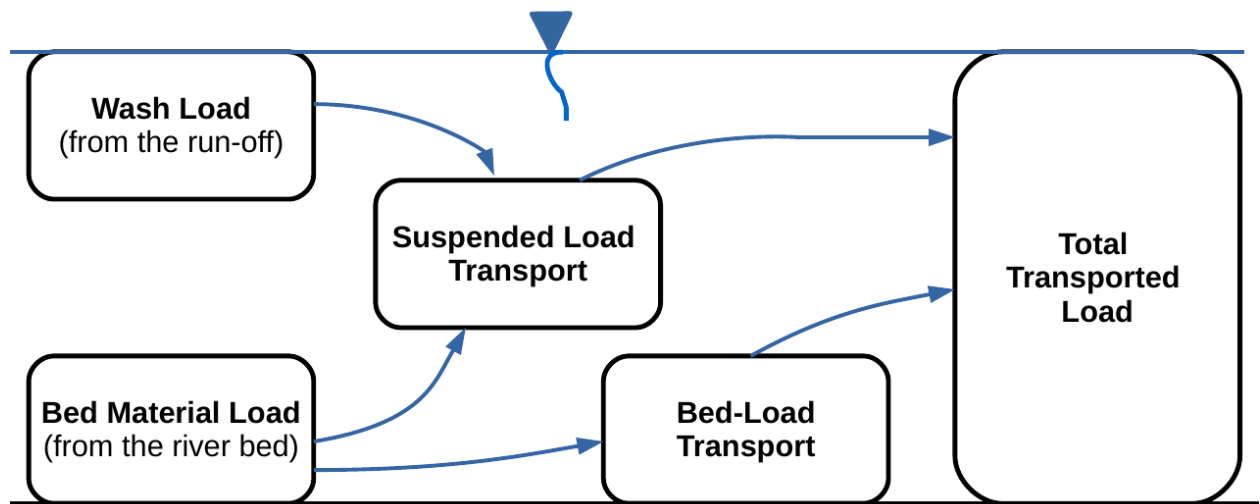


Figure 2.3: Composition of sediment transport

2.3 Reservoir Sedimentation Processes

2.3.1 Introduction

Sediment transport capacity for a river flowing in a reservoir is considerably decreased and the sediment load is directly dependent on the hydraulic conditions in the reservoir. For example, flow velocity for a river entering a reservoir decreases due to the expansion of the lateral cross sectional area of the flow and increase in depth, and subsequently sediment deposition occurs in the reservoir. In a typical reservoir, sediment deposition is spatially distributed according to their size. The coarse sediment is found in the upstream part of the storage reservoir and this particular zone refers to delta area. Fine sediments such as silt and clay fractions are transported further downstream due to their light weight and deposited near the dam.

2.3.2 Sediment Transport in Reservoirs

Sediment transport within reservoirs can be classified into three different mode of transports, namely turbulent suspended sediment transport, density currents and colloidal suspension (Basson and Rooseboom, 1997). Turbulent suspended sediment constitutes the major mode of sediment transport through most reservoirs as well as in rivers. In this mode of transport, sediment is maintained in suspension due to presence of turbulence in the flow. Some suspended load transport formulas are given in Section 2.5.

Density currents or gravity currents are flows driven by gravity acting on difference in density between the current and its surroundings (Gerber, 2008). However, differences in temperature, salinity or suspended sediment concentration can also trigger a density current flow in the reservoir because variations in the above mentioned parameters also imply variations in density. There are various types of density current such as overflow, interflow and underflow. The underflow density current is often found in reservoirs and according to Basson and Rooseboom (1997), density currents have been observed in several reservoirs such as Lake Mead, USA and Sautet Reservoir in France.

Colloidal suspensions are mainly caused by electrostatic forces exerted on small particles and their suspensions depend on both particle size and water quality. Colloidal suspended sediment size varies between 10^{-3} to 1 micron (Basson and Rooseboom, 1997). According to the same authors, large reservoirs with a large storage capacity to mean annual river flow trap most of the inflow sediment load, but about 3% of the load could spill at the dam due to colloidal suspension.

2.3.3 Sediment Deposition in Reservoirs

When the river flows into the reservoir coarser sediment fractions which consists of sand fractions or larger sizes are first deposited at the upstream side of reservoir. This leads to the formation of a delta which may increase to reach the full supply level (FSL) of the reservoir. Consequently the reservoir storage is reduced and this loss in storage capacity has a direct impact on the functioning of the dam. For example, the flood hazard upstream of the reservoir could considerably increase. The second sediment deposition area is located further into the reservoir closer to the dam. Sediment deposition in this area is composed of fine sediment fractions (clay and silt) which are generally transported through turbulent suspension. Due to its location, fine sediment deposition could cause the blockage of gates. Furthermore, sediment entrainment into a hydropower intake, especially silt and sand, could also damage the hydropower turbines.

2.3.4 Sedimentation Control in Reservoirs

In order to secure a long-term sustainability of the use of reservoirs many techniques have been developed to deal with reservoir sedimentation. Sediment management in reservoirs resulting to a long lifespan operation of reservoirs can be achieved by adopting suitable sediment control techniques to minimise the impacts of reservoir sedimentation. According to Basson and Rooseboom (1999) the following techniques can be used for reservoir sedimentation control:

Minimise sediment loads entering reservoirs through

- soil and water conservation programmes
- upstream trapping of sediment (debris dams or vegetation screens)
- bypassing of high sediment loads.

Minimise deposition of sedimentation in a reservoir through

- sluicing (passing of sediment-laden floodwaters through the reservoir by mean of drawing the water level down)
- density current venting.

Remove accumulated sediment deposits through

- flushing by mean of drawing the water level down during the rainy season
- excavation by mean of dredging or other mechanical equipment.

Compensating for reservoir sedimentation through

- maintain long-term storage capacity by raising the dam
- abandon/decommission the sedimented reservoir and construct a new reservoir or introduce water from elsewhere.

Detailed descriptions of the reservoir sedimentation control techniques listed above can be found in Basson and Rooseboom (1999) and Morris and Fan (1997). However, some reservoir sedimentation control methods are discussed in this study.

Reservoir sediment as mentioned before is not only a serious threat to water storage capacity but it could also undermine some hydraulic structures such as hydropower intakes and bottom outlets. For this reason, reservoir sedimentation has been a topic of high interest for engineers for many years. Prediction of sedimentation in reservoir, therefore, becomes crucial and could help in the planning and design of a reservoir. However, many reservoirs experience sediment deposition beyond the acceptable level. To deal with reservoir sedimentation some remedial measures exist to prevent incoming sediment from settling in the reservoir or to remove the existing deposited sediment. According to Shen (1999) the following methods can be used to reduce sediment deposition in reservoirs; bypassing flow with heavy sediment concentration from entering the reservoir, sluicing sediment through a reservoir by density currents, mechanical removal of reservoir sediment by means of dredging or siphoning.

Bypassing of sediment is a reservoir sedimentation control method in which high sediment loads are bypassed around the reservoir through a tunnel or canal. Due to its limitations in terms of topographical, hydrological or economical conditions, bypass tunnels are not widely used for reservoir sedimentation management. However, according to Sumi et al. (2004), sediment bypassing techniques have many advantages such as they can be added into existing dams and prevent a loss of water storage caused by the lowering of the reservoir water level. Furthermore, inflow discharge can pass through tunnels very naturally during flood times without a serious impact on the environment downstream. The authors also pointed out that this technique has been successfully implemented to control reservoir sedimentation in Japan as well as in Switzerland. A similar study done by Kantoush et al. (2012) on the evaluation of sediment bypass efficiency concluded that the bypass tunnel has proven to be efficient in mitigating reservoir sedimentation.

Sluicing is a process in which sediment-laden inflows are released through a dam in order to avoid the sediment particles to deposit, and therefore the trap efficiency of the reservoir is considerably decreased. Sluicing operation is carried out at low water level during the flood season. After the flood season clear water is stored by raising the reservoir water level. As reported by Basson and Rooseboom (1997), sluicing techniques were applied on various reservoirs with varying degrees of efficiency. According to the authors the following conditions have to be fulfilled for an efficient sluicing process:

- Sufficient inflow must be available for transporting sediment.
- Outlet works must be dimensioned according to reservoir capacity and be located at the original river-bed level.

- Sediment must be discharged at the right time and duration by a trained operator.
- A narrow shape configuration for the reservoir basin throughout is recommended.
- The river should transport essentially suspended sediment and possess excess capacity in order to transport through the reservoir.

Flood flushing consists of increasing the flow velocities by water level drawdown in order to first re-entrain the previously deposited sediments and then to transport sediment particles through the bottom outlet. Unlike the sluicing technique, the erosion process is observed during flood flushing operation. The width as well as the slope of the river channel will tend to the original regime conditions for periodic flushing events, depending on the reservoir shape, availability of excess water, size of the bottom outlets, judicious operation, etc. (Basson and Rooseboom, 1997). Sediment flushing could be carried out with free outflow conditions or under pressure. As pointed out by Basson and Rooseboom (2008) the following aspects need to be considered for the efficiency of the flood flushing operation:

- Outlet discharge capacity, location and elevation.
- The geometry of the reservoir (width, length, slope, storage ratio).
- Flushing discharge and its duration.
- Characteristics of inflow and deposited sediment
- Water level drawdown and duration

Shen (1999) conducted a study on flushing sediment through reservoirs and described two types of sediment flushing namely, drawdown flushing and local flushing. Drawdown flushing consists of decreasing the water level up to the topset of the sediment deposition. During drawdown flushing sediment is re-entrained leading to a general erosion of the previously deposited sediment in the reservoir. This process will excavate a channel known as flushing channel. Figure 2.4 shows the lateral sediment deposition pattern in reservoirs while Figure 2.5 depicts the reservoir bed after flushing event, including the local scour hole known as flushing cone and the flushing channel for local flushing and drawdown flushing respectively.

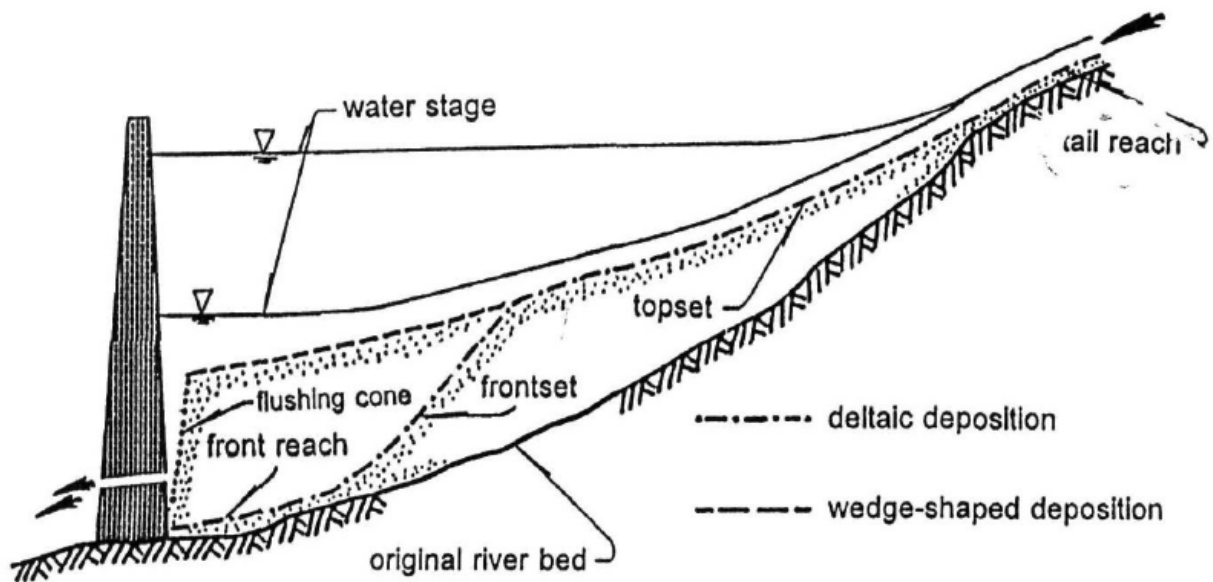


Figure 2.4: Longitudinal sediment deposition patterns in reservoirs (Shen, 1999)

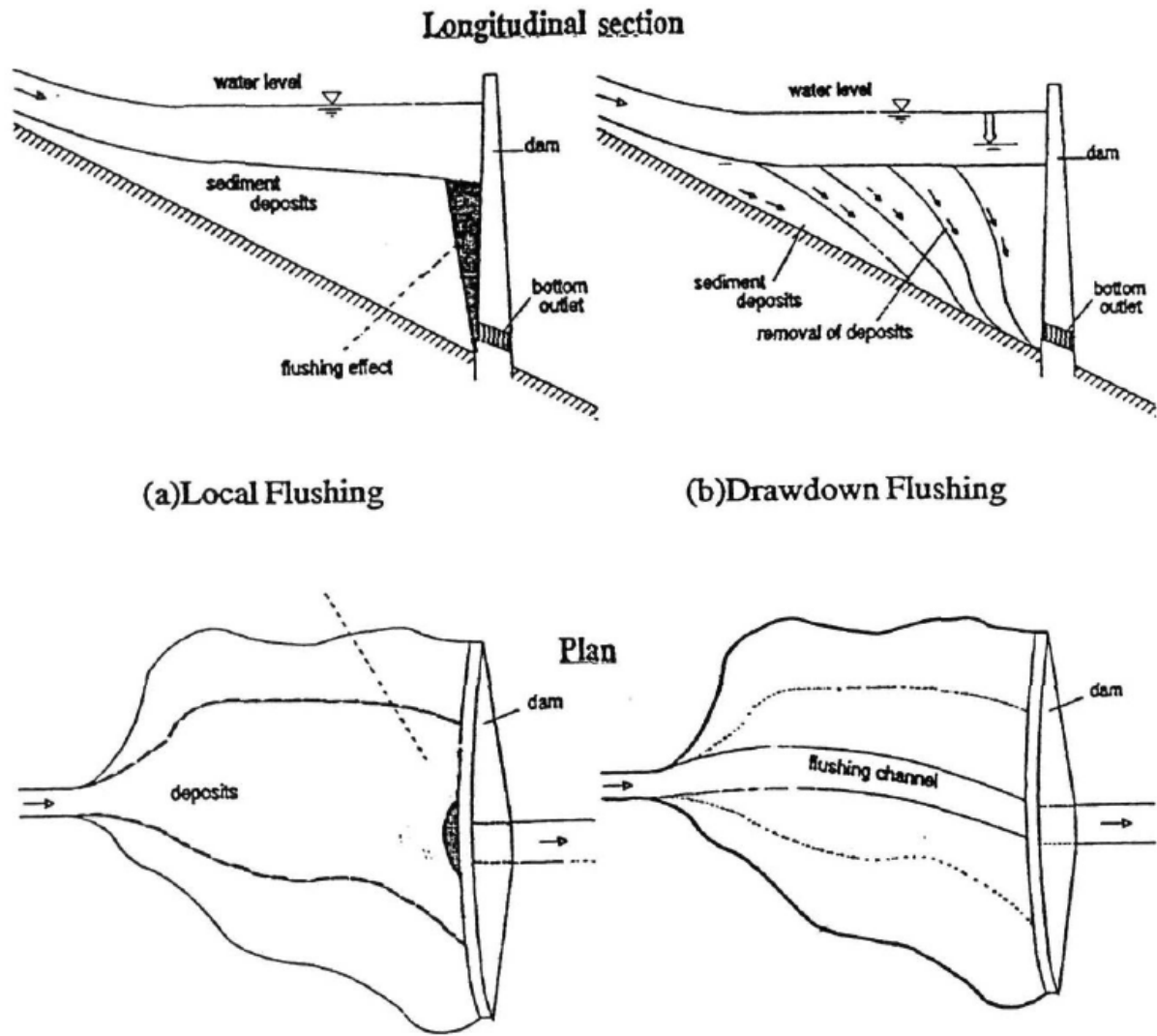


Figure 2.5: Sediment erosion during flushing operation in reservoirs (Shen, 1999)

According to Mahmood (1987), this method is suitable for narrower, gorge-type reservoirs and very effective in terms of amount of sediment removed in reservoir when the drawdown flushing is carried out over a period of several months. On the contrary, the low water condition makes this method inappropriate in case of hydropower system in which high water level in reservoir is generally required for an effective power generation.

Local flushing consists of carrying out flushing operation by fixing the water level to the minimum operating level. Consequently, the flow velocity is much less compared to the drawdown flushing method. This combined conditions leads to the development of local scour hole just upstream of the bottom

outlet. This hole has a conical shape and develops until the slope of the scour hole is equal to the angle of repose. Furthermore in this method, sediment flushing has only a localised effect (upstream of the bottom outlet) because velocities decrease proportionally to the square of the distance from the outlets (Scheuerlein, 1993). The local flushing method is appropriate where localised bed scour at intakes is required. For example in case of hydropower in which the bottom outlet is placed below the intakes could minimise the entrainment of sediment particles into the turbine (Basson and Rooseboom, 2008). It is worth noting that local flushing is discussed in detail in the present study. Firstly, a physical laboratory model of the non cohesive sediment bottom outlet flushing is investigated (see chapter 3) and secondly a coupled fully 3D numerical simulation of the bottom outlet flushing is developed and validated against laboratory data (See Chapter 4 and 5).

2.3.5 Summary

The main focus in this section was to explain deposition processes of sediment in a reservoir. In this regard, the sediment deposition pattern along the reservoir in terms of sediment size distribution was first described and then, various techniques for the removal of deposited sediment were discussed.

2.4 Overview on Bottom Outlet Sediment Flushing under Pressure

2.4.1 Introduction

Bottom outlets are very important components of a dam structure. Although a bottom outlet was historically primarily designed as a safety structure for water releases in an emergency it can also be used for the following purposes:

- Environmental flood release.
- Reservoir drawdown for sediment flushing: local or free flow flushing
- Flood discharge release

Bottom outlets can also be utilised as sediment wear protection in a turbine by initiating local flushing when it is located below the power intakes (Fan, 1985; Basson and Rooseboom, 1997). However, an in-depth research is needed to confirm the effectiveness of this method. In several existing dams outlets

have been designed with very low discharge capacities while in some cases they do not exist. In order to correct this, reconstruction of bottom outlets has been implemented on dams as reported by Basson and Rooseboom (2008). However, outlet reconstruction is found to be costly and in many cases technically challenging (Delft, 1992). To achieve this, special attention should be given to the analysis of hydraulic conditions of the bottom outlet in order to design suitable outlets capable of withstanding high flows and high sediment load events.

Basson and Rooseboom (1997) suggested the following rules for the design of a bottom outlet:

- The orifice of the outlet should be dimensioned to pass a 5 to 10 year Annual Recurrence Interval flood without inundation of floodplains and with moderate deposition. This design consideration results in very large and costly outlet structures in most cases.
- The bottom outlet elevation should be at the original river bed level. This will allow effective flushing of suspended sediment load with high concentrations near the bed. Furthermore, coarse sediments are also re-entrained through the flushing process.
- More than one outlet are recommended in case of hydropower system and the spacing between them should be such that the local scour zone upstream of outlets covers all the intakes to turbines.
- The bottom outlets should be large enough relative to the outlet tunnel length and the initial depth of the sediments above the outlet in order to avoid blocking of the outlets by debris or sediment deposition.
- Abrasion-resistant material should be used to coat the outlets for protection against a potential abrasive action of flushing sediment.

The bottom outlet dimension can be determined using the following equation proposed by United States Bureau of Reclamation (USBR, 1987)

$$H = K_1 H_v \quad \text{or} \quad H = K_2 \frac{Q^2}{A^2} \quad (2.20)$$

where H denotes the total available head, H_v is the velocity head, K_1 and K_2 are coefficients, Q is the outlet discharge and A is the required area of the outlet orifice. From Equation 2.20 it can be noticed that for a given constant total head H the outlet discharge Q increases with the increase of the outlet area A . Therefore the use of a bottom outlet with a large orifice should improve the sediment flushing

effectiveness. A similar equation known as the submerged flow/orifice equation gives a relationship of the bottom outlet discharge Q , with both total head H and the outlet area A and reads

$$Q = C_c A \sqrt{2gH} \quad (2.21)$$

where C_c is the contraction coefficient of discharge for submerged or tube flow and g is the gravitational constant. The contraction coefficient is defined according to the outlet orifice shape. For sharp edges $C_c = 0.6$ while $C_c = 0.8$ in the case of rounded edge (SANRAL, 2013).

2.4.2 Previous Studies done on Bottom Outlet Flushing

The scour downstream of hydraulic structures such as stilling basins, diversion work, river barrages has been an important topic of interest for engineers due to its frequent occurrence in engineering applications. However, there are few studies in literature with main focus on the behaviour of the flow as well as the sediment transport processes just upstream of the bottom outlet structures. The velocity field upstream of a bottom outlet orifice was investigated by Shammaa et al. (2005) and this study found that the shape of velocity contours near the outlet orifice are semi-ellipsoidal and became more hemispherical and approaching uniformity further away from the orifice. Furthermore, the observed velocity magnitude decreases rapidly from the orifice to a distance approximately equal to the outlet diameter in the opposite direction of the flow. In addition, it was found that beyond a certain distance the size and the shape of the bottom outlet do not impact the behaviour of the flow field as shown in Figure 2.6

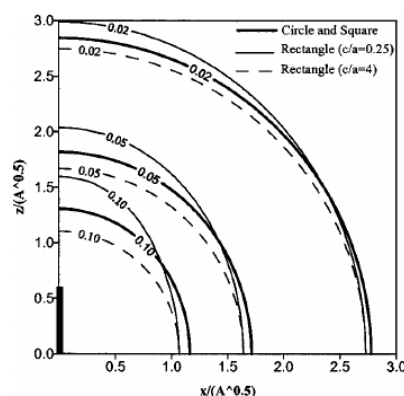
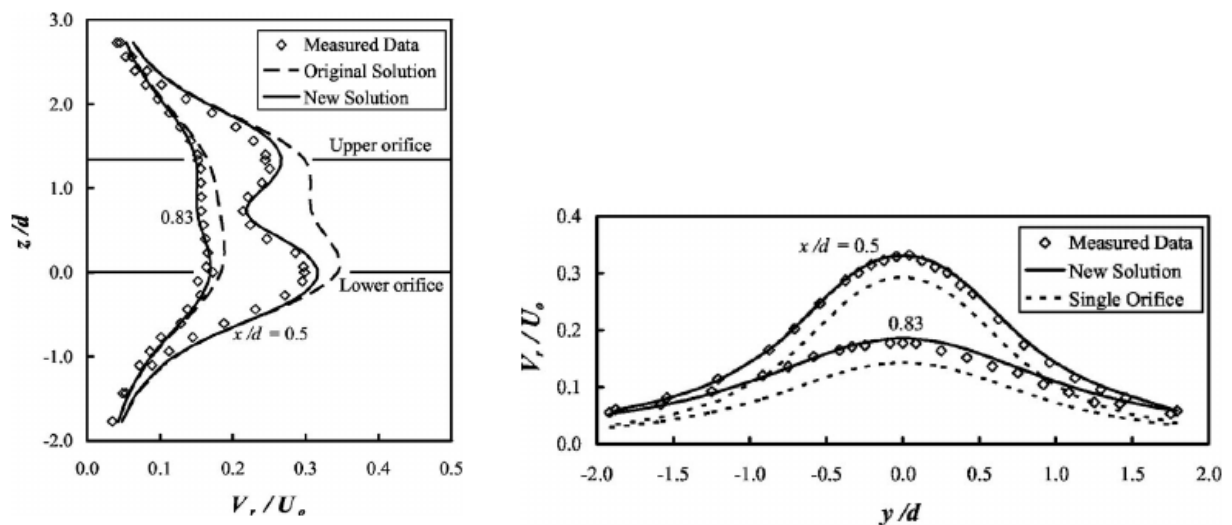


Figure 2.6: Isovelocity contours upstream of orifices of different shapes (Shammaa et al., 2005)

Shammaa et al. (2005) reached the above mentioned results by using the potential flow solution method. This method consisted of a distribution of point or line sinks over the surface of an orifice or sluice gate opening in order to determine the velocity field upstream of the bottom outlet.

A similar approach to Shammaa et al. (2005) method was adopted by Bryant et al. (2008) to investigate the flow pattern upstream of orifices. A new potential flow solution method was therefore developed by Bryant et al. (2008) in which pressure gradient effects close to orifices and the superposition of the solution from multiple orifices were included. A physical model tests, including first, the small size orifices with three cases; first test without the influence of surface or bottom boundary, the second test consisted in placing the orifice near the surface and in the third test two orifices were chosen to be close to each other. For the large size orifice case, the orifice was located far away from the surface and bottom boundaries. Based on comparisons between results from these experimental tests and the new potential flow solution method Bryant et al. (2008) concluded that the new proposed method improved prediction of the velocity profiles near the orifice for one orifice condition as well as multiple orifices conditions as depicted in Figure 2.7.



(a) Vertical velocity profile comparison

(b) Horizontal velocity profile comparison

Figure 2.7: Velocity profile comparison with measurement (Bryant et al., 2008)

Rajaratnam and Humphries (1982) studied velocity behaviour upstream of vertical sluice gates through an experimental rectangular channel setup as well as the geometrical properties of the surface eddy or recirculation region and the pressure defect on the bed. Figure 2.8 depicts the different velocity profiles

upstream of the sluice gate and the surface eddy as observed during the experimental test conducted by the same authors.

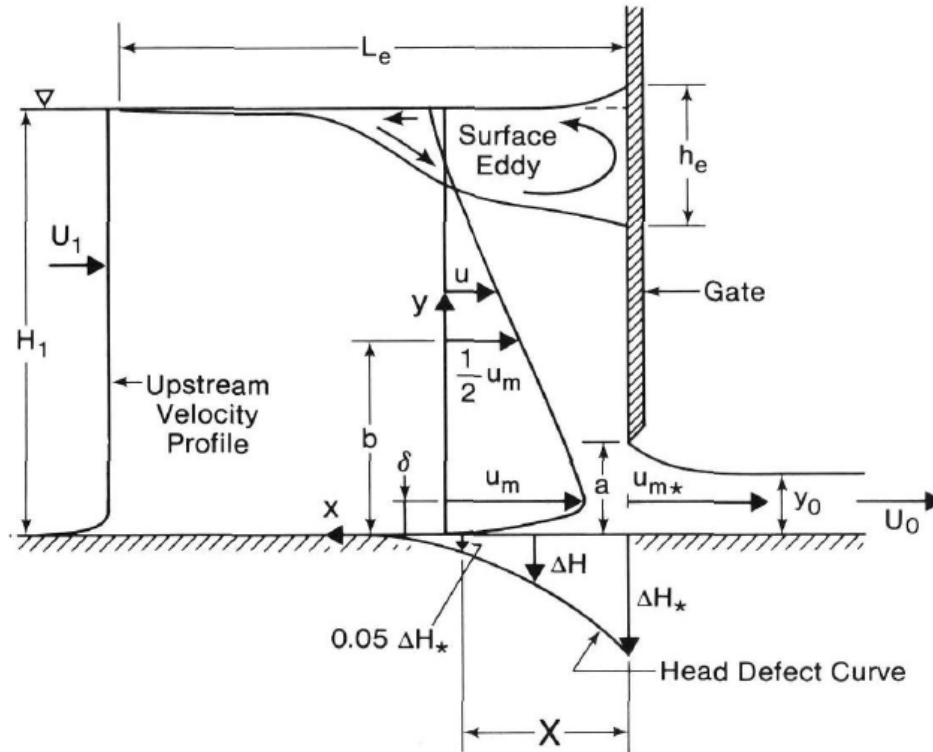


Figure 2.8: Flow through a sluice gate - definition sketch (Rajaratnam and Humphries, 1982)

Firstly, it was found in this experimental study that turbulent flow has occurred at the downstream end of the surface eddy while at the upstream end the flow was laminar within the recirculation region. Secondly, due to high flow acceleration through the gate opening, Rajaratnam and Humphries (1982) concluded that the pressure defect (pressure loss) on the bed decreases from the gate location and reaches zero at an upstream distance approximately five times the gate opening as shown in Figure 2.9. The third conclusion drawn from this study was that the velocity distribution becomes uniform after the flow crosses the gate opening. In addition, for less than about four times the gate opening the profile of the longitudinal component of the velocity has a shape of a wall jet in which the velocity increases with respect to the vertical distance up to a maximum value and then decreases as the vertical distance increases (see Figure 2.10).

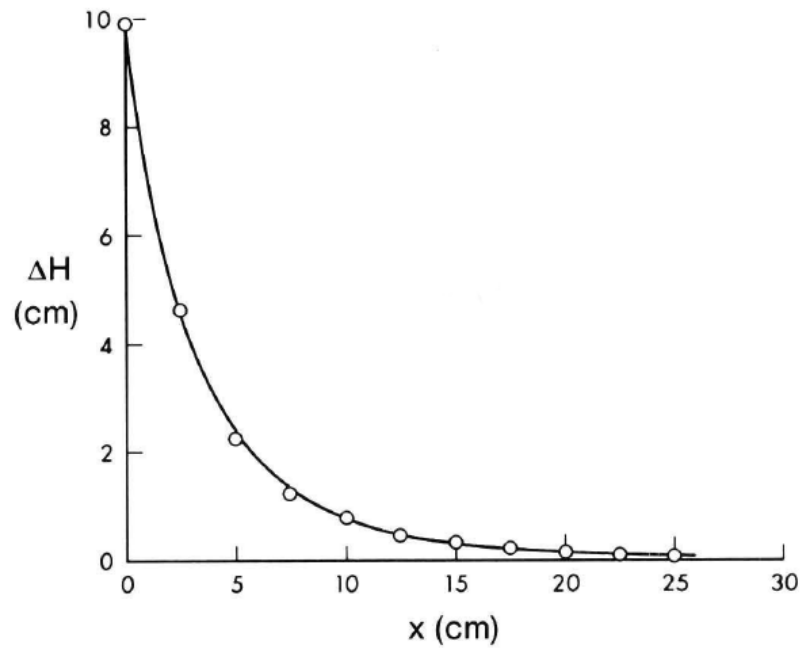


Figure 2.9: Pressure head dropped on the bed (Rajaratnam and Humphries, 1982)

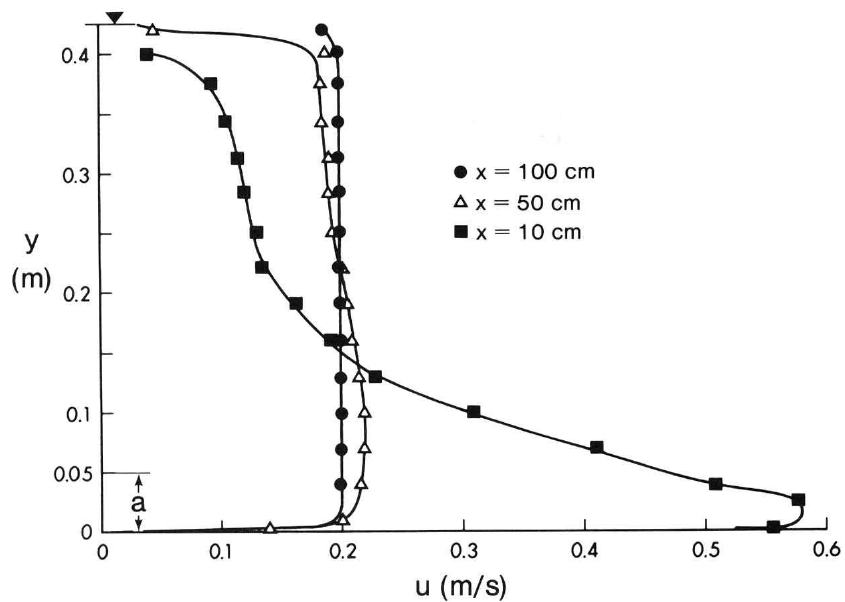


Figure 2.10: Typical velocity upstream of the gate (Rajaratnam and Humphries, 1982)

Most of previous research studies that have been conducted on bottom outlets and presented above deal only with the flow field behaviour upstream of the outlet/slucice gate. However, the following studies will specifically deal with the scour development upstream of the bottom outlet due to the flushing process.

Powell (2007) investigated both sediment transport and flow behaviour upstream of orifices through a laboratory setup. The experimental study included a circular bottom outlet and the bed in the model consisted of non-cohesive uniform sand. Unlike previous experimental studies on bottom outlets, the packed bed inside the physical model was levelled with the invert of the orifice. The same procedure was followed in the physical model presented in the present study (see Chapter 3). After running several test cases by varying the sediment sizes and water level above the orifice, Powell (2007) concluded that on one hand initial inception motion of sediment was driven by high shear stress and on the other hand the equilibrium state of the scour hole was governed by a vortex system that developed in the vicinity of the bottom outlet. Furthermore, based on measurements taken during the experimental tests the same author derived the non-dimensional relationships for predicting maximum scour depth and maximum scour length and width (see Equations 2.22 to 2.24)

$$SD_{C-M} = \frac{18576 \frac{H}{D} + 33273}{\frac{\rho U_0}{\mu} \left(\frac{d_{50}}{H} \right)^{0.1}} \quad (2.22)$$

$$SL = \frac{72017 \frac{H}{D} + 45656}{\frac{\rho U_0}{\mu} \left(\frac{d_{50}}{H} \right)^{0.1}} \quad (2.23)$$

$$SW_M = \frac{55789 \frac{H}{D} + 144557}{\frac{\rho U_0}{\mu} \left(\frac{d_{50}}{H} \right)^{0.1}} \quad (2.24)$$

where SD_{C-M} , SL and SW_M are maximum scour depth, scour length, and scour width, respectively along the orifice centreline, H is the head over the orifice, D is the diameter of orifice, ρ and μ are the density and the dynamic viscosity of the fluid, U_0 is the average orifice velocity and d_{50} is the sediment size.

Meshkati et al. (2009) investigated the temporal evolution of the flushing cone upstream of a bottom outlet during the pressurised flushing in a reservoir. For this purpose, a laboratory model was set up and experimental tests were conducted for various flow conditions using a uniform silica bed and

geometric properties of the flushing cone such as the maximum width, length and depth were measured. These measurements were subsequently used for dimensional and regression analysis in order to derive equations for temporal variations of flushing scour dimensions.

A similar laboratory experiments was conducted by Meshkati et al. (2010) to analyse the local scour hole upstream of bottom outlet for different outlet diameters. Three bottom outlet diameters with five discharges and three different water depths relative to the centre of the bottom outlet were tested. Results from these experimental tests were used for regression analysis which led to dimensionless equations (Equations 2.25 and 2.26) for calculating the volume of the removed sediment as well as to the prediction of the width of the flushing cone.

$$\frac{V_s}{H^3} = 4.6 \left(\frac{U_0}{\sqrt{g(G_s - 1)d_{50}}} \right)^{0.21} \left(\frac{H_s}{H} \right)^{2.2} \left(\frac{D}{H} \right)^{0.89} \quad (2.25)$$

$$\frac{W_s}{H} = 0.02 \left(\frac{U_0}{\sqrt{g(G_s - 1)d_{50}}} \right)^{0.1} \left(\frac{H_s}{H} \right)^{0.75} \left(\frac{D}{H} \right)^{0.34} \quad (2.26)$$

where V_s and W_s are respectively the volume and the width of the flushing cone, H_s is the deposited sediment height above the centre of the bottom outlet, g is the gravitational acceleration and G_s is the relative density.

Furthermore, results from these laboratory tests indicated that the cross section area of the bottom outlet is strongly correlated with the flushing cone dimensions since the flushing scour hole dimensions increase with the increase of the diameter of the bottom outlet.

Emamgholizadeh et al. (2006) also investigated the effect of both the discharge and the water depth at the bottom outlet on the pressure flushing efficiency. For this investigation, laboratory experiments were carried out and three separate non-cohesive sediment sizes were used in the physical model. The authors concluded that the amount of removed sediment during flushing process increased with the increase of the flow exiting the bottom outlet and the decrease of the water depth in the reservoir near the bottom outlet. In addition, the same authors indicated that under the same flow conditions when the sediment size decreased (from coarser to finer size) the quantity of the removed sediment increased.

In a similar study, Dodaran et al. (2012) experimentally investigated the effect of localised vibrations in sediment layers on the geometric parameters of the flushing cone. The experimental tests were conducted with two different outlet diameters, five flow rates, three different frequencies of vibrations with three distinct position of the vibrators. The water depth relative to the centre of the bottom outlet was the same for all experimental tests. Dodaran et al. (2012) showed that vibration frequency

and the cross section area of the bottom outlet are correlated to the flushing cone dimension since the results indicated that when the vibration frequency and the diameter of the bottom outlet increase the scour hole becomes larger and extends further from the outlet. In addition, in the same study, it was proven that an appropriate position of the vibrators, which is defined as the optimum vibrator positions could improve the efficiency of the flushing operation. From the experimental results, the above-mentioned positions are located at the maximum flushing length and width for an experimental case without vibrators.

Laboratory experiments consisting of a one-dimensional reservoir model were conducted by Talebbeydokhti and Naghshineh (2004) to analyse the flushing processes by using polymer particles to model a very fine and non-cohesive sediment. Results from the experimental tests showed that the scour hole upstream of the bottom outlet was conical and symmetrical. In addition, the flushing channel started with a meandering effect at the beginning of the flushing process. According to Talebbeydokhti and Naghshineh (2004), these observations agreed with experimental data found in the literature.

In 1993, Scheuerlein proposed a simplified analytical approach in order to identify the governing parameters of flushing process as well as to estimate its efficiency (Scheuerlein, 2004). This method was mainly based on the continuity equation applied on a three-dimensional grid of streamlines and isotachs combined with some stability criteria of sediment deposit against erosion due to water flow (see Figure 2.11).

From the simplified analytical approach the following equation was derived

$$\frac{r}{D_G} = \frac{1}{2} \sqrt{\frac{\mu_G (2gH_0)^{0.5}}{v_r}} \quad (2.27)$$

where r is the radial distance of a sphere-shaped isotach from the bottom outlet, D_G is the diameter of the bottom outlet, μ_G is a loss coefficient at the outlet, H_0 is the pressure head above the outlet, g the gravitational acceleration and v_r the flow velocity at distance r .

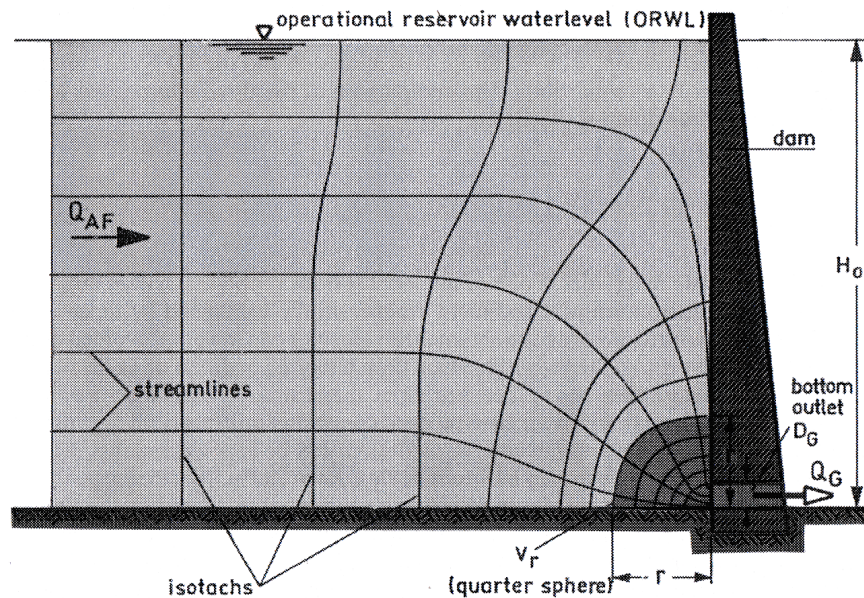


Figure 2.11: Simplified flow pattern at bottom outlet (Scheuerlein, 2004)

Although physical models were extensively used to study the bottom outlet flushing process, several numerical models have also been used to investigate sediment flushing in reservoirs. However, the majority of these mathematical models were one-dimensional numerical modelling (Shen, 1999). Peng, Niu and Ju (reported in Shen, 1999) developed a one-dimensional numerical model based on the diffusion equation to predict the removed sediment volume, bed profile changes and the flushing channel width during the flushing event under a constant discharge. A similar one-dimensional diffusion model which is able to simulate the general trend of bed profile changes as well as the amount of removed sediment was proposed by Lai and Shen (1996) to investigate the flushing processes during drawdown operations.

A two-dimensional numerical model based on the finite volume method and capable of modelling sediment transport under unsteady flow condition was developed by Lai (reported in Shen, 1999) to simulate flushing channel formation during flushing sediment processes in reservoirs. In order to simulate flushing of sediments from reservoirs, Olsen (1999) developed a two-dimensional numerical model that solves depth-averaged Navier-Stokes equations in conjunction with a zero-equation turbulence model. In this model, the sediment concentration is calculated using a convection-diffusion equation. Furthermore, the simulated flow field was extrapolated to three dimensions and the secondary currents were not modelled. However, according to the author, the model was able to reasonably simulate physical model cases.

Scheuerlein (2004) made use of a three-dimensional numerical model to investigate the removal of

sediment deposits from reservoirs. Based on Finite Volume Method (FVM) this numerical model solves the Reynolds-averaged Navier-Stokes equations in conjunction with $k-\varepsilon$ turbulent model to compute the flow fields. The sediment transport is computed using the convection-diffusion equation in combination with Van Rijn's (1984b) equation for sediment concentration near the bed and bed load transport proposed by Van Rijn (1984b). The numerical model results were compared with results from the simplified analytical approach (Scheuerlein, 1993) and the model successfully predicted flushing operation under high water level. However, for water level drawdown conditions the model provided a poor prediction compared to the simplified analytical approach.

2.5 Theoretical Considerations of Suspended Load Transport

2.5.1 Introduction

The sediment transport confined to bed load is only affected by a relatively small value of shear stress excess. Increase in bed shear stress leads to suspension and transport as bed and suspended load. Since suspended sediment is transported at the same velocity as the flow, the quantity of sediment transported as suspended load is usually much greater than that of bed load which moves slowly. According to Raudkivi (1998), the spreading of suspended matter arises from one or more of the following causes:

- Scattering due to random molecular motion of the host fluid.
- Turbulent mixing.
- Spreading due to systematic differences in the velocity in the cross section of the stream or by convecting currents.

The spreading of suspended sediment due to random molecular motion and turbulence is referred to as diffusion or dispersion whereas that due to velocity gradients is known as convective dispersion or gradient diffusion. The colloidal particle sizes are primarily affected by the random molecular motion also known as Brownian motion. Silt and sand sizes are maintained in suspension against the gravitational fall velocity by diffusion of turbulence from the bed or by internal current in a convection process. Unlike the diffusion process, little progress has been made with quantitative studies of the convective suspension.

Different models describing sediment in suspension found in the literature, are presented in the following sections.

2.5.2 Diffusion Models of Suspension

Diffusion models are mostly based on the continuum hypothesis and Fick's law which is given as

$$P = -D \frac{\partial C}{\partial y} \quad (2.28)$$

where P is the rate at which the quantity or property is transported across unit area normal to y -direction, D is the coefficient of diffusion or diffusivity and c is the concentration of the same quantity transported by diffusion. In turbulent flow and addition of gravitational settling velocity (ω_s) term, Fick's law is rewritten as

$$\frac{\partial c_m}{\partial t} + u_{im} \frac{\partial c_m}{\partial x_i} = \frac{\partial}{\partial x_i} \left(D_{ij} \frac{\partial c_m}{\partial x_j} + D_M \frac{\partial c_m}{\partial x_i} \right) + \frac{\partial(\omega_s c)}{\partial y} \quad (2.29)$$

where D_M refers to molecular diffusion, and D_{ij} is the turbulent eddy diffusivity tensor. Generally D_{ij} is much larger than D_M so that D_M can be neglected. In the theoretical models for sediment suspension the following assumptions are made; the concentration is a function of elevation y only and independent of longitudinal or lateral coordinates, the continuity for solids and fluid must be satisfied and usually a steady state is assumed. Therefore, at any elevation within the flow the downward convective movement at settling velocity is balanced by the upward convective velocity due to diffusion of turbulence.

For steady flow with low sediment concentration, suspension of one particle size only at constant settling velocity (ω_s), Equation 2.29 is reduced to

$$\omega_s \frac{\partial c}{\partial y} + \frac{\partial}{\partial y} \left(\varepsilon_s \frac{\partial c}{\partial y} \right) = 0 \quad (2.30)$$

where ε_s is the diffusion coefficient for sediment. Integrating Equation 2.30 once yields

$$\omega_s c + \varepsilon_s \frac{\partial c}{\partial y} + A = 0. \quad (2.31)$$

Assuming that the concentration at the water surface is zero leads to $A = 0$ and then Equation 2.31 is reduced to

$$\omega_s c + \varepsilon_s \frac{\partial c}{\partial y} = 0 \quad (2.32)$$

which is usually the starting point of analyses of sediment suspension problems. From Equation 2.32, the concentration distribution is deducted and given by

$$\ln \left(\frac{c}{c_a} \right) = -\omega_s \int_a^y \frac{dy}{\varepsilon_s} \quad (2.33)$$

where a is a reference level at which $c = c_a$ is known. The form of the concentration profile mainly depends on both the velocity distribution and the diffusion coefficient (ε_s) and by assuming that the diffusion coefficient is constant leads to

$$\frac{c}{c_a} = \exp \left[-\frac{\omega_s}{\varepsilon_s} (y - a) \right]. \quad (2.34)$$

By assuming that $\varepsilon_s = \varepsilon$, where ε is the momentum diffusion in fluid, Rouse (1937) proposed the most widely known solution of the diffusion equation (Equation 2.30). By using the parabolic distribution form of the momentum diffusion (ε) given as

$$\varepsilon = \kappa u_* y \left(1 - \frac{y}{y_0} \right) \quad (2.35)$$

where κ is the Karman constant, and setting the integrand dy/ε in Equation (2.33) as

$$\frac{dy}{\varepsilon} = \rho \frac{\frac{du}{dy}}{\tau_0 \left(1 - \frac{y}{y_0} \right)}$$

and then integration yields the concentration profile given by Rouse (1937)

$$\frac{c}{c_a} = \left[\frac{a(y_0 - y)}{y(y_0 - a)} \right]^Z \quad (2.36)$$

where $Z = \omega_s/\kappa u_*$ and sometimes called Rouse number. The concentration profiles according to Equation (2.36) are depicted in Figure 2.12.

For a given shear velocity, Z is proportional to ω_s and as a result, fine sediment has a small Z value and the particles are distributed fairly uniformly throughout the depth. A substantial variation in concentration over the depth is observed for coarse sediments as shown in Figure 2.12. For a given sediment with a constant settling velocity (ω_s), an increase in shear velocity leads to increased uniformity of concentration over the depth.

Van Rijn (1984a) proposed a concentration profile formula similar to Rouse's Equation (2.36) by dividing the flow depth into two parts and used a parabolic distribution form of the momentum diffusion (ε) (Equation 2.35) in the lower half of the flow and the a constant ε in the top half. This leads to the following concentration profile over the flow depth

$$\frac{c}{c_a} = \left[\frac{a(y_0 - y)}{y(y_0 - a)} \right]^Z \quad \text{for } y/y_0 < 0.5 \quad (2.37a)$$

$$\frac{c}{c_a} = \frac{a}{y_0 - a} \exp \left[-4Z \left(\frac{y}{y_0} - 0.5 \right) \right] \quad \text{for } y/y_0 \geq 0.5 \quad (2.37b)$$

where $Z = \omega_s/\beta \kappa u_*$ and β is the differences between diffusion of solids and fluid as defined by Van Rijn (1984a). According to the same author, Equations (2.37a) and (2.37b) are only valid for $c < c_a < 0.001$.

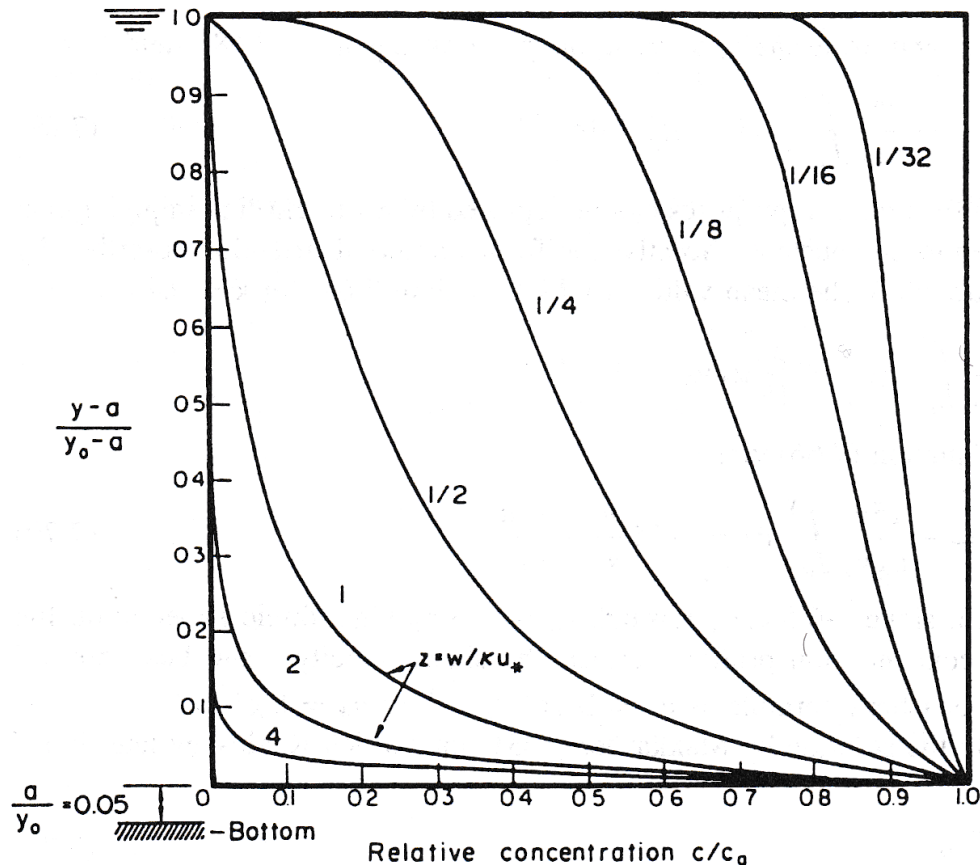


Figure 2.12: Distribution of suspended load in a flow (Raudkivi, 1998)

2.5.3 The Energy Approach of Suspension

The energy approach of suspension problems also known as the gravitational theory was developed by Velikanov (reported in Raudkivi, 1998). According to the author, suspension by diffusion involves energy, and energy dissipation of flow is an irreversible transformation of energy via turbulence into heat. Furthermore, the kinetic energy of turbulence provides the energy needed to maintain a suspension of sediment. Assuming logarithmic velocity distributions and that shear stress varies linearly with depth, Velikanov (reported in Raudkivi, 1998) obtained the following concentration profile formula

$$\frac{c}{c_a} = \exp \left\{ -\frac{\omega_s k_s \Delta}{u_* S} \int_{\eta_0}^{\eta} \left[(1 - \eta) \ln \frac{\eta}{a} \right]^{-1} d\eta \right\} \quad (2.38)$$

where the limits of integration are from η_a , a reference level, to $\eta = y/y_0$ and $a = k_s/30y_0$. The agreement of equation (2.38) with observed results is of the same order as in Equation (2.36) from Rouse in the diffusion approach (Raudkivi, 1998).

By stating that the rate of energy input per unit volume to a flow of water-sediment mixture must be equal to the power of fluctuations, the rate of energy dissipation through motion and collisions of particles, flow distortion and dissipation by water, Itakura and Kishi (1980) proposed

$$\frac{c}{c_a} = \left[\left(\frac{y_0 - y}{y_0 - a} \right)^{1-\varphi} \frac{a}{y} \right]^Z \quad (2.39)$$

where $Z = \omega_s / \kappa u_*$, $\varphi = ay_0 / L$, $L = u_*^3 (\kappa g \Delta \omega_s c)$ and a is an experimental constant. Although the application of Equation (2.39) to laboratory data yields good results, no studies involving field data are known (Raudkivi, 1998).

2.5.4 Statistical Models of Suspension

Owing to the fact that suspension is maintained by turbulence which is a random process, suspension can be described by probabilistic methods. Furthermore, the diffusion equation used to describe suspension can be expressed in the form of a random functions where concentration (c) is interpreted as probability of occurrence of a single particle in a given unit volume. Early studies on sediment suspension using statistical methods made an attempt to relate the particle motion to turbulence. Although numerous researchers have published on statistical methods for analysis of suspension, the statistical models have not established themselves in suspended sediment studies or predictions (Raudkivi, 1998).

2.5.5 Numerical Models of Suspension

Numerical models, known as mathematical models, are powerful tool for the analysis of suspended sediment problems. Based on momentum and mass balance equations for fluid and sediment, numerical methods enable the use of more complex descriptions of turbulent mixing. A turbulence model is essential because it defines the fluid and sediment mixing coefficients, which are solved numerically using a finite differences procedure and appropriate boundary conditions. Boundary condition involves the description of the exchange of sediment between the bed and suspension. From the Reynolds' equations by applying a k - ε turbulence model, where k is the kinetic energy of turbulent motion per unit mass and ε the rate of dissipation, the fluid mixing coefficients can be calculated. In numerical models, the combination of both Reynolds' equations and the k - ε model is usually used and has proven to yield a good description for velocity fields. Calculations of mixing coefficients in non-uniform flow were presented by Alfrink and Van Rijn (1983).

The numerical model approach is the method used in the present study to analyse turbulent suspended sediment in reservoirs and therefore, more details will be given in the subsequent chapters dealing with numerical modelling.

2.5.6 Summary

This section discussed empirical consideration of the suspended-load transport by giving various approaches to define the suspended sediment concentration profile in the flow. Suspended sediment transport is part of the scope of the present study. Therefore, numerical modelling dealing with suspended sediment in reservoirs which is able to predict sediment concentration profiles, is developed and presented in Chapters 6 and 7.

2.6 Overview on Mathematical Modelling of Turbulent Suspended Sediment Transport

2.6.1 Introduction

Because of the complexity of sediment transport processes, all existing sediment transport formulas are empirical or semi-empirical. Based on these formulas several mathematical models have been developed in the past to simulate reservoir sedimentation and sediment transport processes. Therefore, evaluation of their performance in various situations is very important. Many models exist that are able to simulate turbulent sediment transport in a reservoir. Some of these models are discussed in the following sections.

2.6.2 One-Dimensional Models

Mathematical one-dimensional (1D) models are mostly used in river and reservoir applications around the world. These models are able to simulate large reaches of rivers or reservoirs due to the simplicity of the formulation and the few requirements of computer resources. However, the main shortcomings of 1D models are the inability of simulating curved flows and recirculating zones or secondary flows. The 1D models also remain limited in terms of predicting suspended sediment distribution conveniently. As an example, the lateral profile of the suspended sediments inside the reservoir is not described. According to Campos (2001), 1D models exclusively developed for reservoir application have been available since

the end of the 1970s and some of them are reviewed below.

2.6.2.1 HEC-6 Model

HEC-6 is a general one-dimensional sediment transport model developed by the US Army Corps of Engineering in the early 1970s. The model was designed for the analysis of long-term river and reservoir behaviour. It is capable of computing scour and deposition by simulating the interaction between the hydraulics of the flow and the rate of sediment transport (U.S Army Corps of Engineers, 1972).

2.6.2.2 Mike11 Model

MIKE 11 is a 1D river model developed by the Danish Hydraulic Institute (DHI). It is able to simulate water flow and sediment transport in rivers and also in reservoirs. The computational core of MIKE 11 is a hydrodynamic simulation engine and it has a wide range of additional modules and extensions that cover almost all aspects of river modelling.

2.6.2.3 CCHE1D Model

CCHE1D is a 1D flow and sediment transport model for channel networks developed by the National Centre for Computational Hydroscience and Engineering (NCCHE) at the University of Mississippi. The model is able to compute unsteady flows in channels and also non-equilibrium transport of non-uniform sediment mixture. The CCHE1D model can be a valuable predictive tool for the evaluation of flow and sedimentation processes in primarily agricultural watersheds (Wu and Viera, 2002).

2.6.2.4 RESSASS Model

RESSASS (Reservoir Survey Analysis and Sedimentation Simulation) is a 1D model based on the equations that describe flow and sediment movement. The model can quantify reservoir storage volume reductions due to sedimentation, and the impact of reservoir operating policies on these losses.

2.6.2.5 GSTARS3 Model

GSTARS3 (Generalized Sediment Transport model for Alluvial River Simulation) is a 1D numerical model for simulating the flow of water and sediment transport in alluvial rivers which has been developed by the Sedimentation and River Hydraulics Group of the Technical Service Centre, U.S. Bureau of Reclamation, Denver. The model is composed of four major modules namely; the use of both the energy and the momentum equation for backwater computations, the use of the stream tube concept for sediment routing computations, the use of the theory of minimum energy dissipation for channel width and depth adjustments, and the inclusion of a channel bank side stability criteria for sediment continuity computations (Yang and Simoes, 2003).

2.6.3 Two-Dimensional Models

The two-dimensional (2D) horizontal plane models are considered as a particular case of the three-dimensional (3D) models. Therefore they are used as an initial step in the 3D models. The 2D models are being gradually upgraded to or replaced by the 3D mathematical models. Several 2D hydrodynamic and sediment transport models have been developed and some of them are discussed below.

2.6.3.1 MIKE21C Model

MIKE 21C is a numerical model that simulates the development in the river bed and channel plan form in two dimensions. Like the MIKE11, it was developed by the DHI. In its basic form the model is a 2D hydrodynamic model that can simulate dynamic as well as quasi-steady or steady-state hydrodynamic solutions. MIKE 21C uses the traditional division of sediment transport into bed load and suspended load, and the model can simulate both non-cohesive and cohesive sediment in a mixture (DHI, 2003). The sediment transport and hydrodynamics are coupled in MIKE 21C model.

2.6.3.2 CCHE2D Model

The CCHE2D is an analysis model system for unsteady, turbulent free surface flow, sediment transport and water quality evaluation. It is a depth-integrated 2D hydrodynamic and sediment transport model based on a variant of the finite element method (Wu, 2001). The model is used for application in the areas related to predicting river bed and bank erosion for both uniform and non-uniform sediment. The

sediment transport and hydrodynamics are not coupled in CCHE2D model.

2.6.3.3 SUTRENCH-2D Model

SUTRENCH (Suspended sediment Transport in Trenches) is a finite-volume hydrodynamic and sediment transport model developed by Van Rijn and Tan (1985) for simulating sediment transport and associated bed level change under conditions of combined quasi-steady currents and wind-induced waves over a sediment bed. The model solves the general advection-diffusion equations by incorporating a lag coefficient to account for the settling of sediments.

2.6.3.4 TABS-2 Model

TABS-2 is a group of finite-element type model based on hydrodynamic and sediment transport computer codes which are applicable to rivers, reservoirs and estuaries. The model is composed of the hydrodynamic component, the sediment transport component and the water quality component (Thomas and McAnally, 1985).

2.6.3.5 MOBED2 Model

MOBED2 (Mobile Bed) is a 2D finite-difference hydrodynamic and sediment transport model used in a curvilinear coordinate system, developed by Spasojevic and Holly (1990). The model can simulate water flow, sediment transport, and bed evolution in natural waterways such as reservoirs, estuaries, and coastal environments where depth averaging is appropriate. The 2D numerical models, as pointed out by Papanicolaou et al. (2008), cannot capture the hydrodynamic and sediment processes associated with secondary flow, vertical acceleration around structures, etc. However, they offer the possibility of a relatively long-term unsteady simulation when their simplifying assumptions are appropriate for the problem under study.

2.6.4 Three-Dimensional Models

The largest difference between 3D and 2D models is that 2D models can only simulate depth-averaged flow fields and sediment concentration fields, while 3D models can predict flow fields and sediment concentration fields at different water depths or elevations. Furthermore, a 3D sediment transport

model is necessary to compute lateral bed-load transport of sediments and erosion-deposition process. Three-dimensional mathematical models are commonly used for modelling water-quality issues, sediment distribution in stratified reservoirs (thermal stratification), and complex flow patterns by wind and waves. These models are adequately suitable for predicting suspended turbulent sediment load in the reservoir since the suspended turbulent sediment transport is a three-dimensional phenomenon. However, the sediment transport and hydrodynamics are not coupled in most 3D numerical models. Some of 3D models are reviewed below.

2.6.4.1 SSIIM Model

SSIIM (Sediment Simulation in Intakes with Multiblock Option) is a 3D sediment transport model for use in rivers, channels and estuaries developed by Olsen (1994). It solves the Navier-Stokes equations using the control volume method with the SIMPLE algorithm and the $k-\varepsilon$ turbulence model. It also solves the convection-diffusion equation for suspended sediment transport.

2.6.4.2 FLUENT Model

FLUENT is a product of ANSYS fluid analysis software and provides fast, accurate and robust Computational Fluid Dynamics (CFD) solutions. FLUENT is a computer program which can model fluid flow and heat transfer in complex geometries using the finite volume method. It is able to simulate laminar and turbulent flows in 3D geometries. One of the special features of FLUENT is the User-Defined Function (UDF) which allows the user to customise for example, material properties and boundary conditions in the FLUENT program.

2.6.4.3 Fang and Wang Model

The numerical model developed by Fang and Wang (2000) is a 3D sediment transport model that uses equations for sediment-laden water with variable density. Therefore, the model can take account of stratified flows and was applied to predict reservoir sedimentation in the Three Gorges Reservoir project in China (Campos, 2001).

2.6.4.4 MIKE3

MIKE3 is a 3D model with an orthogonal grid system developed by the Danish Hydraulic Institute (DHI) for free surface flows. It includes modelling components for advection-diffusion, water quality, flooding and drying of intertidal areas, and sediment processes (Jacobsen and Rasmussen, 1997). The model can simulate interactions between the bed sediments and the water column, sediment transport, deposition and entrainment.

2.6.4.5 DELFT3D

DELFT3D model is a 3D integrated modelling system developed by the Delft Hydraulic Laboratory team that is solved through the finite difference scheme (Delft, 1999). The model contains several submodels that simulate the temporal and spatial variation of six processes namely; flow, waves, water quality, morphology, sediment transport, and ecology. DELFT3D model can simulate flow and sediment transport processes and water quality.

2.6.5 Summary

In this section, an overview of numerical modelling of suspended sediment transport was given by reviewing some existing numerical models that deal with sediment transport and hydrodynamic simulation. They are grouped into three categories namely, 1D numerical models, 2D numerical models and 3D numerical models. Although 3D mathematical model is the more convenient model because of its wide range of applicability, it remains the most complex model. The sediment transport and hydrodynamics are not coupled in most 3D numerical models. A coupled numerical model in terms of sediment transport and flow field is very convenient in case of shallow water, river system or local scour process where bed level change considerably affects the flow fields. In this regard, the scope of the present study was to develop a fully coupled 3D numerical model able to simulate reservoir sedimentation processes and will be discussed in the following chapters.

3. Experimental Investigations of Bottom Outlet Flushing under Pressure

3.1 Introduction

The prediction of the local scour process occurring upstream of the reservoir flushing bottom outlet under pressure is challenging and it was the primary objective of the present study. One of the commonly used methods to investigate the extent and depth of local scour is to carry out physical model tests. Laboratory tests were conducted in the present research work, in order to assess the local scouring development upstream of the bottom outlet during a flushing event. The main objective of this experimental investigation was to collect data from measurements in a controlled environment. Subsequently, these data would later be used for the validation of the coupled fully three-dimensional numerical model of the bottom outlet flushing presented in Chapter 5. The physical model emulating reservoir conditions was set up in a laboratory rectangular flume in which a packed bed made of sediment with uniform size was built. Water was then released through the bottom outlet until local scour becomes apparent upstream of the bottom outlet. More details on the experimental setup as well as the physical test procedure and results are given and discussed in the following sections.

3.2 Physical Model Setup

The experimental investigation presented in this research was conducted in the hydraulic laboratory of the Civil Engineering Department of Stellenbosch University. The physical model consisted of an elevated rectangular flume of 40 m long, 1.24 m deep and a width of 1 m (see Figure 3.1). The flume was equipped with a permeable woven sheet located at its upstream side, near the pump supply system which creates a smooth inflow and reduces the turbulence caused by pump fluctuations. In addition, the flume was long enough to ensure a fully developed uniform flow with less turbulence and vortices reaching the packed bed which was located far downstream of the flume.

A wall made of PVC with 1 m high, representing the dam was mounted at the downstream end of the model with a bottom circular orifice 0.09 m in diameter and located at the centre of the wall, 0.26 m above the floor of the flume. The orifice was connected directly to the outlet pipe equipped

with a flowmeter and a manual valve. In this experimental study, an Endress + Hauser Promag 50W electromagnetic flowmeter was utilised for the measurements of the flow exiting the bottom outlet. Located just downstream of the flowmeter, the manual valve was used to adjust the flow rate according to the necessary flow needed for the model test. The outlet flow rate was increased by pumping more water out of the flume through the outlet pipe using a pump, which was located further downstream. This additional setup allowed the testing of relatively high discharges, exceeding the discharge due to gravity ($0.021 \text{ m}^3/\text{s}$). The maximum pumped discharge reached in the present study was $0.036 \text{ m}^3/\text{s}$. Figures 3.1 to 3.4 show the laboratory flume setup with its different features.

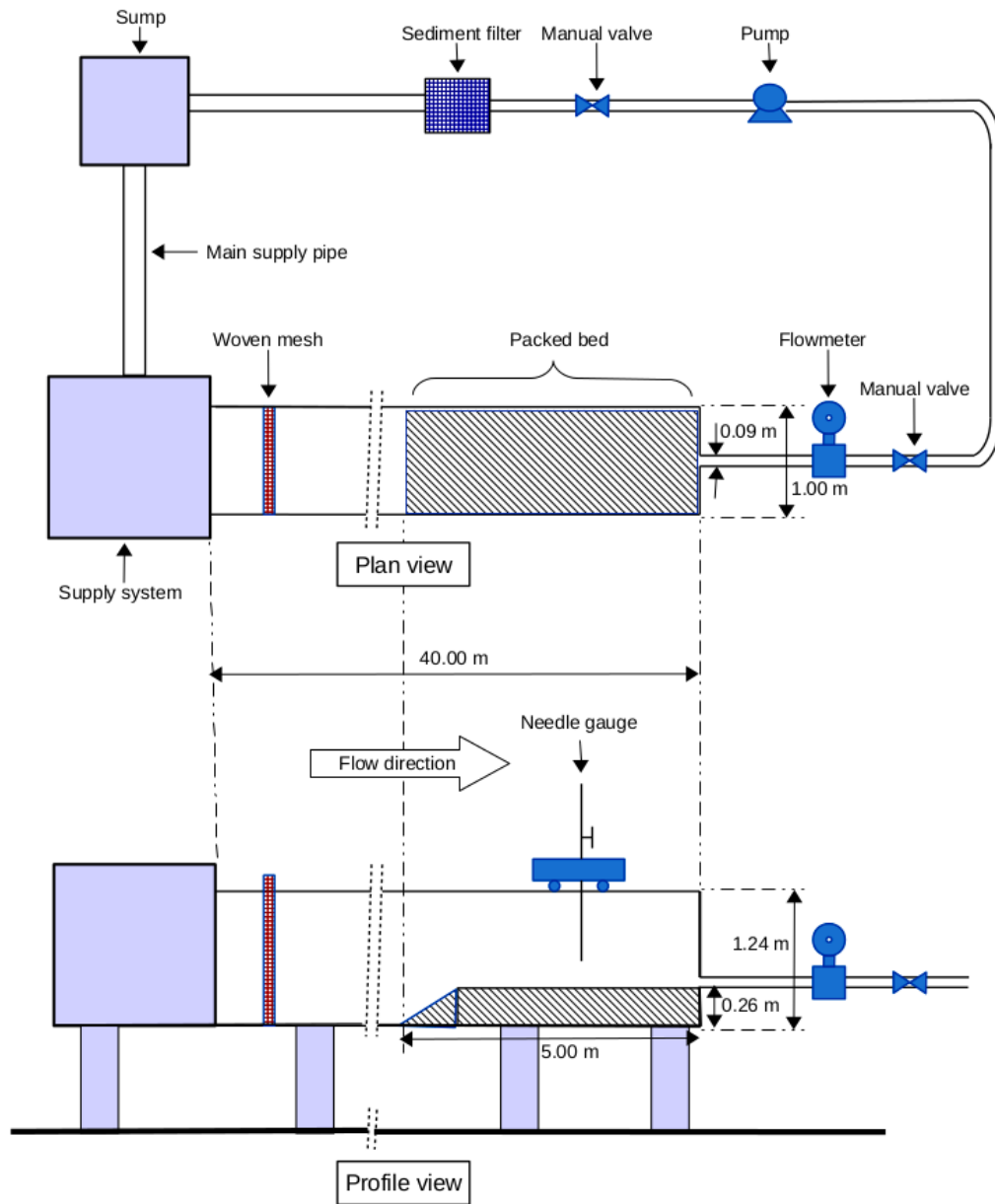


Figure 3.1: Experimental flume layout

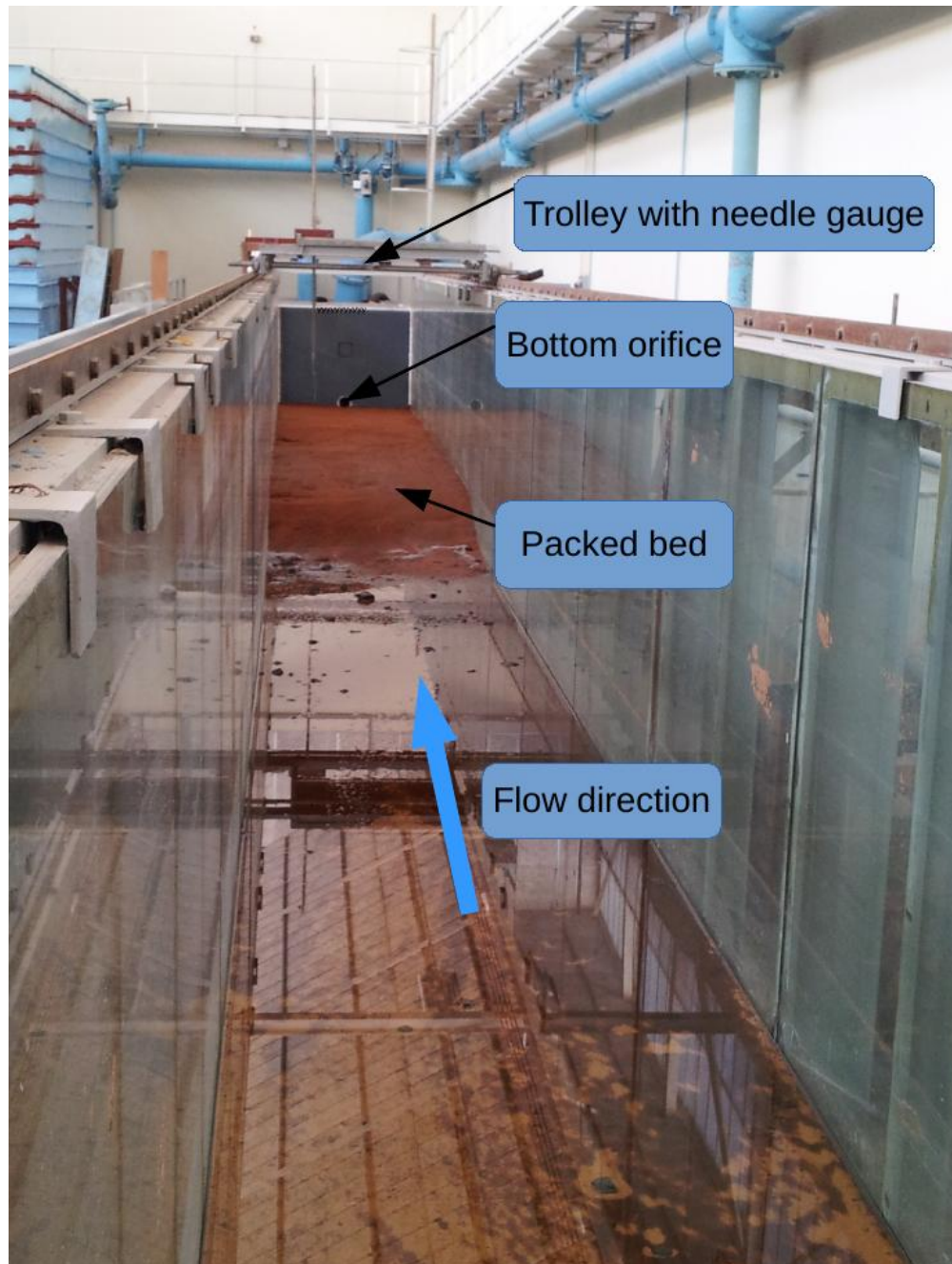


Figure 3.2: Laboratory flume view from upstream



Figure 3.3: Packed bed levelled with the outlet invert



(a) Needle gauge used for scour hole survey



(b) Flowmeter used for flow measurement

Figure 3.4: Measurement instruments

The erodible part of the physical model was made of a packed bed with a total length of 5 m and a height of 0.26 m relative to the flume floor, which corresponds to the bottom outlet invert (see Figure 3.3). In this experiment, the sediment was modelled using crushed peach pips. A standard sieve grading analysis on the same sediment, done by Stephan (2013) showed that the sediment has a d_{50} diameter of 0.74 mm as indicated in Figure 3.5.

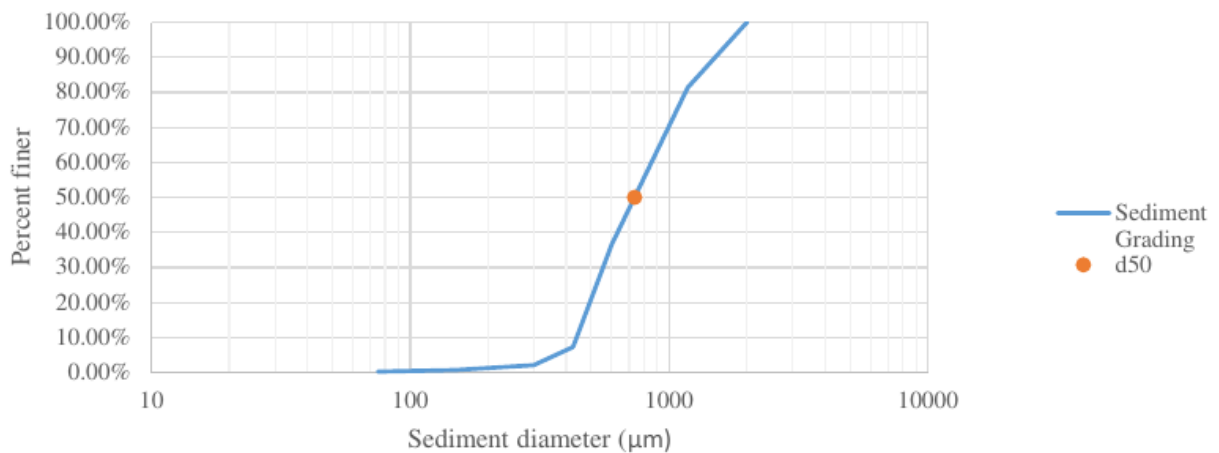


Figure 3.5: Sediment size distribution curve (Stephan, 2013)

Furthermore, a value of 1.65 was found for Gr known as the gradation coefficient. This value indicates a relative high uniform sediment size distribution and this is also depicted in Figure 3.5 showing the sediment cumulative frequency distribution curve with a steep section between 0.43 mm and 1.18 mm . An average settling velocity of 0.023 m/s was found after conducting a settling velocity test on a sample of 54 sediment particles and the specific gravity of 1.35 was measured following the same procedure. All the above mentioned values of crushed peach pips properties were taken from the sieve analysis done by Stephan (2013).

Scour depth measurements were accomplished by utilising a moveable trolley equipped with needle gauge which is able to roll along steel rails mounted on top of both side of the flume's walls (see figure 3.4). Measurements of erosion upstream of the bottom outlet were done by surveying the extent and depth of the scour in a grid fashion. The extent and the depth of the local scour was therefore surveyed every 0.10 m across the width of the flume and at 0.10 m longitudinal intervals along the erodible area of the model. These readings were relative to the bottom outlet position and provided a three-dimensional grid data of the local scoured region useful to produce a map for visual analysis.

3.3 Laboratory Test Procedure

Prior to the beginning of the physical model test, the surface of the packed bed inside the flume was uniformly levelled to an elevation equal to the bottom outlet invert. Unlike some laboratory tests conducted in previous research works (see Section 2.4.2) in which the packed bed height was placed above the invert bottom outlet, only sediment level to the bottom outlet invert was considered in the present study. The same condition was also adopted by Powell (2007) for the study of sediment transport upstream of orifices and therefore one of his laboratory test is simulated and presented in Chapter 5. The flume was filled with water at low flow rates (less than $0.002\text{ m}^3/\text{s}$) in order to avoid any disturbances to the surface of the packed bed before the starting of the actual test. The valve preventing water to flow out of the flume was gently opened after the water height was above the bottom outlet invert. This allowed the water to flow through the pipe system connected to the pump and ensures the removal of any air trapped inside the pipe system. As a result, the pump was operating under its full capacity. After the above mentioned preliminary steps, the flume was gradually filled with water until it spilled over the wall. As soon as the flow was steady inside the flume, the water level was kept constant during the tests. Thus, the actual test began with the activation of the pump at the outlet and in the meantime the valve in conjunction with the flowmeter, was manually adjusted in order to obtain the preferred outflow rate for the test. The time from the beginning to the end of the erosion process at specific flow rates was recorded as well as the water level which remained constant during the model test. Once the scour process reached its equilibrium point, that is when the scour depth reached its maximum size and there was no more significant change in terms of scour hole depth and extent, the test was ended by stopping the pump and closing the bottom outlet. It is worth noting that the equilibrium condition of the scour hole is difficult to determine and it has been defined differently in previous studies. This could be due to differences in the experimental setup conditions and most importantly the type of the measurement device used for the survey of the bed level change during the test. For example, Powell (2007) defined the equilibrium condition in his experiment by only assessing the centreline bed profile change during the scour process.

After the erosion reached its equilibrium point, the water was drained from the flume through a bottom outlet located further upstream at the back of the flume. This was done at a slow flow rate and far from the scoured area in order not to alter the final scour pattern before any measurements were taken. Finally, the scour depth and its extent were manually surveyed after the water was totally drained from the scour area, upstream of the bottom outlet.

In this experimental study, only three different flows were tested namely; $0.036 \text{ m}^3/\text{s}$ (Test 1), $0.021 \text{ m}^3/\text{s}$ (Test 2) and $0.012 \text{ m}^3/\text{s}$ (Test 3). These values were chosen based on the limitation of the laboratory setup. As mentioned before, the maximum discharge reached when water flows by gravity, was $0.021 \text{ m}^3/\text{s}$ and this value was increased to $0.036 \text{ m}^3/\text{s}$ using a pump further downstream. The flows used during Tests 1 to 3 correspond to flow velocities in the outlet pipe of 5.66 m/s , 3.30 m/s and 1.89 m/s respectively. All tests were run following the above mentioned procedure and "clear water" (no sediment input) were maintained during the laboratory flume tests.

3.4 Physical Model Test Results

3.4.1 Visual Observations of the Scour Process

During the laboratory test, special attention was given to the area with high potential to scour. This area is known as the critical shear zone and was closely monitored by visual observation in order to assess the scour development upstream of the bottom outlet. From a direct visualisation, it was observed that the primary stage of sediment motion occurred closer to the outlet and this was due to the bottom shear stress of the flowing water. At that specific point, the shear stress exerted by the water onto the bed surface exceeded the critical shear stress of the sediment causing its entrainment by the flow. The sediment was first lifted from the bed and put in suspension motion and then sucked through the bottom orifice following the streamlines. Furthermore, a scour hole was developed at the critical shear zone which contributed to modifying the velocity field upstream of the bottom outlet. It is plausible to mention that as the scour depth increases the velocities inside the scour hole will decrease. Consequently, this will reduce the shear stress forces in the area and eventually may fall below the critical shear stress value. As the bed was eroded, the slope inside the scour hole increased and became unstable, resulting in slope failure. The unstable sediment layer collapsed by moving down along the slopes until it reached the critical shear stress area. The sliding motion of sediment inside the primary scoured hole is described in this study as the secondary scouring mechanism. The secondary scouring process was carried out until the slope inside the scour hole reached the angle of repose, which is defined as the angle for which the slope is stable. A transitional zone was observed between the primary scour and the secondary scour zones. Figure 3.6 depicts the final scoured hole at the bottom outlet in which different scouring mechanism zones are represented.

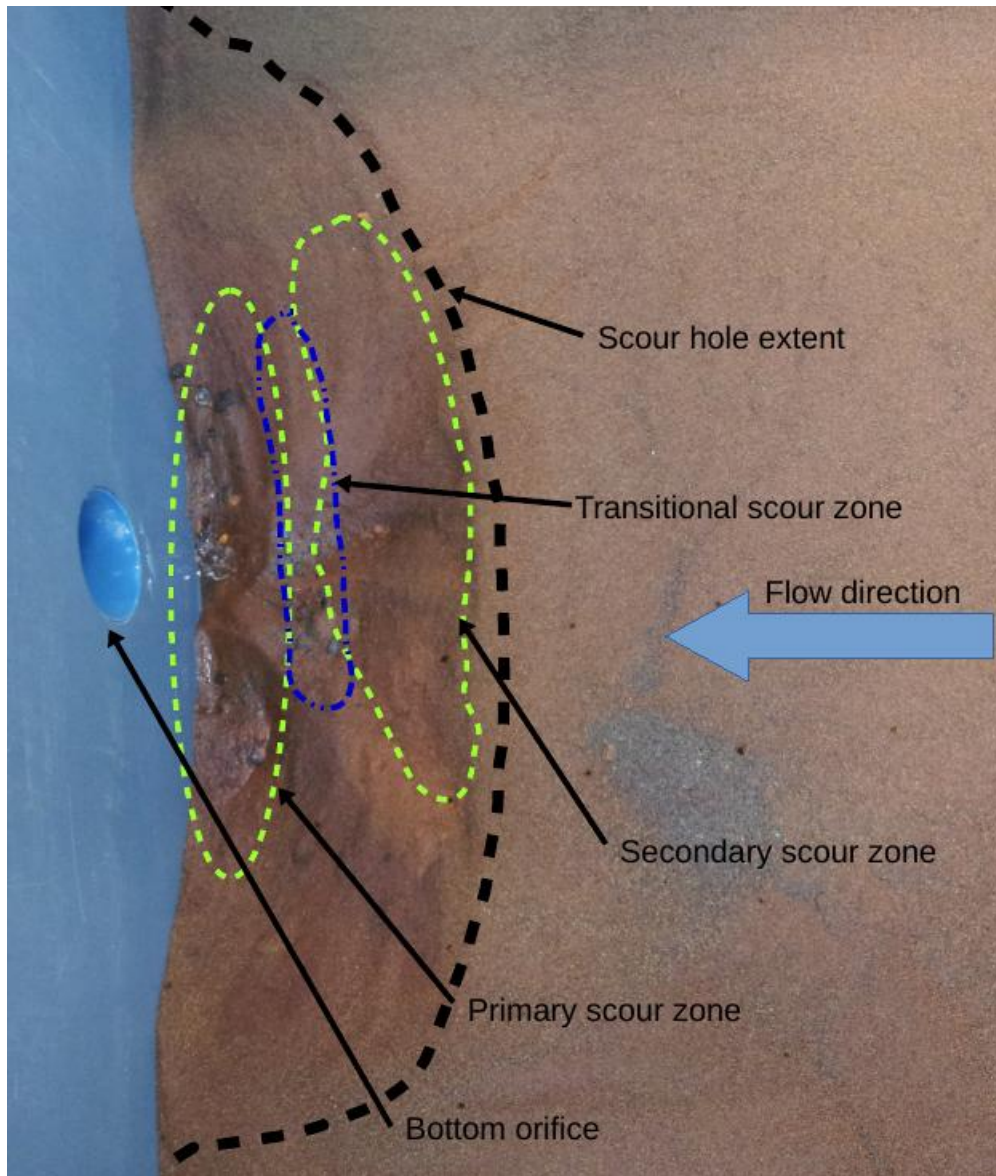


Figure 3.6: Scour hole extent and scouring process based on visual observations

Due to the complex flow-sediment interrelationship with the turbulent three-dimensional flow conditions that occurred during the scour process, it is difficult to define the actual location of the transitional zone. Finally, the edge of the scour hole was a semi-ellipsoid shape when the equilibrium condition was reached. The extent of the scour hole in Figure 3.6 clearly illustrates the elliptical shape of the final edge of the scour hole. Furthermore, it is shown that near the bottom outlet the slopes are relatively unstable due to the presence of a ridge in the scour hole while they become stable further away from the outlet. Results from the laboratory tests, which are discussed in the next section showed that the shape of the scoured hole shifted from ellipse to a shape similar to a circle as the flow rate at the bottom outlet increases. Powell (2007) reached the same conclusion in a similar study by increasing water level above the bottom outlet.

3.4.2 Test Results of Scour Depth and Extent

As mentioned in Section 3.3, three experimental tests were run by varying the bottom outlet flow rate. Each test was run twice to ensure that there is no major differences between results from experimental tests conducted in the same flow conditions. Table 3.1 shows a summary of the different test results in terms of scour depth, width and length as well as the length-width ratio.

Table 3.1: Experimental results

	Discharge $Q(m^3/s)$	Scour depth $D_{scour}(m)$	Scour width $W_{scour}(m)$	Scour length $L_{scour}(m)$	Ratio $L/(W/2)$
Test 1	0.036	0.12	0.65	0.33	1.02
Test 2	0.021	0.10	0.56	0.29	1.04
Test 3	0.012	0.08	0.46	0.20	0.87

It can be seen from Table 3.1, that the scour depth, width and length increase with increasing flow rate which was in this experimental study the only varying parameter. Furthermore, the length-width ratio tends to a value closer to 1 as the discharge at the bottom outlet increases. This value implies that the outline of the scour hole tends relatively to a circular shape as mentioned before. In order to render the three-dimensional view of the bed topography upstream of the bottom outlet, data gathered from the depth measurements of the scour hole were plotted using SURFER, which is a 3D surface mapping software. The following figures show the final scour hole and 3D final bed topography for Test 1. The same figures for Test 2 and Test 3 are shown in Appendix A.



Figure 3.7: Scour hole for Test 1

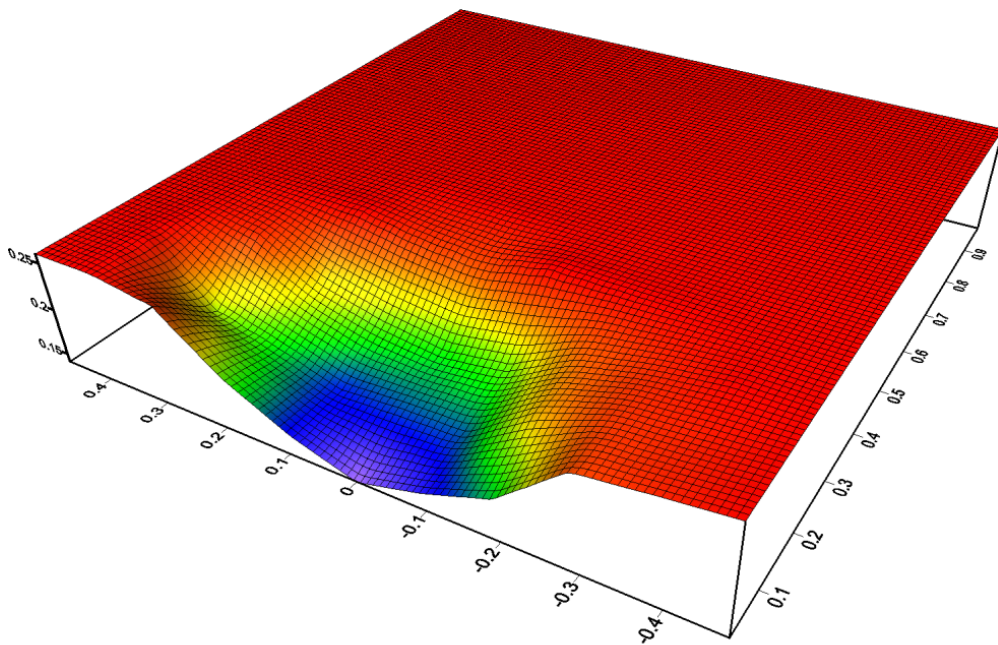


Figure 3.8: 3D bed surface mapping for Test 1

3.4.3 Test Results of Scour Bed Profiles

In this section more detailed representation of the experimental results is made. Both lateral and longitudinal bed profile for different tests are plotted in a Cartesian coordinate system using the flume floor and the centre of the bottom orifice as the vertical and horizontal datum respectively. Figure 3.9 shows the coordinate system adopted in this experimental study and final bed profiles from experiments were given in both lateral and longitudinal directions.

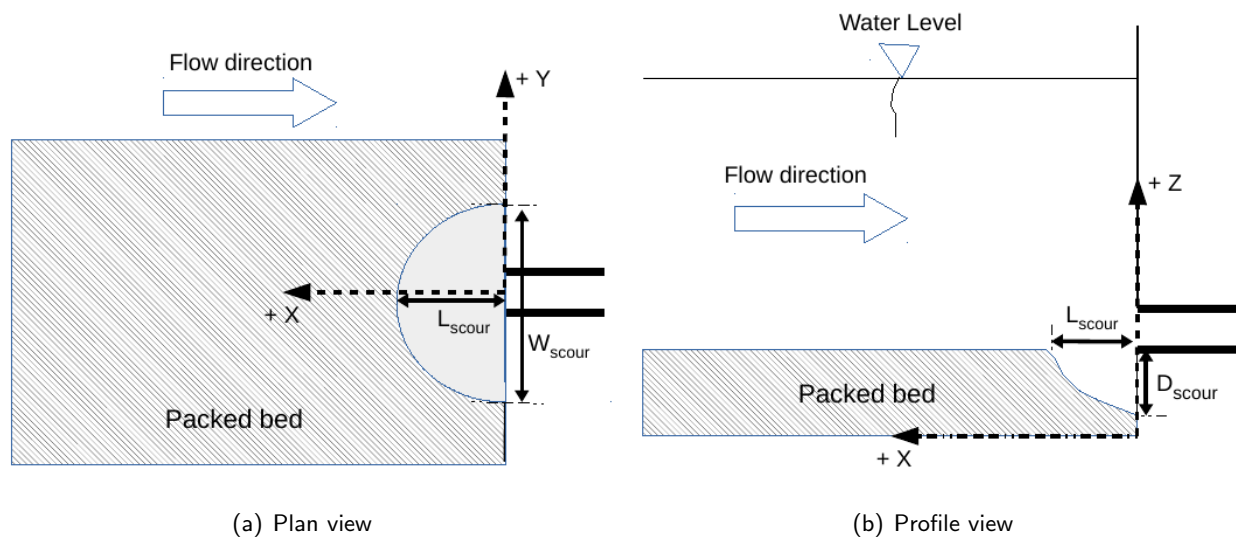


Figure 3.9: Cartesian coordinate system

- **Lateral profiles**

In order to describe the transversal changes of the scour hole from the different tested flow rates, the lateral bed profiles are plotted along y -axis upstream of the bottom outlet every 0.05 m away from the orifice as depicted in Figure 3.10. In this figure the abscissa shows the lateral distance (Y) and the ordinate depicts the bed surface elevation relative to the flume floor (Z).

The first observation is that the lateral slopes are more steeper for cross sections that are close to the bottom orifice, and this shows that the deepest scour hole is near the bottom outlet ($x = 0$). Secondly, the bottom of the scour hole at that particular location is sharp whereas lateral cross sections away from the bottom orifice have a relatively flat bottom end. Similar lateral cross section pattern was found for Test 2 and Test 3 (See Appendix A).

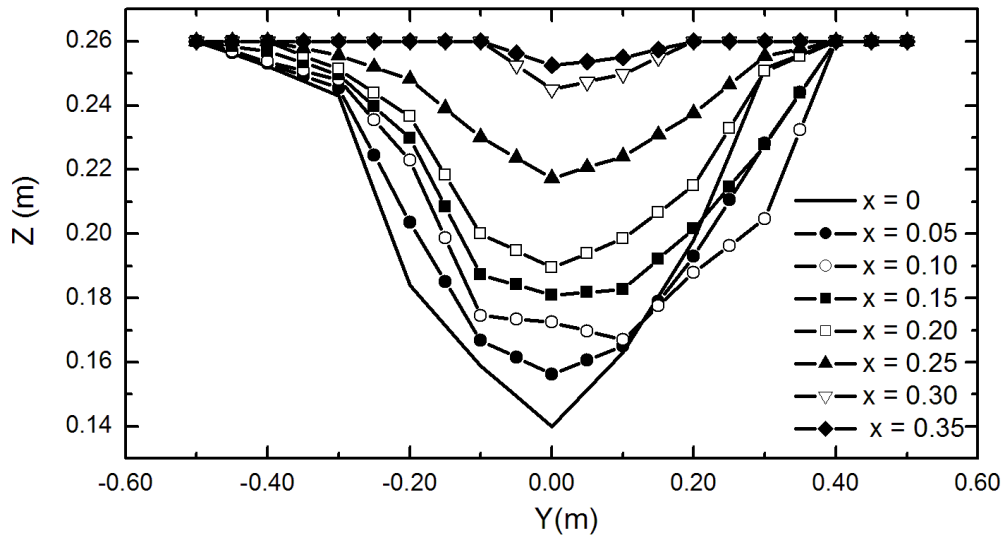


Figure 3.10: Observed lateral cross sections of the scour hole for Test 1

- **longitudinal profiles**

The longitudinal bed profiles are plotted along the x -axis upstream of the bottom outlet every 0.10 m on both sides of the centreline which is a horizontal line passing through the centre of the bottom orifice. These longitudinal profiles help to describe how the scoured hole varies in the flow direction. Figure 3.11 shows the longitudinal bed profiles for Test 1 in various locations y . In this figure the abscissa represents the longitudinal distance (x) and the ordinate depicts the bed surface elevation relative to the flume floor (Z).

The results show that the centreline profile ($y = 0$) has a uniform steep slope while in the other longitudinal bed profiles, the upper part presents a relatively steep slope and the lower part is more or less flat. These results confirm that the deepest scour hole is located closer to the bottom outlet.

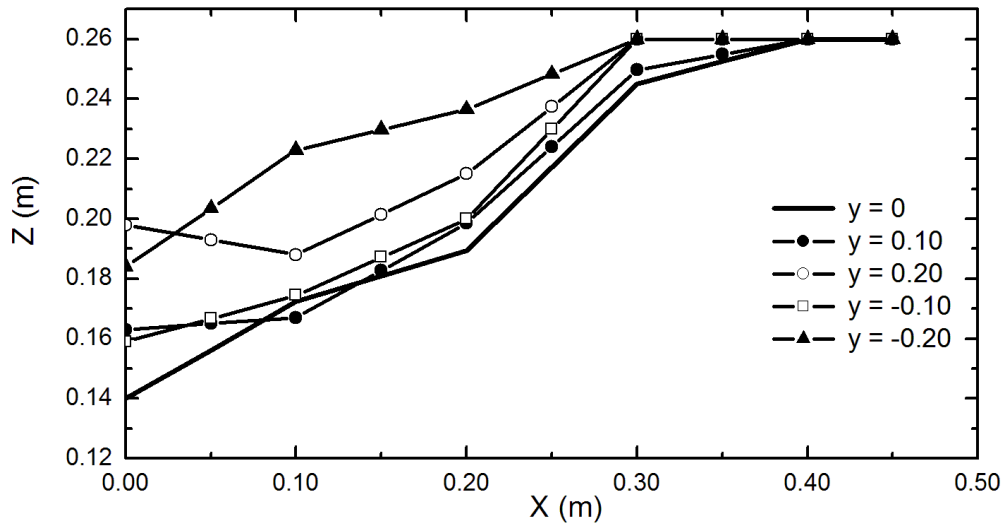


Figure 3.11: Observed longitudinal cross sections of the scour hole for Test 1

- **Scour hole profile variation with flow rate**

In order to describe the bed profile changes due to flow variation, the lateral cross section located at the bottom outlet ($x = 0$) and the centreline profile ($y = 0$) of the scour hole are plotted for different discharges in the same graph.

Figure 3.12 shows the lateral bed profile at the deepest scour hole location for various flow rates run in this experimental study.

It can be seen that the scour width becomes wider and the scour depth deeper as the discharge increases. However, the shape of the lateral cross sections at the deepest scoured hole are similar regardless of the flow rate.

Figure 3.13 describes the centreline bed profile for various flow rates tested in this physical model study. It can be seen that the scour length and depth increase as the discharge increases. The results show that the slope of centreline profiles are similar regardless of the discharge.

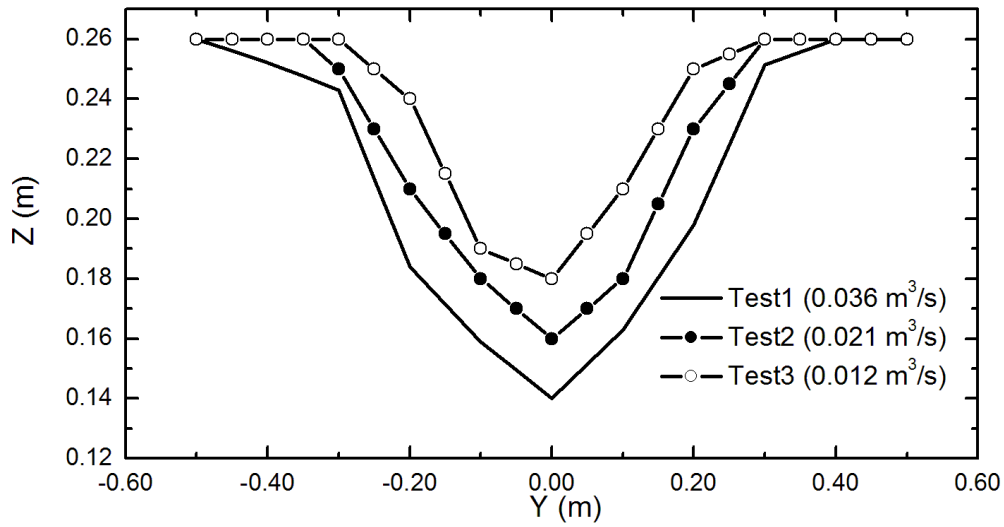


Figure 3.12: Lateral cross section variation with flow rate

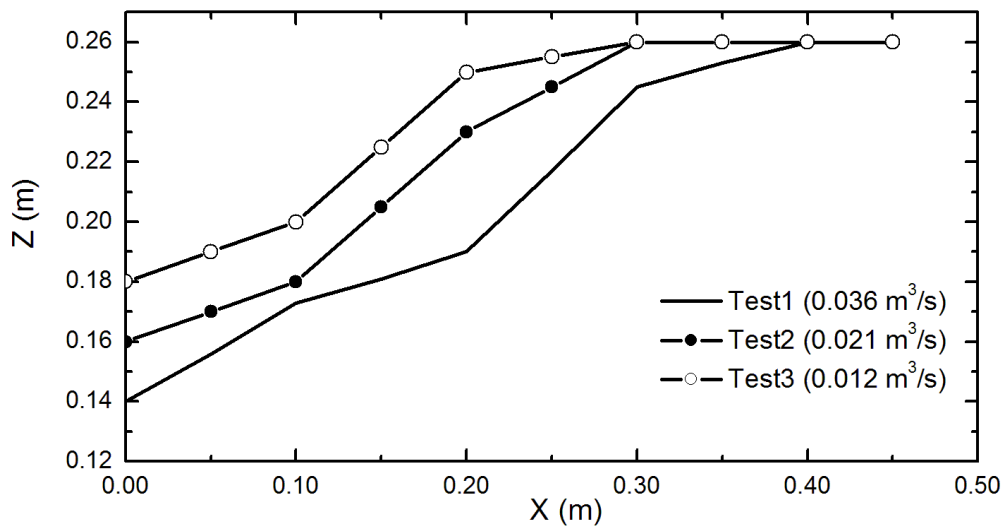


Figure 3.13: Longitudinal cross section variation with flow rate

The shape of the scour hole is highly dependent on the bottom outlet discharge as shown in Figures 3.12 and 3.13.

3.4.4 Experimental Test Limitations

The experimental work presented in this study consisted of simulating the bottom outlet flushing operation and the main focus was on the area upstream of the bottom outlet which has a high potential of erosion. The experimental tests were run for different flows. However, only a few flow rates were tested due to the experimental setup limitations. The water level above the bottom outlet and the suction head of the pump directly connected to the outlet pipe constituted the limiting factors in the experimental setup. Furthermore, besides the flow rate and water level which remains constant for all tests, velocity components upstream of the orifice were not measured due to lack of an appropriate velocity measurement instrument. To overcome the lack of velocity field information, velocity component data from similar experimental study found in the literature were used as additional data for the present experimental work.

3.5 Summary

Laboratory tests were conducted in the present study to investigate the scour process upstream of the bottom outlet. The physical model was set up in a rectangular flume in which sediment from crushed peach pips was packed with the bed surface levelled with the invert of the bottom outlet. Three different flow rates were tested namely, $0.036 \text{ m}^3/\text{s}$, $0.021 \text{ m}^3/\text{s}$ and $0.012 \text{ m}^3/\text{s}$. The visual observation of the experiment during different tests led to the spatial classification of the scour processes upstream of bottom outlet into three separate scour areas. The primary scour area is known to be driven by the bed shear stress while the secondary scour zone is due to slope instability which allows the unstable bed layer to slide down and therefore causes erosion. The transitional scour area separates the primary scour area from the secondary scour zone. However, the exact location of the transitional scour area can not easily be determined by visual observation due to the complexity of the flow field upstream of the bottom outlet.

Cross sections in both vertical and longitudinal variations of the scour hole were surveyed. The scour depth for each test was measured. The analysis of the experimental test results showed that the shape of the scour hole was directly dependent on the discharge at the bottom outlet. The scour depth, the scour width as well as its length increase as the flow rate increases.

4. Three-Dimensional Numerical Bottom Outlet Flushing Model Development

4.1 Introduction

In this study, a coupled fully three-dimensional (3D) numerical model was developed to simulate the scour pattern that occurred upstream of the bottom outlet during a flushing event. In this numerical model, the hydrodynamics are coupled with a sediment transport model. Both flow and sediment transport parameters are linked by the governing equations, which are presented in detail in the following sections.

The theory behind the proposed numerical model is discussed, which is divided into two parts. The first part gives an insight into the basics of fluid dynamics through the well known Navier-Stokes equations and the theory used to model the turbulence phenomena. In the second part, the sediment transport model is discussed, focusing on the interaction flow-particle.

4.2 Computational Fluid Dynamics Modelling

4.2.1 Governing Equations

The general conservation equations used in the present study to model the flow field are presented in this section.

Unlike the two-dimensional (2D) single phase flow equations, where many assumptions have to be made, the 3D numerical model presented in this study follows an Eulerian multiphase approach. Thus, the continuity equation for phase q in the model is given as

$$\frac{\partial \alpha_q}{\partial t} + \nabla \cdot (\alpha_q \mathbf{V}_q) = \frac{1}{\rho_q} \left(\sum_{p=1}^n (m_{pq} - m_{qp}) + S_q \right) \quad (4.1)$$

where α_q denotes the volume fraction, \mathbf{V}_q is the velocity of phase q , ρ_q is the density of phase q , m_{pq} is defined as the mass transfer from the phase p to phase q and m_{qp} the mass transfer from the phase q to phase p and S_q is the mass source term of phase q . Note that constant density (ρ_q) is assumed and also the mass transfer between phases is neglected in this study and therefore, $m_{pq} = -m_{qp} = 0$.

The momentum equation for phase q reads as

$$\frac{\partial \alpha_q \mathbf{V}_q}{\partial t} + \nabla \cdot (\alpha_q \mathbf{V}_q \mathbf{V}_q) = \frac{1}{\rho_q} \left(-\alpha_q \nabla p + \nabla \cdot \bar{\mathbf{T}}_q + \alpha_q \rho_q \mathbf{g} + \sum_{p \in \mathcal{F}} R_{pq} (\mathbf{V}_p - \mathbf{V}_q) + \mathbf{F}_q \right) \quad (4.2)$$

where $\bar{\mathbf{T}}_q$ is the stress-strain tensor of phase q and given by

$$\bar{\mathbf{T}}_q = \alpha_q \mu_q \left(\nabla \mathbf{V}_q + \nabla \mathbf{V}_q^T - \frac{2}{3} \nabla \cdot \mathbf{V}_q \bar{\mathbf{I}} \right) \quad (4.3)$$

Here p is the pressure shared by all phases, \mathbf{g} is the gravitational acceleration, R_{pq} is the interface momentum exchange term, \mathbf{F}_q is an additional volumetric forces of phase q , μ_q is the shear viscosity of phase q and $\bar{\mathbf{I}}$ denotes the unity tensor.

In this model, three phases are considered, namely; water (α_w), rolling particles (α_r) and saltating grains (α_s) that is, $p, q \in \mathcal{F} = \{w, sal, rol\}$. Section 4.3 describes detailed classification of these particles into saltating and rolling particles respectively. Also discussed in detailed is the mass source term (S_q) which accounts for sediment deposition and erosion are discussed. Equation 4.3 is only valid for Newtonian fluid as it is the case in this study. According to Anderson and Haff (1991), the solids volume fractions are expected to be very small (less than a value of order of magnitude around 10^{-3}). Thus, it assumed that $\mu_q \approx \mu_w$ where μ_w is shear viscosity of water. In order to close Equation 4.2 with appropriate expressions for the interphase momentum exchange coefficient which depends on the friction, pressure, cohesion, and other effects (Fluent, 2011), the interaction fluid-solid momentum exchange term is computed following Wen and Yu model (Fluent, 2011).

$$R_{pq} = \frac{3}{4} C_D \frac{\alpha_p \alpha_q \rho_q |\mathbf{V}_p - \mathbf{V}_q|}{d_p} \alpha_q^{-2.65} \quad (4.4)$$

where

$$C_D = \frac{24}{\alpha_q Re_p} \left[1 + 0.15 (\alpha_q Re_p)^{0.687} \right] \quad (4.5)$$

and d_p denotes the diameter of the particulate phase p . The relative Reynolds number is computed from

$$Re_p = \frac{\rho_q d_p |\mathbf{V}_p - \mathbf{V}_q|}{\mu_q} \quad (4.6)$$

4.2.2 Turbulence Model

In this research study the turbulence was modelled using the standard k - ε turbulent model. This turbulence model was first developed by Launder and Spalding (1974) and later it has been widely used

in industry due to its robustness and reasonable accuracy for a wide range of turbulent flow (Fluent, 2011). The standard k - ε turbulent model is defined as eddy viscosity model and Reynolds stresses are computed through the Boussinesq hypothesis. The k - ε model is a two-equation model, namely it is based on model transport for the turbulence kinetic energy (k) and its dissipation rate (ε). The transport equations for the turbulent kinetic energy k and the turbulent dissipation rate ε are obtained from

$$\frac{\partial \rho k}{\partial t} + \nabla \cdot (\rho k \mathbf{V}) = \nabla \cdot \left(\frac{\mu_t}{\sigma_k} \nabla k \right) + G_k - \rho \varepsilon + S_k \quad (4.7)$$

and

$$\frac{\partial \rho \varepsilon}{\partial t} + \nabla \cdot (\rho \varepsilon \mathbf{V}) = \nabla \cdot \left(\frac{\mu_t}{\sigma_k} \nabla \varepsilon \right) + \frac{\varepsilon}{k} (C_{1\varepsilon} G_k - C_{2\varepsilon} \rho \varepsilon) + S_\varepsilon \quad (4.8)$$

where G_k represents the production of turbulence kinetic energy (k) due to the mean velocity gradients and given as

$$G_k = -\overline{\rho u'_i u'_j} \frac{\partial u_j}{\partial x_i} \quad (4.9)$$

where $\overline{u'_i u'_j}$ is the Reynolds stresses and u_j is the component of local time-averaged flow velocities. By using Boussinesq concept, the turbulence production is simplified by

$$G_k = \mu_t \overline{\mathbf{T}_2} \quad (4.10)$$

where $\overline{\mathbf{T}_2}$ denotes the second invariant of the rate-of-strain tensor of the mixture, defined as

$$\overline{\mathbf{T}_2} \equiv \sqrt{2 \overline{S_{ij} S_{ij}}} \quad (4.11)$$

The turbulent or eddy viscosity μ_t in Equations 4.7, 4.8 and 4.10 is computed by linking k and ε as follows

$$\mu_t = \rho C_\mu \frac{k^2}{\varepsilon} \quad (4.12)$$

S_k and S_ε are additional user-defined source terms for the turbulent kinematic energy k and the turbulent dissipation rate ε equations, respectively. These source terms are described in detail in Section 4.3.2. In this present research the following default values for the model constants are used: $C_{1\varepsilon} = 1.44$, $C_{2\varepsilon} = 1.92$, $C_\mu = 0.09$, $\sigma_k = 1.00$, $\sigma_\varepsilon = 1.30$. These default values have been determined from comprehensive data fitting for a wide range of turbulent flows (Fluent, 2011) and they are found to be suitable for this study. The density ρ and the velocity \mathbf{V} of the mixture defined in Equations 4.7 and 4.8 are given as

$$\rho = \sum_{q \in \mathcal{F}} \alpha_q \rho_q \quad \text{and} \quad \mathbf{V} = \frac{1}{\rho} \sum_{q \in \mathcal{F}} \alpha_q \rho_q \mathbf{V}_q \quad (4.13)$$

4.3 Sediment Transport Modelling

Sediment erosion and deposition of a packed bed due to shear forces of a fluid is an important research topic in engineering practice. For example, the sediment deposition that occurs at the bottom outlet of a reservoir can seriously undermine the functioning of such a hydraulic structure if an adequate remedial solution such as flushing is not found. In this regard, numerical modelling of sediment transport can be used as tools in the management and design of existing bottom outlet as well as future reservoir outlet.

The prediction of sediment erosion and deposition is challenging and many researchers have developed empirical formulas in order to get a better understanding of fluid-particle relationship. Based on work done on particle transported by wind, Bagnold (1966) concluded that sand grains are put in motion if the shear stress exerted by the wind onto the soil exceeds a certain threshold, which is known as fluid threshold. A similar relationship called the Shield Parameter, was developed by Shields (1936) after investigating sediment motion in river bed and assuming that resistance to motion depends only on the form of the bed and the immersed weight of the particles. In order to improve previous findings on fluid-particle motion relationship, a great deal of work has been published pertaining to fluid threshold (Chepil, 1959; Schmidt, 1980).

The present section deals with the modelling of different particle transport modes. According to Bagnold (1966), the particle transport mechanism is divided into three transport modes, namely, surface creeping, saltation and suspension. Furthermore, landslide-like shear slides of a whole layer of grains could also be considered as a particle transport mode and therefore it is accounted for in this study. Subsequently, modelling of the changing topography of the packed bed is addressed in this section.

In order to model the local erosion and deposition, detailed behaviour of individual grains and the interstitial fluid was the main focus and only the flow of the fluid above the packed bed was considered since the fully resolved modelling approach is confined to very small geometries (Schneiderbauer and Prokop, 2011). Therefore, the wall shear forces of the fluid determine the amount of entrained grains and the surface of the packed bed is considered to be a rough wall. From this assumption, the behaviour of the particles in motion can be modelled following two different approaches; in the first approach, the particles are considered as a continuous phase (Ouriemi et al., 2009) while the second one consists in tracking particle trajectories (Shao and Li, 1999). The first approach was followed in the present study and therefore, the particulate phase was considered as continuum.

The deformation of packed bed surface due to erosion and deposition can be modelled by the following

two methods. The first approach is defined as an Immersed Boundary method, which essentially consists of tracking the packed bed's surface. Khadra et al. (2000) used this method by first assuming an artificial packed media throughout the computational domain and then adjusting the packed media's porosity in order to match the actual physical packed bed. The second approach is referred to Arbitrary Lagrangian Eulerian method in which the computational grid for the fluid flow modelling is directly linked to the changing topography of the packed bed. That is, the computational grid is deformed according to the change at the surface of the packed bed due to erosion and deposition processes. The Immersed Boundary method was used in the present research and therefore no more details are given on the Arbitrary Lagrangian Eulerian method. However, the reader is referred to Schneiderbauer and Pirker (2010) for a detailed description on the capability of both methods to model erosion and sedimentation of a packed bed.

It is worth noting that the flow equations for Eulerian multiphase model in conjunction with the turbulence model presented in previous sections were solved making use of the standard ANSYS FLUENT code. On the contrary, the models proposed in this section, namely, the erosion and deposition model as well as the modelling of the deformation of packed bed's surface through the Immersed Boundary method, were not implemented in the standard version of ANSYS FLUENT. Actually, these sub-models were introduced by making use of User Defined Functions (UDFs), a special feature of ANSYS FLUENT which allows the user to define his own functions or code in C programming language, as well as to specify customised model parameters. After writing the UDFs code, it is compiled and dynamically linked with ANSYS FLUENT solver.

The methodology follows in this study for the modelling of the erosion and deposition as well as the changing topography of the packed bed surface was used in previous studies. For example, Schneiderbauer and Prokop (2011) adopted the same approach to develop an atmospheric snow-transport model while Schneiderbauer and Pirker (2014) used a similar method to study the erosion and the sedimentation processes in a wind tunnel. It must be pointed out, however, that the above mentioned studies deal with aeolian particle transport that is, the transport of particles is initiated by air, while only the hydrodynamic non-cohesive particle transport mechanism (particle transported by water) was addressed in the present study.

4.3.1 Sediment Erosion and Deposition Model

The sediment erosion and deposition of non cohesive sediment are modelled by considering the following particle transport modes: particle rolling due to the hydrodynamic shearing, particle rebound after impact, particle entrainment due to shear stresses, particle erosion due to impacting particles, particle deposition and accumulation as well as landslide shearing are considered.

For a better understanding of terms used to describe the particle transport mode in this chapter, the following definition of the classification of the different modes taken from Gauer (1999) is used.

- **Surface creeping /rolling:** This mode describes the transport of particles which is not directly affected by wind forces but their motion is rather caused by particle impact.
- **Saltation and modified saltation:** In this mode of transport, particles follow ballistic trajectories determined by the time-averaged wind profile and are not influenced by turbulence of the wind. This type of saltation is called pure saltation. In case the particle trajectories are highly affected by turbulent fluctuations of the wind then, modified saltation is used to describe the motion.
- **Reptation:** In this mode particles splashed up on impact do not obtain enough energy from the wind to rebound or eject other particles.
- **Suspension:** Particles are lifted and transported far from the bed without contact with the surface bed.

4.3.1.1 Hydrodynamic Entrainment

The motion of particles from the packed bed due to hydrodynamic shear stress can be quantified following Anderson and Haff (1991) formula, in which the number of sand grains entrained per unit time and per unit area $N'_A(m^{-2}s^{-1})$ is given as

$$N'_A = C_\eta (\tau_s - \tau_t) \quad (4.14)$$

where C_η is an empirical coefficient, τ_s is the shear stress at the surface and τ_t is the fluid shear stress threshold for particle entrainment. Anderson and Haff (1991) used a value of $10^5 N^{-1}s^{-1}$ for C_η while from an experimental work done for $350 \mu m$ quartz particles, White and Schulz (1977) suggested that the value of C_η is around $5 \times 10^7 N^{-1}s^{-1}$, which is, in terms of orders of magnitude higher than the value

proposed by Anderson and Haff (1991). In order to get a better understanding about the magnitude of the coefficient C_η , Shao and Li (1999) proposed a modified version of Equation 4.14 in which, the friction velocity $u_s^* = \sqrt{\tau_s/\rho}$ is introduced and C_η is approximated by $1/(mu_{x_0})$, thus

$$N_A \approx \frac{\rho}{mu_{x_0}} (u_s^{*2} - u_t^{*2}) \quad (4.15)$$

where, ρ is the fluid density, $m = \rho_p V_p$ is the mass of particle, $V_p = \pi d_p^3/6$ is the volume of the particle, d_p is the diameter of the particle, $u_{x_0} = a_x u_s^*$ is the mean lift-off particle velocity in x direction, a_x is a constant. Equation 4.15 is, therefore, rewritten as

$$N_A = \frac{C'_\eta u_s^*}{d_p^3} \left(1 + \frac{u_t^{*2}}{u_s^{*2}} \right) \quad (4.16)$$

where $C'_\eta \approx 6/(s\pi a_x)$ is a dimensionless coefficient proposed by Shao and Li (1999). Its value is around 1.74×10^{-3} by assuming that $a_x = 0.5$, which is taken from White and Schulz (1977) and s the specific gravity of particle with respect to air (2200). Schneiderbauer and Pirker (2014) found that the coefficient C'_η is proportional to the inverse of the particle diameter d_p and therefore,

$$C'_\eta \approx 5.19 \times 10^{-7} d_p^{-1}. \quad (4.17)$$

Based on different values presented and due to the lack of a substantial experimental data for accurate estimation of the coefficient, it is expected that C'_η would vary considerably according to the case study. Therefore, in this research, C'_η is considered as a calibration parameter. However, the coefficient C'_η as described in Equations 4.14, 4.16, and 4.17 is referred to as aerodynamic transport of particle. Based on the approximation done by Shao and Li (1999) ($C'_\eta \approx 6/(s\pi a_x)$) and using the specific gravity of particle with respect to water (2.65), the value of C'_η in the case of hydrodynamic transport of sand grains, is around 1.44. This value gives an indication on the order of magnitude of C'_η when the particle entrainment is due to water flow. However, after an extensive numerical calibration with laboratory data, it was observed that a value of $C'_\eta = 0.35$ gives a better stability of the surface of the packed bed during the numerical simulation. A greater value than 0.35 tends to considerably disturb the topography of the packed bed. Thus, 0.35 was used as value of the coefficient C'_η in the present research.

The total number of particles entrained due to shear forces of water flow is considered as the sum of rolling particles and the saltating grains at the bed surface. According to Shao and Li (1999), the classification of the resulting transport mode as surface rolling or saltation highly depends on the initial

ejection velocity of the particle $u_{i,o}$, which is given as

$$u_{i,o} = C_v u_s^* \quad (4.18)$$

where, C_v is a dimensionless coefficient and u_s^* is a shear velocity at the surface of the packed bed. In Shao and Li (1999), C_v is around 0.5 and the same value was used in the present study.

Knowing the number of entrained particles N_A (Equation 4.16), the total mass per unit volume and unit time ($kg.m^{-3}.s^{-1}$) for the particles entrained into surface rolling (S_{rol}^e) and for particles entrained into saltation (S_{sal}^e) are obtained from

$$S_{rol}^e = p_r m_p \frac{A}{V} N_A = p_r \frac{\pi \rho_p d_p^3}{6} \frac{A}{V} N_A \quad (4.19)$$

and

$$S_{sal}^e = (1 - p_r) m_p \frac{A}{V} N_A = (1 - p_r) \frac{\pi \rho_p d_p^3}{6} \frac{A}{V} N_A \quad (4.20)$$

where ρ_p is the particle density, A is the area and V the volume of a grid cell adjacent to the packed bed and p_r defines the probability that a particle is entrained into the surface rolling transport mode. In this study, it was assumed that the initial velocity of the rolling particles was 0 and also for a shear velocity of magnitude less than 1, p_r was approximately 0.5 and decreases as shear stresses increase at the surface of the packed bed. The same approach was followed by Schneiderbauer and Pirker (2014) in order to establish a relationship between the friction velocity u_s^* and the probability p_r .

In order to determine the fluid threshold τ_t and subsequently the shear velocity u_t^* in Equation 4.16 two approaches were considered; the first method is proposed by Chepil (1959) in which the critical drag force F'_C required to entrain a spherical particle is

$$F'_C = \left[\frac{\pi d_p^3}{6} g (\rho_p - \rho) - F_L \right] \tan \beta \quad (4.21)$$

where β denotes the mean drag level and F_L is the lift force acting on a particle and from previous experiments, $F_L = 0.85 F'_C$ (Chepil, 1959). From Equation 4.21, the critical drag force F_C per unit cross-sectional horizontal area occupied by the particle is $F_C = F'_C / (\pi d_p^2 / 4)$. Then after simplification

$$F_C = \frac{2 (\rho_p - \rho) g d_p \tan \beta}{3 (1 + 0.85 \tan \beta)} \quad (4.22)$$

By including in Equation 4.22, η the ratio of mean drag and lift per unit area on the whole bed to mean drag and lift on the top grain entrained by the fluid and Γ the ratio of maximum to mean drag and lift

on the particle, the fluid threshold that initiates the particle entrainment is given as

$$\tau_t = \rho u_t^{*2} = \frac{2}{3} \frac{\eta (\rho_p - \rho) g d_p \tan \beta}{\Gamma (1 + 0.85 \tan \beta)} \quad (4.23)$$

The second method for the fluid threshold calculation was taken from Schmidt (1980), which was similar to Equation 4.23. In this method, two constants were included, namely, the slope angle θ with respect to the flow direction and φ the angle of repose. Thus,

$$\tau_t = \rho u_t^{*2} = \frac{2}{3} \frac{\eta (\rho_p - \rho) g d_p (\cos \theta - \sin \theta / \tan \varphi) \tan \beta}{\Gamma (1 + 0.85 \tan \beta)} \quad (4.24)$$

The fluid threshold τ_t was determined in this study, using the second method (Equation 4.24) because it accounts for more parameters compared to Equation 4.23. However, the values for η , Γ and β were taken from Chepil (1959) that is, 0.21, 2.5 and 24° respectively. The angle of repose φ was 45° in the present research and it was obtained from the calibration of the numerical model.

4.3.1.2 Entrainment due to Particle Ejection

In this study, ejection of grains due to particle impacts at the surface of the packed bed is considered since it contributes to the sediment transport process. The collision of saltating particles with velocity U_I impacting at angle α_I at the surface of packed bed may cause the ejection of other particles with velocity U_E at the angle α_E . In addition the impacting particles may rebound with velocity U_R at the angle α_R or be trapped at the surface. Figure 4.1 describes the above mentioned different trajectories followed by particles after a collision at the surface of the bed.

In order to study this mode of transport, several researches pertaining to the particle impacts on the surface bed have been conducted for years. In this regards, some studies focus only on numerical simulations (Werner and Haff, 1988; Anderson and Haff, 1991) while others make use of physical models (Rice et al., 1995; Schneiderbauer, 2012) to investigate the particle-bed impacts. These studies concluded that impacting particles have a similar behaviour. For example, there is a small variation on the probability of the impacting particles to rebound, the impact angle and rebound angle as well as the ratio of impact velocity to rebound velocity (Gauer, 1999).

According to Gauer and Issler (2004), the number of ejected grains per particle impact is linearly dependent on the impact speed. On the contrary, Shao and Li (1999) and Andreotti (2004) assumed

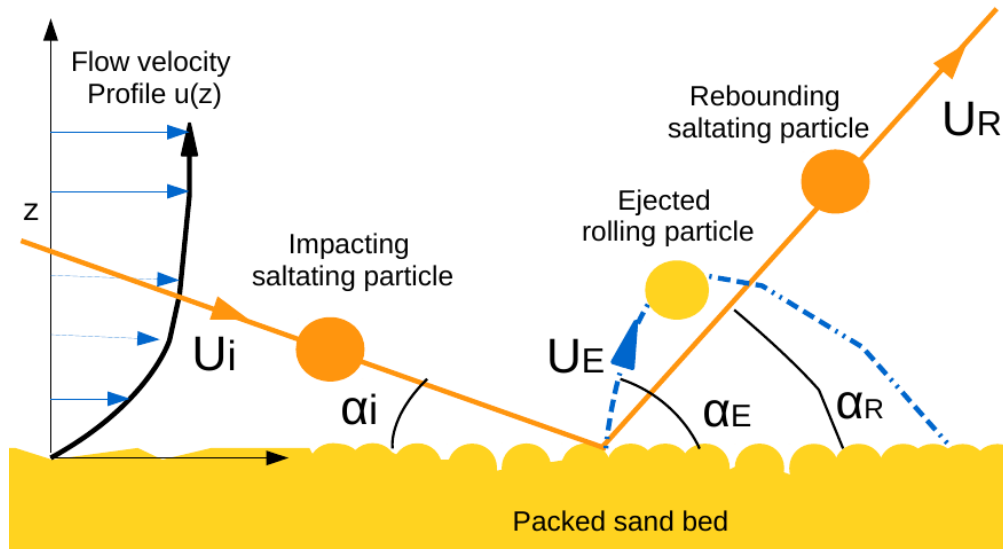


Figure 4.1: Sketch of particle impact at the surface of the packed bed

that the number of ejected particles depends mostly on the kinetic energy of impacting particles. The number of particles N'_{EpI} ejected by a single impact of a particle is (Shao and Li, 1999)

$$N'_{EpI} = \zeta_s \frac{m_{im}}{m_{sp}} \left(\frac{U_{Im}}{U_{t,sp}^*} \right)^2 \quad (4.25)$$

where m_{im} and m_{sp} are the impacting and splashed particle mass, respectively, ζ_s is the splash coefficient, U_{Im} is the velocity of the impacting particle and $U_{t,sp}^*$ is the threshold of the shear velocity. However, in the present research, the number of ejected particles per impact N_{EpI} , proposed by Andreotti (2004) was used and reads

$$N_{EpI} = 0.3 \left(\frac{U_{Im}}{c_i \sqrt{gd_p}} \right)^2 \quad (4.26)$$

where U_{Im} denotes the speed of impacting particle and c_i is a dimensionless coefficient and defines a velocity scale. In this work $c_i = 10$ was chosen and the same value was used by Anderson and Haff (1991), Andreotti (2004) and Schneiderbauer and Pirker (2014). Furthermore, based on the energy balance between impacting, rebounding and ejecting particles, Shao and Li (1999) proposed a theoretical limitation for the number of splashed (ejected) grains per impact as follows

$$N_{EpI}^{max} = \frac{c_s - 1.9c_a^2 \left[1 - e^{U_{Im}/(c_i \sqrt{gd_p})} \right]}{2c_h^2} \quad (4.27)$$

where c_s denotes the fraction of energy not converted to heat after the impact, whereas c_a and c_h are empirical coefficients. In the present study, the following values were used; $c_s = 0.5$, $c_a = 0.5$ and $c_h = 0.25$. Previous studies such as, Shao and Li (1999), and Schneiderbauer and Prokop (2011) used the same values for these coefficients. The total mass of splashed particles (S_{rol}^{ej}) per unit volume and unit time ($kg.m^{-3}.s^{-1}$), due to particle impact at the surface of packed bed, is determined by combining Equations 4.26 and 4.27 as follows (Schneiderbauer and Pirker, 2014)

$$S_{rol}^{ej} = \rho_p N_{im} \min(N_{Epl}, N_{Epl}^{max}) \quad (4.28)$$

and

$$N_{im} = \frac{\alpha_s}{t'_s} \quad (4.29)$$

where N_{im} is the number of impacts with the packed bed per unit time and t'_s is the mean travel time for a saltating particle, which is calculated from the initial velocity $u_{i,o}$ (see Equation 4.18) of the entrained particle as follows

$$t'_s = 2 \frac{u_{i,o}}{g} \quad (4.30)$$

Due to the relatively small kinetic energy generated by the splashed grains, Schneiderbauer and Pirker (2014) suggested that the total number of ejected particles S_{rol}^{ej} should be included into the rolling particulate phase. Furthermore, it was assumed that the energy from the rolling particle was not enough to eject other particles from the packed bed. Similar assumptions were made in this study.

The formula proposed by Andreotti et al. (2002) for the calculation of the initial velocity of splashed particles with an impacting angle of 45° , was followed in the present research and reads

$$u_{sp,o} = \zeta_r c_i \sqrt{gd_p} \quad (4.31)$$

In Equation 4.31, ζ_r is the restitution parameter of particle-bed collision, which is the velocity ratio of the rebounding particle to the impacting particle; 0.5 was taken as its value in this work like, in Shao and Li (1999), Gauer (1999), Andreotti (2004), and Schneiderbauer and Pirker (2014)

4.3.1.3 Particle Deposition

In the present research, it was considered that during the particle-bed collision some of the grains remain trapped at each rebound event. Therefore, a probabilistic approach was used to quantify the amount of trapped grains, which are initially a part of impacting grains on the surface of the packed bed. Based

on numerical simulation, Werner and Haff (1988) proposed the probability p_{re} of a particle rebound by

$$p_{re} = p_{re}^{max} \left[1 - e^{-U_{Im}/(c_i \sqrt{gd_p})} \right] \quad (4.32)$$

where p_{re}^{max} is defined as the rebound probability for a high velocity of the impacting particle, and according to Quartier et al. (2000) the term $c_i \sqrt{gd_p}$ represents a velocity threshold below which the probability p_{re} of rebound particles becomes relatively small. As a result, it is described as the velocity needed by the impacting grains to escape the potential trapping at the surface of the packed bed.

Given that the probability of an impacting particle to rebound is known (Equation 4.32), the probability of a grain to get trapped can be readily expressed as

$$p_{tr} = 1 - p_{re} = 1 - p_{re}^{max} \left[1 - e^{-U_{Im}/(c_i \sqrt{gd_p})} \right] \quad (4.33)$$

In the present study, p_{re}^{max} was estimated at 0.95, which was taken from Andreotti (2004). Knowing the number of impact N_{im} of a particle per unit time and the trapping probability p_{tr} of a grain at the surface of the bed, the total mass of deposition of saltating S_{sal}^{de} and rolling particles S_{rol}^{de} per unit volume and unit time ($kg.m^3.s^{-1}$) are calculated as

$$S_{sal}^{de} = \rho_p \frac{\alpha_s}{t'_s} p_{tr} \quad (4.34)$$

and

$$S_{rol}^{de} = \rho_p \frac{\alpha_r}{t'_r} p_{tr} \quad (4.35)$$

By assuming that the hop height of the rolling grains is in the same order of magnitude of the surface roughness k_s , which is approximated by the particle diameter d_p , the mean travelling time t'_r of rolling particle is given by

$$t'_r \approx 2 \sqrt{\frac{2d_p}{g}} \quad (4.36)$$

The contributing mass sources S_q , appearing in the continuity Equation 4.1, for the saltating particles S_{sal} and the rolling grains S_{rol} are given as

$$S_{sal} = S_{sal}^e - S_{sal}^{de} \quad (4.37)$$

and

$$S_{rol} = S_{rol}^e + S_{rol}^{ej} - S_{rol}^{de} \quad (4.38)$$

It is worth noting that, in this work, the mass of ejected particles due to the impacting saltating particles S_{sal}^{ej} were assumed to be part of the mass of rolling grains entrained S_{rol}^e by the flow of water.

4.3.1.4 Particle erosion and Deposition due to shearing slides

The particle mode of transport involving the shearing slides is only considered if the slope angle ϕ is greater than the angle of repose φ . The amount of erosion S_{er}^{sl} , due to shearing slide was described as (Schneiderbauer and Pirker, 2014)

$$S_{er}^{sl} = \begin{cases} \frac{\rho_b \delta A}{\Delta t V} & \phi > \varphi \\ 0 & \phi \leq \varphi \end{cases} \quad (4.39)$$

where δ is the size of a discrete shearing slide (in meter), Δt is the size of time step and ρ_b denotes the bulk density of the packed bed, and it is calculated by

$$\rho_b = \alpha_{pr} \rho_p \quad (4.40)$$

where α_{pr} is the packing ratio and ρ_p the particle density. In this study, the packing ratio of 0.5 was used and this value was obtained from the calibration simulation. From Equation 4.39, the amount of deposition S_{de}^{sl} is computed as

$$S_{de,j}^{sl} = \sum_{l \in \mathcal{C}_j} S_{er,l}^{sl} \quad (4.41)$$

in which a released discrete shearing slide is transferred to the nearest neighbour cell, which is located along the steepest descent and adjacent to the packed bed. The set \mathcal{C}_j is composed of all cells for which cell j is the nearest neighbour cell located along the steepest descent. Note that the shearing slide mode of transport as described above was used to model the sliding motion of sediment inside the scoured hole observed during the experimental tests, which includes both sediment erosion and deposition processes.

4.3.2 Modelling of the Packed Bed Surface Deformation

The deformation or the changing topography of the packed bed is mainly due to occurrence of local erosion and deposition areas at its surface. Therefore, the elevation of the packed bed increases within the deposition zones whereas in the erosion areas it decreases. As a consequence, the local velocity field is affected by the variation of the height of the packed bed. Furthermore, the change of the local fluid flow causes time-dependent deformation of these areas. The methodology used in the present research to model the deformation of the surface packed bed was the Immersed Boundary Method. This method essentially consists of tracking the packed bed surface, in which immersed bodies or packed beds are previously included inside the computational domain. Unlike in some previous work (Patankar et al.,

2000; Uhlmann, 2005) where the immersed bodies are considered as rigid bodies and their motion is described by Lagrangian marker points defining a free flow zone or a rigid body inside the computational domain, Schneiderbauer and Pirker (2010) adopted a different approach by considering the immersed body as a flexible body since erosion and deposition can occur at the surface of the body. Thus, the volume fraction α_b of the packed bed, which is a continuous parameter varying between 0 and 1 is introduced in this approach. The same approach was followed in the present study to capture the different changes of the packed bed topography.

The transport equation of the volume fraction α_b of the packed bed is given by the following diffusion equation

$$\rho_b \frac{\partial \alpha_b}{\partial t} = S_t (\nabla \cdot \Gamma_b \nabla \alpha_b + S_{sd}) \quad (4.42)$$

where the bulk density of the packed bed ρ_b is calculated using Equation 4.40 and S_t is defined as a time scaling factor. In order to subsequently reduce the required computational time, time scale of the fluid t_f (in Equations 4.1 and 4.2) and the time scale of the surface deformation of the packed bed t_h (in Equation 4.42) are decoupled by introducing the scaling factor $S_t = t_f/t_h$. As a result, for a physical time scale t_h , the flow field is considered as steady for a time duration of $S_t t_h$. In the present study, the time scaling factor $S_t = 60$ was used.

The diffusion coefficient Γ_b appearing in Equation 4.42 is given as

$$\Gamma_b = \begin{cases} 0 & \alpha_b \in [0, 1] \\ \lambda_b & \alpha_b \notin [0, 1] \end{cases} \quad (4.43)$$

The diffusion coefficient λ_b was approximated at $\rho \times 10^{-2} = 10$, where $\rho = 1000 \text{ kg.m}^{-3}$ is the density of water. This diffusion coefficient value was obtained from the calibration simulation conducted in the present work. In this model, the surface \mathcal{S} of the packed bed, which is the interface between fluid body and the packed bed, is defined by the value of $\alpha_b = 0.5$. Note that cells with $\alpha_b \in [0, 1[$ are defined as first fluid cells, whereas the neighbour cells with $\alpha_b \geq 1$ are cells located within the packed bed. Figure 4.2 describes the Immersion Boundary Method in which the packed bed is indicated by orange coloured cells, the green coloured cells represent the first fluid cells and the red line is the surface of the packed bed. These definitions were taken from (Schneiderbauer and Pirker, 2014).

Equation 4.43 specifically controls the relocation of the cell layer of first fluid cells in the computational domain. That is, during the erosion process, if the volume fraction α_{b1} of Cell-1 located within the packed bed decreases until $\alpha_{b1} < 0$, then Cell-1 is refilled by diffusion from the neighbour Cell-2 in which

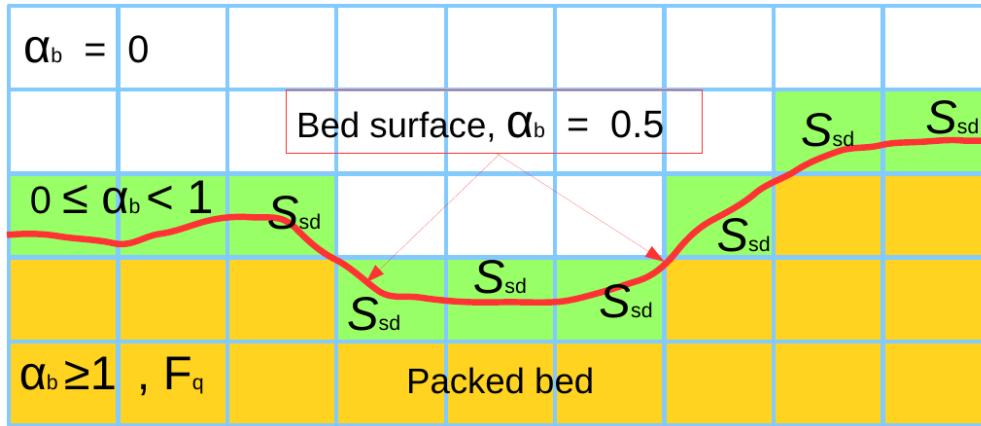


Figure 4.2: Sketch of Immersed Boundary Method

$\alpha_{b2} \geq 1$ until $\alpha_{b1} = 0$ in Cell-1. Finally, the cell layer of first fluid cells is relocated to the neighbour Cell-2 satisfying $\alpha_{b2} \in [0, 1[$. Conversely, if the volume fraction α_{b1} of Cell-1 of the packed bed increases until $\alpha_{b1} > 1$ due to particle accumulation event, then Cell-1 is emptied by diffusion to the neighbour Cell-2 satisfying $\alpha_{b2} < 1$ until $\alpha_{b1} = 1$. The cell layer of the first fluid cells is therefore, relocated to the partially filled neighbour Cell-2 in which $\alpha_{b2} \in [0, 1[$.

The source term S_{sd} , appearing in Equation 4.42 and accounting for the amount of erosion and deposition is given by the sum of the individual contributions to erosion and deposition mentioned in Section 4.3.1.

Thus,

$$S_{sd} = -S_{sal} - S_{rol} + S_{de}^{sl} - S_{er}^{sl} \quad (4.44)$$

or

$$S_{sd} = S_{sal}^{de} - S_{sal}^e + S_{rol}^{de} - S_{rol}^e - S_{rol}^{ej} + S_{de}^{sl} - S_{er}^{sl} \quad (4.45)$$

Note that in the expression of S_{sd} mentioned above, the positive sign denotes the mass contribution from the deposition process while the negative sign describes the mass from the particle erosion at the surface of the packed bed.

In order to prescribe a rigid body motion to the fluid and the particulate phases within the packed bed, a forcing scheme was applied to the momentum equations. The purpose of this scheme was to prescribe a desired velocity values at a selected cells. In this work, the direct forcing approach proposed by Uhlmann (2005) was followed and reads

$$\mathbf{F}_q = -\alpha_q \rho_q \frac{\mathbf{V}_q - \mathbf{V}_b}{\Delta t} \quad (4.46)$$

where \mathbf{F}_q is the additional volumetric forces of phase q appearing in Equation 4.2 and \mathbf{V}_q is the velocity of phase q . Note that Equation 4.46 is only applied to cells inside the packed bed that is, all cells with $\alpha_b \geq 1$. Since the rigid body motion condition was applied, the velocity within the packed bed was set to $\mathbf{V}_b = 0$. The direct forcing approach is equivalent to the rigidity constraint introduced by Patankar et al. (2000) in which the deformation rate tensor in conjunction with the rigid motion is zero inside the packed bed.

The erosion and the deposition processes generally occur under turbulent flow regime at the surface of the packed bed. Therefore, boundary conditions for the turbulent kinetic energy k and the turbulent dissipation rate ε have to be prescribed at the first fluid cells. The turbulent production term G_k , appearing in Equation 4.7 was calculated at the first fluid cells as (Pope, 2000)

$$G_k = \frac{\tau_w^2}{\kappa \rho y_p \sqrt{C_\mu^{1/2} k_p}} \quad \text{for} \quad \alpha_b \in [0, 1[\quad (4.47)$$

where τ_w is the wall shear stress exerted by the mixture phase onto the surface of the packed bed, ρ is the mixture phase density, y_p is the cell-wall distance and k_p is the turbulent kinetic energy at the first fluid cells. The turbulent dissipation ε_p at first fluid cells was applied to Equation 4.8 by direct forcing as proposed by Pope (2000) and reads

$$S_\varepsilon = -\rho \frac{\varepsilon - \varepsilon_p}{\Delta t} \quad \text{for} \quad \alpha_b \in [0, 1[\quad (4.48)$$

where

$$\varepsilon_p = \frac{\sqrt{C_\mu^{3/2} k_p^3}}{\kappa y_p} \quad (4.49)$$

The turbulent kinetic energy k and its dissipation rate ε inside the packed bed have to be adjusted in order to account for the dissipation property of the packed bed. For example, turbulence of a potential background gas flow in real packed beds is dissipated instantaneously due to the presence of particles (Schneiderbauer and Pirker, 2014). As a result, the production of turbulent kinetic energy G_k disappears inside the packed bed, that is

$$G_k = 0 \quad \text{for} \quad \alpha_b \geq 1 \quad (4.50)$$

The production of the turbulent dissipation rate ε which is given in Equation 4.8 by the term $(C_{1\varepsilon} G_k - C_{2\varepsilon} \rho \varepsilon)$ was also

$$C_{1\varepsilon} G_k - C_{2\varepsilon} \rho \varepsilon = 0 \quad \text{for} \quad \alpha_b \geq 1 \quad (4.51)$$

In order to suppress the diffusion of the turbulent quantities within the packed bed a small value closer to zero was given to the turbulent viscosity μ_t and in the calibration simulation conducted in this study

the value was set to

$$\mu_t = 0.001 \quad \text{for} \quad \alpha_b \geq 1 \quad (4.52)$$

Finally, in Equation 4.47, the wall shear stress τ_w exerted by the mixture phase onto the surface of the packed bed was determined by applying the standard logarithmic law-of-wall. This law-of-wall is a simplified version of the original logarithmic law-of-wall (see Equation 4.57) proposed by Prandtl (Fluent, 2011) and it is commonly used in some commercial and open source CFD solvers such as; FLUENT, OpenFOAM. The wall shear stress τ_w is given by

$$\tau_w = \frac{\rho u_p \sqrt{C_\mu^{1/2} k_p}}{U^+} \quad (4.53)$$

with

$$U^* = \frac{u_p}{u^*} = \begin{cases} \frac{1}{\kappa} \ln \left(\frac{EY^*}{f_r} \right) & Y^* \geq 11.225 \\ Y^* & Y^* < 11.225 \end{cases} \quad (4.54)$$

in which U^* is the dimensionless velocity, u_p is the mean velocity at the first fluid cells, u^* is the wall shear velocity, E is an empirical constant with a value of 9.793 and Y^* is a dimensionless distance from the wall, which is given by

$$Y^* = \frac{\rho y_p \sqrt{C_\mu^{1/2} k_p}}{\mu} \quad (4.55)$$

In Equation 4.54, f_r defines a roughness function and it was calculated, in this study as follows

$$f_r = 1 + 0.5 \frac{\rho r \sqrt{C_\mu^{1/2} k_p}}{\mu} \quad (4.56)$$

where r is the physical roughness height. In the standard logarithmic law-of-wall, the wall shear stress τ_w is highly dependent on the turbulent kinetic energy k_p at the first fluid cells as shown in previous Equations (from 4.53 to 4.56).

4.3.3 Estimation of Water Induced Shear Stress for Hydrodynamic Entrainment

The shear velocity u_s^* which appears in Equations 4.15, 4.16 and 4.18, was described as the most sensitive parameter for the numerical simulation of erosion and deposition (Schneiderbauer and Pirker, 2014). Therefore, it is essential to evaluate its value with high accuracy using a suitable empirical formula. The shear velocity can be calculated following the equation for the logarithmic law-of-the-wall given by

$$\frac{u_s}{u_s^*} = \frac{1}{\kappa} \ln \left(\frac{EY^+}{f_r} \right) \quad (4.57)$$

with the dimensionless distance from the wall

$$Y^+ = \frac{\rho_w y_p u_s^*}{\mu_w} \quad (4.58)$$

and the roughness function

$$f_r = 1 + 0.5 \frac{\rho_w r u_s^*}{\mu_w} \quad (4.59)$$

where ρ_w is the water density, u_s^* is the friction velocity exerted by the water flow onto the surface of the packed bed and μ_w is the molecular viscosity of water. Since Y^+ and f_r are not explicit functions, Equation 4.57 has to be solved by the mean of an iterative method, which requires the differentiation of implicit functions and possibly failing to converge (Schneiderbauer and Pirker, 2010). To solve this problem, an explicit form of Equation 4.57 is proposed by substitutions ($y_p \rightarrow EY^+$ and $r \rightarrow f_r$), leading to (Gauer, 2001)

$$u_s(y_p) = \frac{u_s^*}{\kappa} \ln \left(\frac{y_p}{r} \right) \quad (4.60)$$

However, the use of this explicit form of the law-of-the-wall leads to an overestimation of the rise of shear stress as wind speed increases in the fully turbulent logarithmic area (Schneiderbauer and Prokop, 2011).

The second approach to solve the problem involves establishing a direct relationship between the friction velocity u_s^* and the turbulent kinetic energy k_p . In this approach, the turbulent production and dissipation are first assumed to be at equilibrium states and then by using similarity theory (Stull, 1988), the shear velocity u_s^* is given by

$$u_s^* = \sqrt{C_\mu^{1/2} k_p} \quad (4.61)$$

The substitution of Equation 4.61 into Equations 4.57, 4.58 and 4.59 leads to the standard logarithmic law-of-the-wall given in Equations 4.53, 4.54, 4.55 and 4.56. Although this approach yields an explicit formula for the evaluation of u_s^* , its application is only limited to the fully developed steady flows. As a result, recirculation zone and high flow disturbance area are not accounted for in this method.

The third method proposed by Lew et al. (2001), relates to decoupling the shear stress from the turbulent kinetic energy, by applying a linearised implicit scheme in order to solve Equation 4.57. In this approach, the shear stress ($\tau_s = \rho_w u_s^{*2}$) is expressed as

$$\tau_s^{(n+1)} \approx \tau_s^{(n)} + \frac{\partial \tau_s^{(n)}}{\partial \mathbf{U}_s^{(n)}} \left(\mathbf{U}_s^{(n+1)} - \mathbf{U}_s^{(n)} \right) \quad (4.62)$$

The superscript (n) denotes the number of time step. Equation 4.57 can be rearranged, after substituting

$u_s^* = \sqrt{\tau_s/\rho_w}$, as follows

$$\tau_s = -f(u_s) \frac{\mathbf{U}_s}{u_s} \quad (4.63)$$

with

$$f(u_s) = \rho_w \left(\frac{\kappa u_s}{\ln(EY^+/fr)} \right)^2 \quad (4.64)$$

The substitution of Equation 4.63 into Equation 4.62 gives

$$\begin{aligned} \tau_s^{(n+1)} = -f(u_s^{(n)}) & \left(\frac{\mathbf{U}_s^{(n+1)} + \mathbf{U}_s^{(n)}}{u_s^{(n)}} - \frac{\mathbf{U}_s^{(n)} (\mathbf{U}_s^{(n+1)} \cdot \mathbf{U}_s^{(n)})}{(u_s^{(n)})^3} \right) - \\ & \frac{\partial f(u_s^{(n)})}{\partial \mathbf{U}_s^{(n)}} \left(\frac{\mathbf{U}_s^{(n)} (\mathbf{U}_s^{(n+1)} \cdot \mathbf{U}_s^{(n)})}{(u_s^{(n)})^2} - \mathbf{U}_s^{(n)} \right) \end{aligned} \quad (4.65)$$

The advantage of this method is its ability to evaluate the shear stress τ_s with less computational effort and subsequently, increase the τ_s estimation stability (Schneiderbauer and Pirker, 2014).

In the last method, the logarithmic law-of-the-wall (Equation 4.57) can be solved using Newton's Method. This method was chosen, in the present research, for the evaluation of water induced shear stress. Furthermore, it has been shown by Schneiderbauer and Pirker (2014) that the linearised scheme presented in Equation 4.65 leads to the same shear stress evaluation compared to the logarithmic law-of-the-wall solved by Newton's Method.

4.4 Summary

The main focus of this chapter was to underline the different approaches followed in the present study for the development of a coupled fully three-dimensional numerical model capable of simulating bottom outlet flushing process. In this regard, an insight into the basics of fluid dynamics through the Navier-Stokes equations in conjunction with turbulence model was first addressed. The second part focused on describing the method used to model sediment transport processes. Therefore, the sediment erosion and deposition were modelled by considering the following mechanisms of sediment particle transport in water; particle rolling due to the hydrodynamic shearing, particle rebound after impact, particle entrainment due to shear stresses, particle erosion due to impacting particles, particle deposition and accumulation and landslide shearing mode of transport. Finally, the immersion boundary method was used to model the surface deformation of a packed bed.

5. Three-Dimensional Numerical Simulation of the Bottom Outlet Flushing

5.1 Introduction

Bottom outlets, for sediment control are among the most important components of hydraulic structures, especially when sediment yields are high and reservoirs are small. The failure of such structures could undermine the water storage in reservoirs and could also be a serious threat to hydropower project if sediment deposition upstream of the outlet reaches the hydropower intake invert. Consequently, the transport of fine sand into the intake could cause erosive and abrasive damage to the turbines. Although many studies pertaining to bottom outlet, have focused on the flow area downstream of the outlet with high potential to erosion due to high velocity, little research have been conducted to understand the flow and the scouring process on the upstream side of the bottom outlet. These studies mainly used physical models to investigate the scour development and the flow field upstream of the bottom outlet.

In the present research, a fully three-dimensional numerical model coupled in terms of flow field and sediment transport is presented. Numerical models are important tools by means of which the formation of the scour hole upstream of the bottom outlet may be investigated. In addition, numerical models are not limited in terms of scale restrictions of the experimental studies. However, the underlying assumptions on the governing equations, computer constraint in terms of processors and memory capacity, and the computational effort required to obtain the solution are the potential limitations of the numerical models.

The first part of this chapter presents the model setup in which the computational fluid dynamics software, the model geometry and grid cells, the model boundary conditions as well as the solution technique are described in detail. In the second part, results from the numerical simulation are presented and will be compared with experimental measurements of Chapter 3 in the third part of the chapter. Finally, sensitivity analysis of the model to a certain parameters is discussed.

5.2 Numerical Model Setup

The numerical model presented in this work was set up by adopting the following steps:

1. Define the model geometry representing the computational domain.
2. Generate mesh in order to divide the computational area into small grid cells.
3. Set up the model boundary conditions.
4. Adopt a solution technique and procedure.
5. Post-process and analyse simulation results.

More details on the different steps are presented in the following sections.

5.2.1 Computational Fluid Dynamics Software

ANSYS FLUENT is the Computational Fluid Dynamics (CFD) package used in the present research work. ANSYS FLUENT is a computer program which has been used extensively in fluid flow modelling under complex geometries using the finite volume method. ANSYS FLUENT package is composed of:

- A preprocessor engine which includes ANSYS Design Modeler for geometry modelling, ANSYS Meshing for mesh generation.
- A processor engine, FLUENT solver which is a computer code for solving governing equations.
- A postprocessor engine for results visualisation and analysis.

The flow domain in ANSYS FLUENT was first discretised into a large number of cell volumes and then the governing equations were solved in each generated cell by FLUENT solver. The software version used in this study was ANSYS FLUENT version 14.0. The main reasons for using ANSYS FLUENT software package in the present research was first, to avoid the unnecessary time consuming of developing a CFD custom software code and secondly, ANSYS FLUENT is equipped with a special feature named User Defined Function (UDF) which allows the user to define his own functions. However, as mentioned previously in Chapter 4 only the modelling of the flow and the turbulence were carried out in the standard version of ANSYS FLUENT. The sediment transport component was introduced using UDF and therefore, a customised code was developed based on the different particle transport modes explained in Chapter 4.

5.2.2 Model Geometry and Grid Cells

The main goal of the present study was to develop a coupled fully 3D numerical model that is able to accurately simulate the different experimental tests under the same laboratory conditions, discussed in Chapter 3. Therefore, the laboratory flume setup was modelled by applying the same dimension. That is 1 m wide, 1.05 m height and 7 m long of which 2 m was covered by the packed bed with a thickness of 0.26 m. The bottom outlet orifice diameter was 0.09 m which was extended by a pipe of 1 m length with the same diameter. Note that the laboratory flume was 40 m long but only 7 m long was modelled because the area of interest was located just upstream of the bottom outlet and the distance used in the numerical model was enough to get a fully developed and stable flow at the surface of the packed bed. The laboratory test results also showed that the maximum scour length upstream of the bottom outlet was less than 1 m and therefore, only 2 m length of the packed bed was modelled instead of 5 m as it was the case in the physical model. The shortening of the model length has significantly reduced the number of generated cells and subsequently, the computational time was considerably decreased. Figure 5.1 shows the modelled geometry of the laboratory setup as presented in Design Modeler.

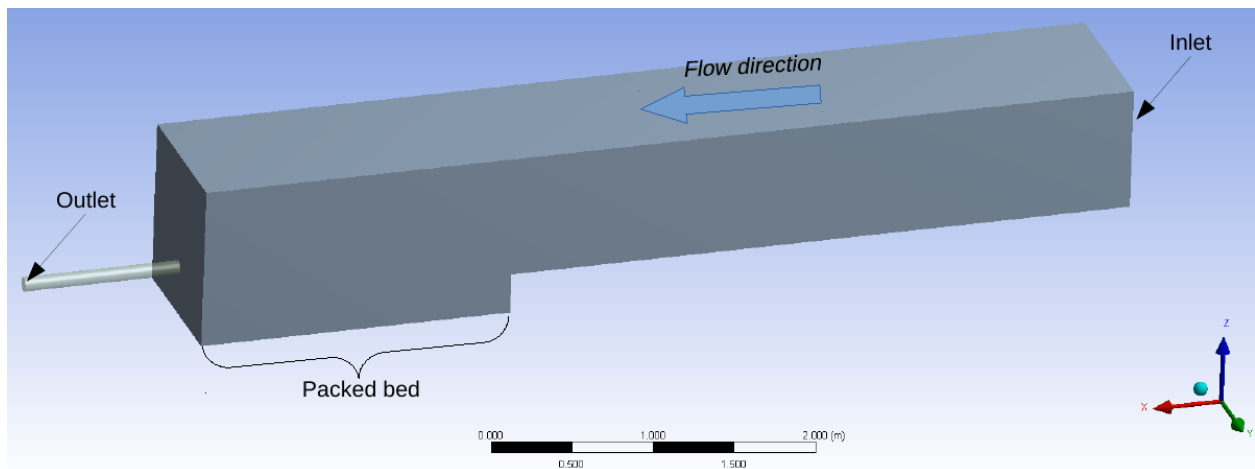


Figure 5.1: Computational model geometry

The most crucial step in developing a numerical model is the construction of an appropriate computational grid in order to obtain a stable and grid independent solution. The governing equations are solved at the nodes of this grid iteratively until convergence is reached for important model parameters such as flow velocity and direction, and pressure. The construction of mesh can lead to high number of cells which in return may require a long computational time for a single solution. Therefore, the

modelling of the physical environment have to be done in the most efficient way taking into account the different aspects mentioned above. In this study, the geometrical cell volume chosen was a hexahedral shape. This type of mesh was chosen because it provides high-quality solutions with fewer cells/nodes particularly for flow-aligned geometries, which was the case in this study. Furthermore, the hexahedron mesh reduces numerical diffusion when the mesh is aligned with the flow. Numerical diffusion is referred to as an overestimation of the diffusion coefficient by the model.

Cells in the direction perpendicular to the flow represented in the model by Y-axis, were uniform in size while in the flow direction (X-axis) finer cells were used closer to the upstream of the bottom outlet, area of high potential of erosion and flow turbulence, and further upstream of the flume, coarser cells were applied. In the vertical direction (Z-axis) the packed bed area was made of finer mesh, which increases as approaching the free surface of water. Figure 5.2 shows the generated mesh used in the simulation and Table 5.1 provides some information on the number of cells as well as the cell quality and its resolution.

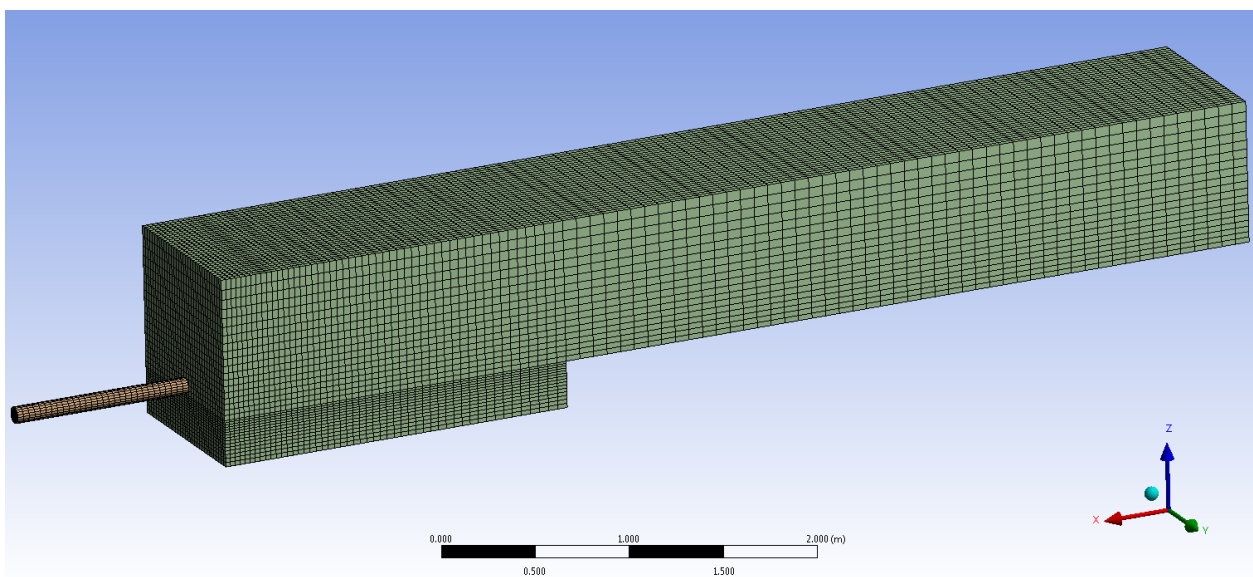


Figure 5.2: Computational grid cell

A mesh is defined as good quality mesh when the orthogonal quality is 1 and bad when this value is 0. The generated mesh in this study has an average orthogonal quality of 0.99 which is very close to 1 (see Table 5.1). This shows that the mesh used has an acceptable quality.

Table 5.1: Details of generated mesh

Number of cells	90210
Number of nodes	97883
Minimum cell size (m)	0.017
Maximum cell size (m)	0.08
Average skewness	0.006
Average orthogonal quality	0.99

5.2.3 Model Boundary Conditions

Boundary conditions are very important in computational fluid dynamics and they specify physical values at the boundaries of the computational domain. Therefore, it is crucial to define these conditions correctly and understand their role in the numerical algorithm because boundary conditions have a direct impact on the quality of the final results of the simulation. In ANSYS FLUENT a limited set of boundary types is available and the choice of the boundary condition type should comply with the availability of the flow information at that particular surface location. In this study, four boundary condition types were used to model the laboratory tests namely, the inlet-flux, the outlet-pressure, the symmetry and the wall.

The inlet-flux boundary type was used as inlet boundary because the discharge at the bottom outlet was known for being measured during the laboratory tests. The flows prescribed at the inlet were the same flow as used in the physical model namely; $0.036 \text{ m}^3/\text{s}$ for Test 1, $0.021 \text{ m}^3/\text{s}$ for Test 2 and $0.012 \text{ m}^3/\text{s}$ for Test 3. The hydraulic diameter ($D_h = 4/(A/P)$) of 1 m , where A is the inlet cross section area and P its perimeter. The default value of 5% was used for the turbulent intensity at the boundary inlet.

The outlet-pressure type was set at the outlet boundary, which requires to specify a gauge pressure. In this study, the gauge pressure was set to 0 Pa , and since in ANSYS FLUENT the absolute pressure is equal to the sum of a reference pressure and a gauge pressure, then the reference pressure is set to the atmospheric pressure (101320 Pa). The hydraulic diameter (D_h) of 0.09 m was used and the turbulent intensity of 5% was also prescribed as boundary conditions at the outlet.

The free surface in this study was modelled by using a symmetry boundary type, which implies that the velocity component normal to the free surface is zero, as well as the gradients of all the other flow variables normal to the symmetry axis (Fluent, 2011). This boundary condition was suitable to describe

the free surface in the present research, because the water level was constant in the numerical model as it was during the laboratory tests.

The sidewalls and the floor of the flume were set as wall boundary type in which no-slip condition was specified.

5.2.4 Numerical Solution Technique and Procedure

In this section, the different steps involving the settings of the numerical model through the Graphical User Interface (GUI) of ANSYS FLUENT are discussed. First, the ANSYS FLUENT launcher was started by activating the following options; 3D , double precision and parallel as processing option. In order to speed up the computational time, 12 processors were used in parallel for the processing option. This enables the computational task to be shared amongst the processors and therefore, the computational time was considerably reduced. The mesh file previously generated in design Modeler was loaded in ANSYS FLUENT interface. The User-Defined-Function was compiled and loaded. The solver options used were; Pressure Based for solver type, absolute for velocity formulation type and transient for time. The gravitational acceleration was activated in this simulation.

The eulerian model with three phases were chosen in the multiphase options. The primary phase was water and the remaining two phases were used to model saltating and rolling particles. Material properties such as viscosity, diffusivity, density and particle diameter were specified for each phase. The mass and momentum source term provided by the User Defined Function (UDF) were hooked for each phase and passed on to FLuent solver in order to implement the modelling of sediment transport and the deformation of surface of the packed bed.

In the viscous model, the $k-\epsilon$ model in conjunction with the standard wall functions were chosen for the turbulence model. In this option, the turbulent viscosity was computed using the customised UDF code.

In the operating conditions of the fluid domain, the operating pressure was set to atmospheric pressure (101325 Pa) and the reference pressure in this model was located at the free surface. The boundary conditions were specified using the laboratory test flow values as discussed in previous sections.

For the solution methods, the Phase Coupled SIMPLE scheme was used as Pressure-Velocity Coupling method and spatial discretisation schemes for the solution variables were set up in the model.

The solution variables in the computational domain were first initialised from the inlet value and then by using region adaption function from GUI, the area representing the packed bed in the model was marked and patched with a new User Defined Scalar (UDS) value and velocity. The UDS patched value representing the volume fraction of the packed bed was 1.15 and the initial velocity was set to 0 at the marked region.

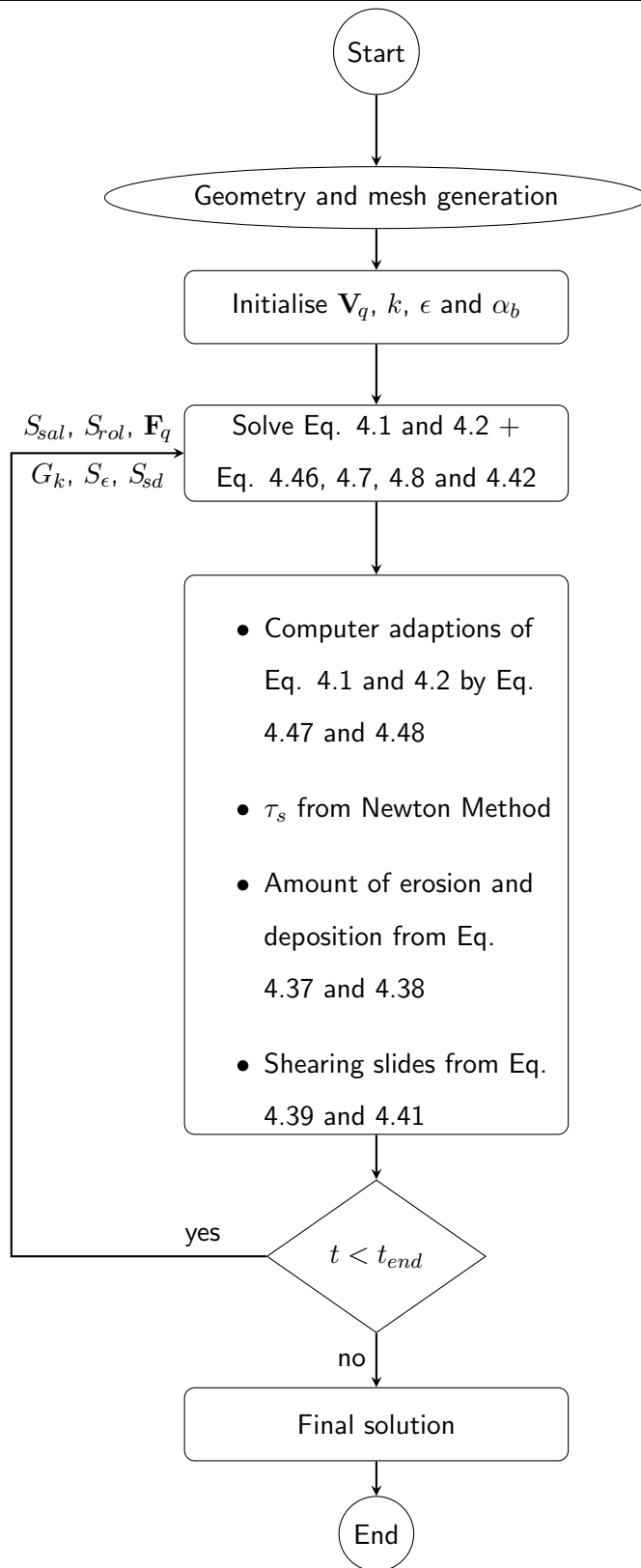
In order to run the calculations the time-step size, the number of time-steps and the maximum number of iterations per time-step were specified in the model. The time step size was set to $0.001s$ and maximum iteration per time step was set to 10. Note that these values were obtained after many trial runs and they are found to be appropriate in terms of solution stability and convergence. The number of time step was taken from the longest laboratory run time test which was around 30 min . By applying the time scale ($T = 60$) discussed in Section 4.3.2, the number of time step was set to $30000s$ and multiplying this value with the time step size gives the time duration of $30s$ which is actually 30 min . According to the time scale adopted in this model, $1s$ is equivalent to the physical time of $60s$.

The governing equations were finally solved for each time-step and results are plotted and analysed. The model procedure is summarised in the following flowchart in which t is time.

Note that the computer used to run the different simulations in this study was a Dell Precision T5600 tower system running Windows 7 Professional. The specifications are as follows:

- Dual Intel Xeon CPU *E5 – 2643* 3.30 GHz , 3.30 GHz (2×8 cores CPUs)
- 16 GB RAM
- NVIDIA Quadro graphics card

The processing time required for one numerical simulation using the above mentioned computer was about 48 hours.

**Figure 5.3: The proposed numerical model flowchart**

5.3 Simulation Results

In this section, simulation results of the experimental tests are discussed. These simulated experimental tests included the laboratory tests (Test 1 to 3) discussed in Chapter 3 and the physical model test taken from Powell (2007). The latter was simulated because it provided a more comprehensive experimental result for the validation of the present 3D fully coupled numerical model. For example, in this laboratory test results a vertical and horizontal distribution of flow velocity upstream of the bottom orifice were available for comparison against numerical model results.

5.3.1 Model Calibration

The first simulation consisted of calibrating the model against the laboratory data. The parameter chosen for calibration was the dimensionless empirical coefficient C'_η , which appears in Equation 4.16. As mentioned in Section 4.3.1.1, this coefficient would considerably vary according to the case study. Furthermore, different values of C'_η presented in the literature were based on air-particle condition studies while water-particle case is addressed in the present research. In this regard, the model was calibrated against experimental results of Test 1, which corresponds to a highest simulated flow ($0.036 \text{ m}^3/\text{s}$). After the model was successfully calibrated, Test 2, Test 3 and test from the literature (Test 4) were simulated using the first simulation setup with the corresponding flow rate for each test.

5.3.2 Bed Deformation Results

The primary objective of the simulations conducted in this study was to predict the laboratory test results. Therefore, the final simulated scour hole should represent the equilibrium condition as it was the case during the experimental study. Figure 5.4 shows the longitudinal variation with time of the scour hole in the centreline.

It can be seen that the scour depth increases at the beginning of the simulation and then reduces with increasing time until there is no more change. This shows that the final scour hole from the simulation corresponds to the equilibrium condition.

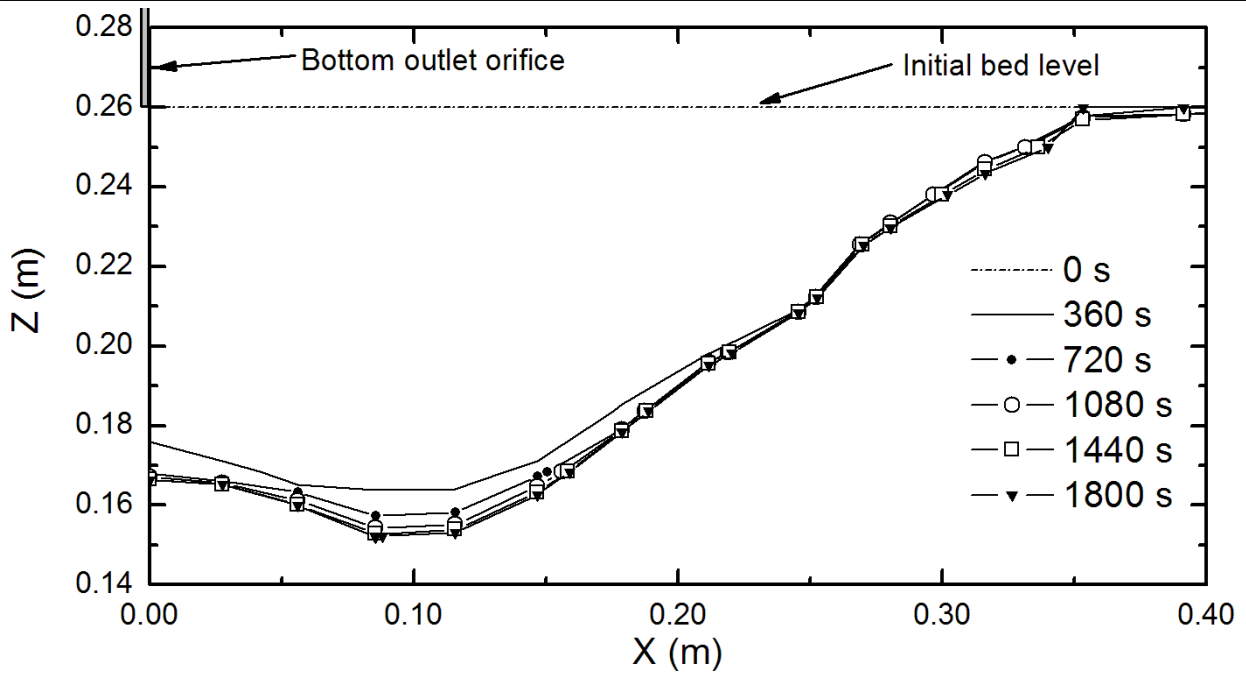


Figure 5.4: Simulated longitudinal variation of the scour hole with time for Test 1

Figure 5.5 depicts the simulated scour hole result for Test 1 in three-dimensional view. It shows that the model accurately simulated the elliptical shape of the edge of the scour hole. Furthermore, the scour hole is located closer to the bottom outlet, while further upstream, the surface of the pack bed remains at its initial level. That is there was no bed deformation or erosion that occurred at that part of the packed bed.

The shape of the scour hole was similar for all the simulated tests and the simulated results for Tests 2, 3 and 4 are presented in Appendix B.

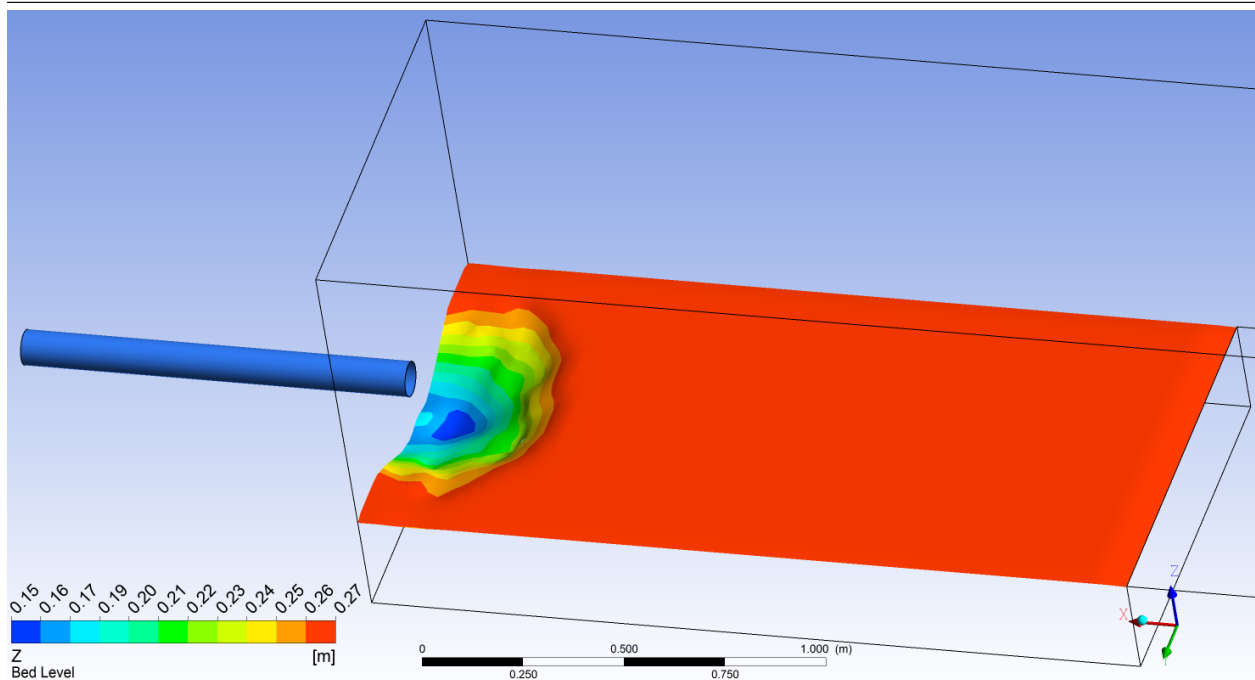


Figure 5.5: Simulated scour hole for Test 1 (after 1800 s)

5.3.3 Hydrodynamic Results

The acceleration of the flow through the bottom orifice causes a drop in pressure at the bed just upstream of the bottom outlet. Figure 5.6 depicts the simulated static pressure distribution upstream of the bottom outlet. It shows that the pressure dropped below hydrostatic for a region closer to the bottom outlet, which corresponds to the location of the scour hole. The drop in pressure begins at a distance approximately 9 times the orifice diameter (0.09 m), upstream of the bottom outlet. At the bottom outlet, the pressure decreased to 55% of the hydrostatic pressure as shown in Figure 5.6. Similar observations were made by Rajaratnam and Humphries (1982) when they studied the flow behaviour upstream of a sluice gate. The authors found that the decrease in pressure just upstream of the gate was approximately 40% of the hydrostatic pressure and this drop in pressure was extended to a distance of approximately 5 times the sluice gate opening.

The simulated flow field upstream of the bottom outlet for Test 1 is presented in Figures 5.7 to 5.10. The simulated velocity contours show that the area with high velocity is located closer to the bottom outlet. The flow is accelerated at that particular area due to the contraction caused by the bottom outlet. This zone was defined, in this study, as the primary scour area in Chapter 3. Furthermore, the

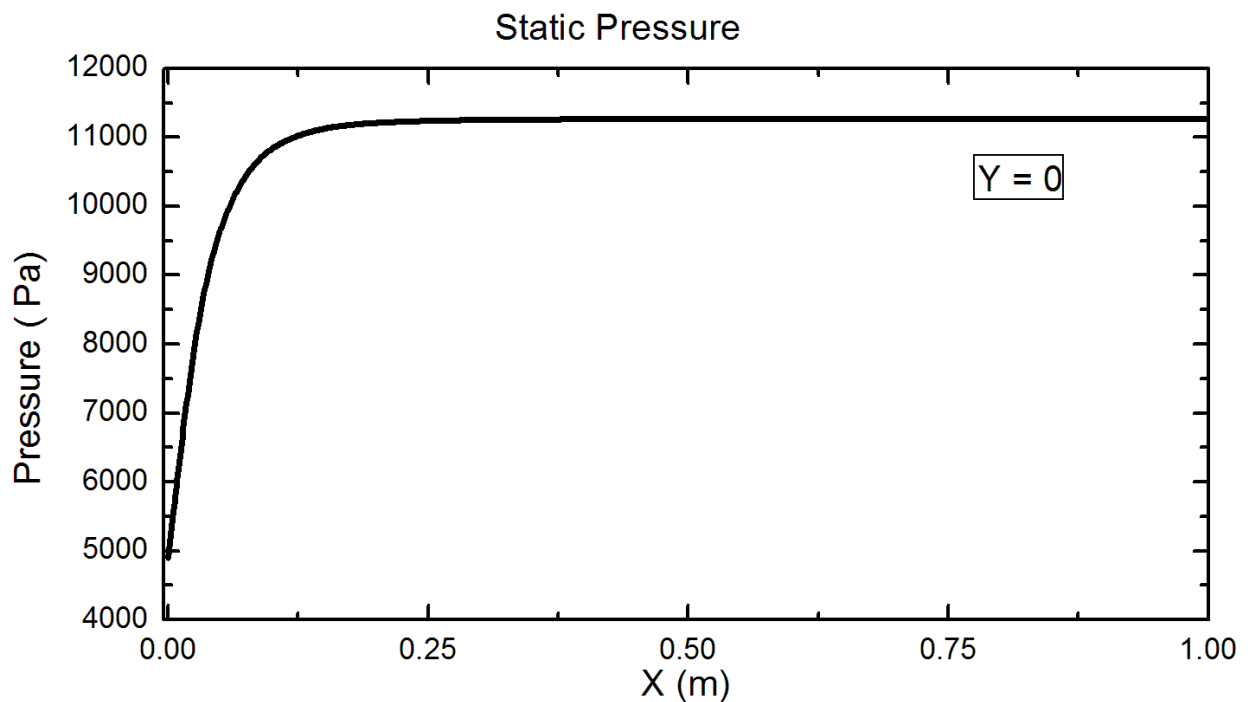


Figure 5.6: Simulated static pressure distribution at the bed

contour of simulated velocity at the bed shows a transitional area where the velocity is closer to zero. This zone is located just at the top of the slope inside the scour hole (see Figure 5.7). The streamline representing the path of the simulated flow is shown in Figure 5.8. Simulated Eddy viscosity is presented in Figure 5.9 and it shows that inside the scour hole, the eddy viscosity is higher closer to the bottom outlet while at the transitional zone it is closer to zero. It is evident from the comparison of the contours of the simulated shear stress in Figure 5.10 and the simulated scour hole in Figure 5.5 that the location of the area with high shear stress coincides with the zone of maximum depth inside the scour hole. This confirms that the primary scour area is driven by the shear stress exerted by the flow onto the surface of the bed. The simulated flow results for Tests 2, 3 and 4 are given in Appendix B.

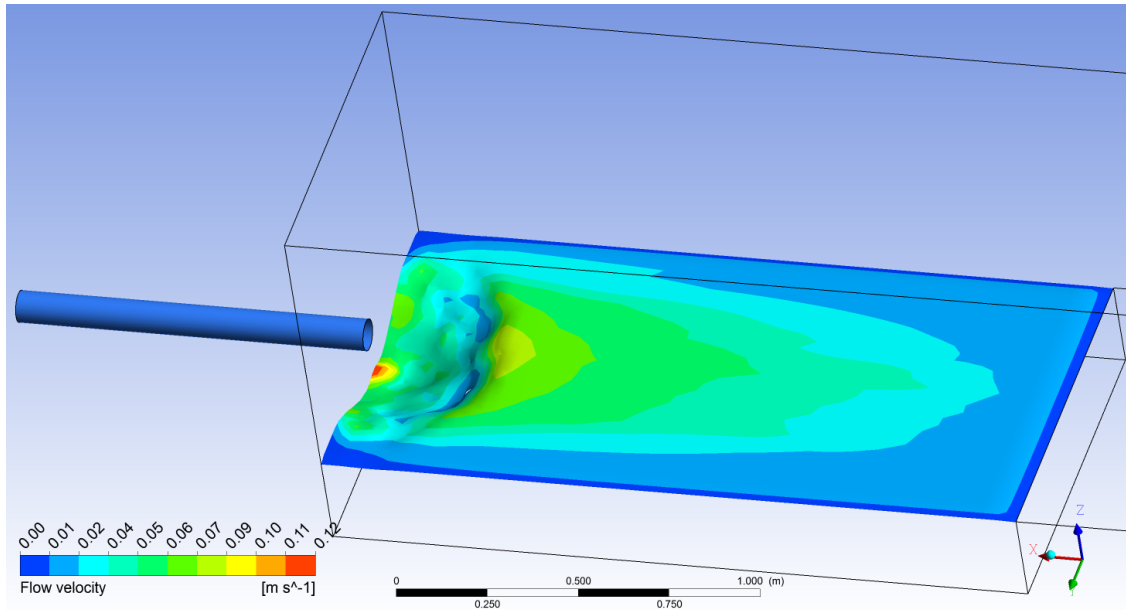


Figure 5.7: Contours of simulated flow velocity for Test 1 (after 1800 s)

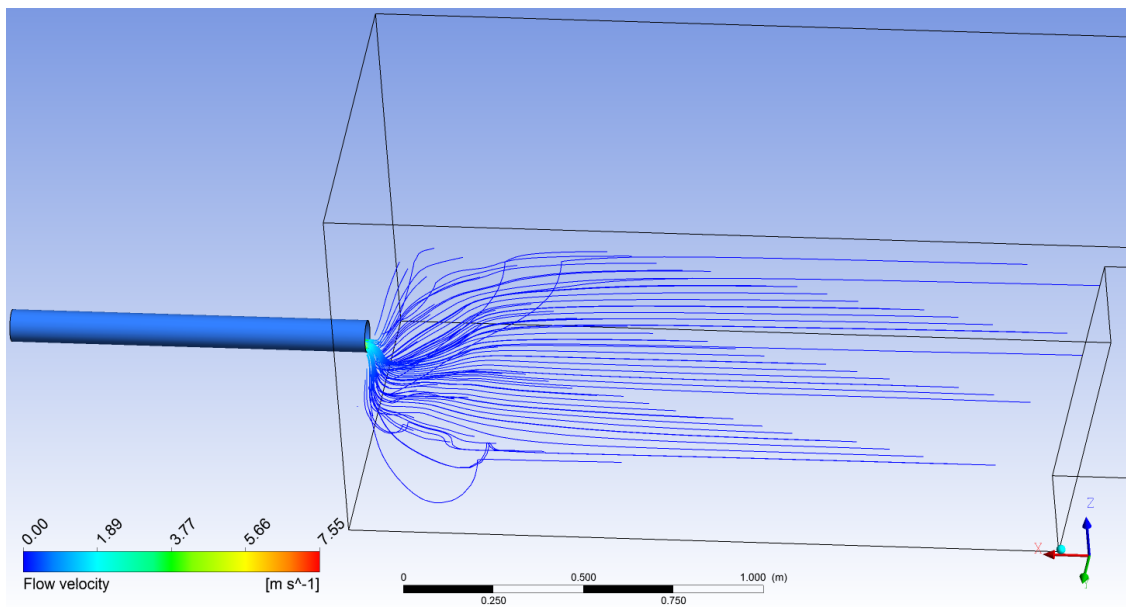


Figure 5.8: Simulated flow streamline for Test 1 (after 1800 s)

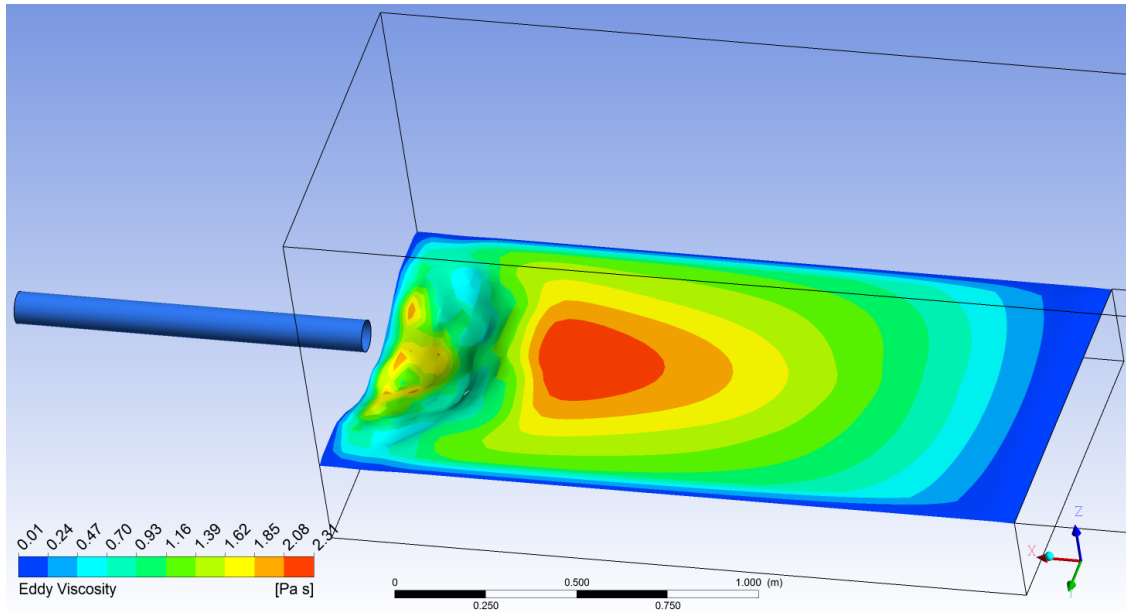


Figure 5.9: Contours of the simulated eddy viscosity for Test 1 (after 1800 s)

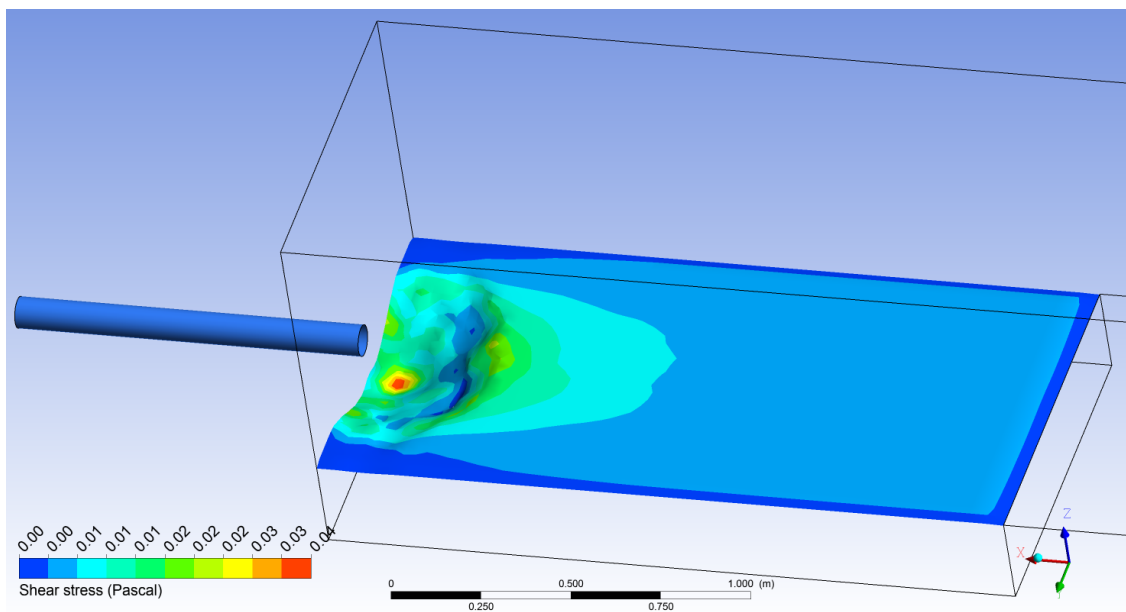


Figure 5.10: Contours of the simulated bed shear stress for Test 1 (after 1800 s)

5.4 Validation of the Simulation Results against Experimental Data

In order to validate the numerical model, it has to be compared with the experimental measurements conducted in Chapter 3. In the first part of this section, the simulated bed deformation in terms of scour bed extent and shape are compared with experimental data. This is followed by more detailed comparison of the cross section profiles of the scour hole. In the third part the simulated flow field is compared with experimental data from the literature.

5.4.1 Comparison of Bed Deformation

Figures 5.11 to 5.13 show the contour map of the scour hole of the experimental tests compared with the simulation results. It can be seen from the contour map that the simulated scour hole reasonably agrees with the measurements from the experimental test in terms of the scour extent and the maximum scour depth. However, for Test 3 the scour width was overestimated compared to the experimental test result.

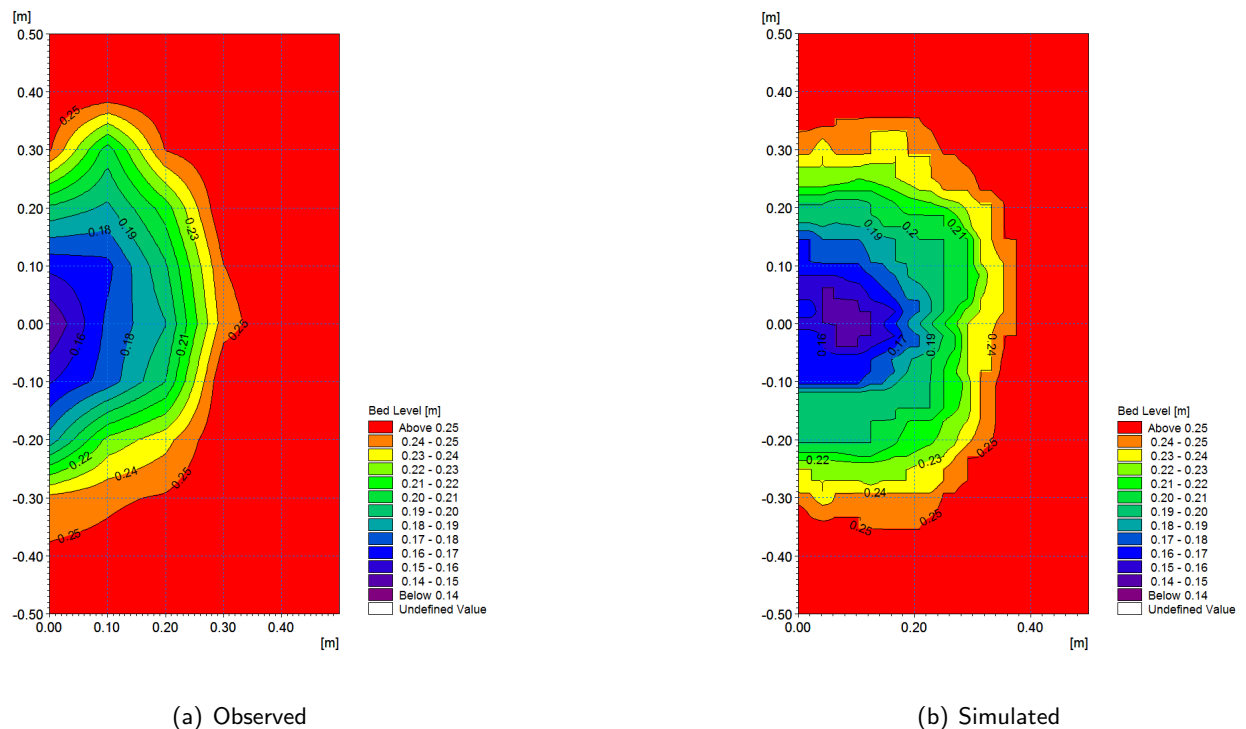


Figure 5.11: Plan view of final bed level for Test 1

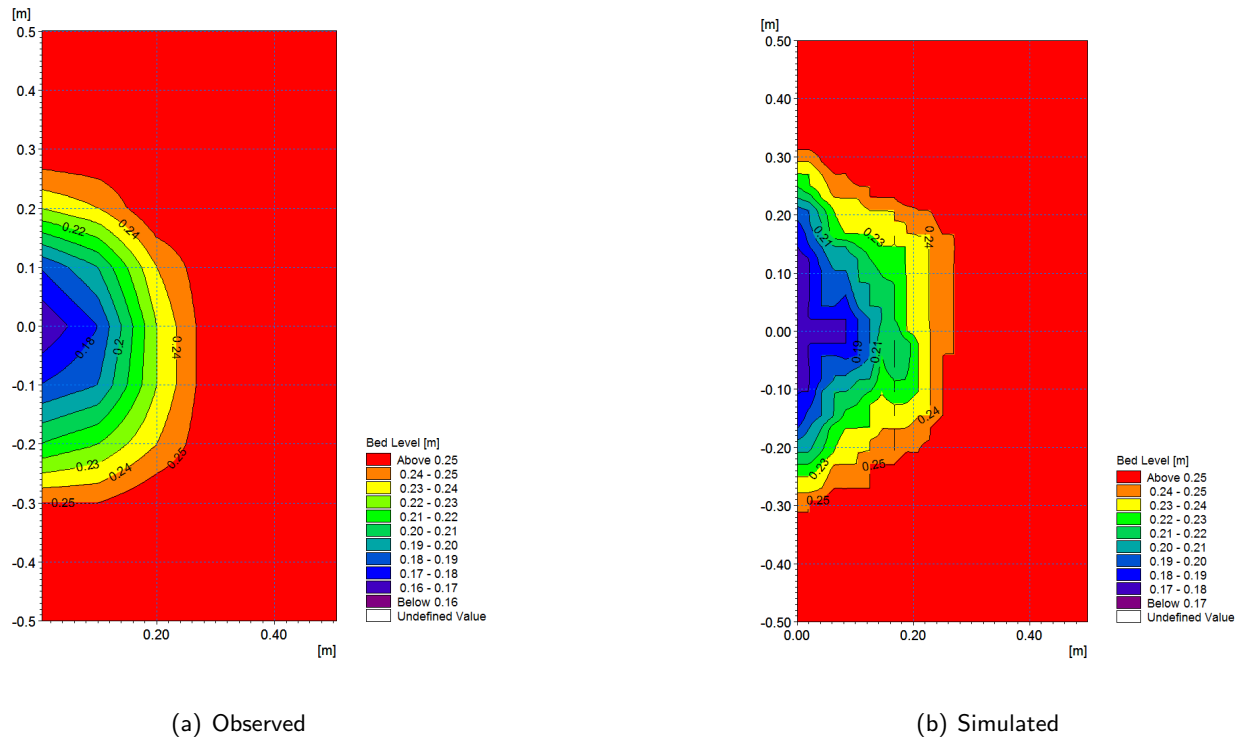


Figure 5.12: Plan view of final bed level for Test 2

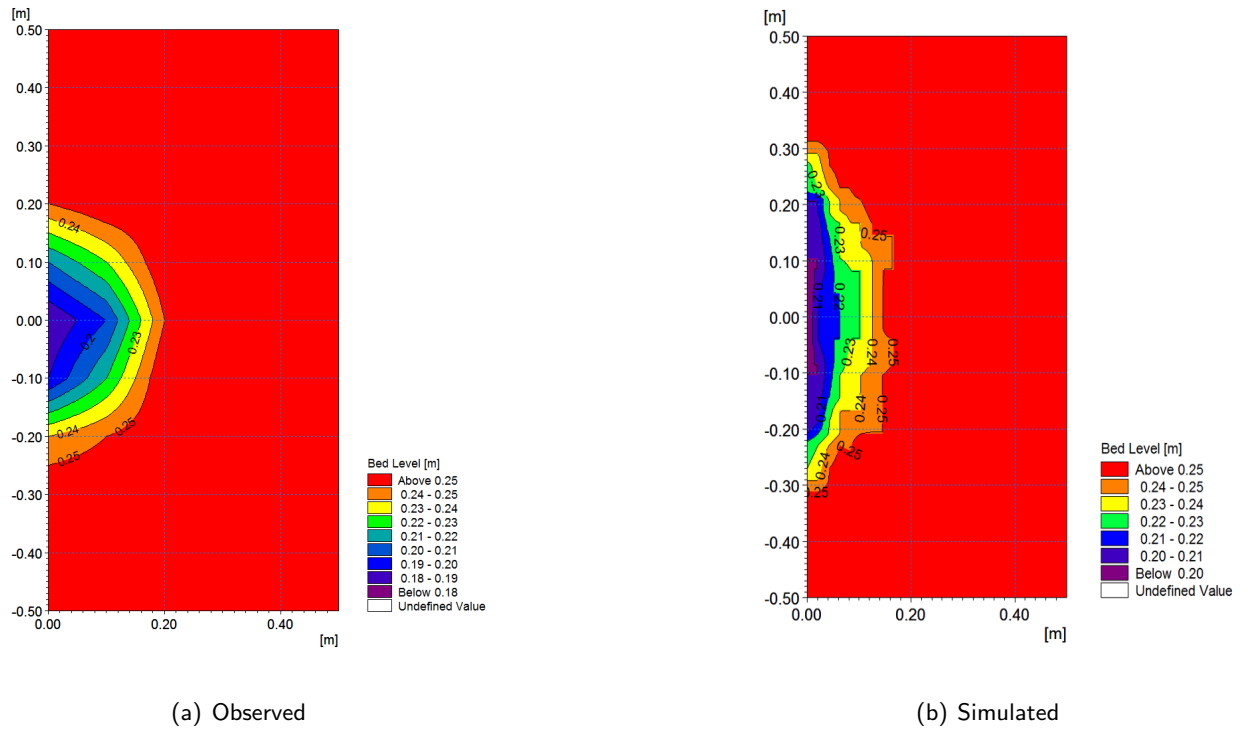


Figure 5.13: Plan view of final bed level for Test 3

5.4.2 Comparison of Scour Hole Profiles

The simulated lateral bed profiles, were plotted every 0.05 m away from the orifice and then, compared with measurements. The simulated longitudinal profiles of the scour hole along the x-axis upstream of the bottom outlet with 0.10 m interval on both sides of the centreline were also compared with experimental results. Besides the three experimental tests simulations, an additional experimental test was simulated. This experimental work was conducted by Powell (2007) to investigate the scour process and the flow behaviour upstream of the bottom orifice. Since the different experimental tests carried out in the present study did not provide measurements for velocity distribution upstream of the bottom outlet, Powell (2007)'s laboratory test was then simulated in order to validate the proposed numerical model in terms of velocity field prediction upstream of the bottom outlet. The model geometry consisted of a 2.14 m wide, 6 m long and 1.06 m height flume, in which a sand of 0.73 mm was used as packed bed. The surface of the bed was levelled with the bottom orifice invert located at 0.3 m from the flume floor. Powell (2007) used a bottom orifice diameter of 0.152 m and tested many scenarios. However, only one scenario from the author's work was simulated in this study. In this scenario, the water head relative to the orifice invert was 0.76 m . In Table 5.2, the simulated maximum scour depth (D_s), the scour width (W_s), the scour length (L_s) and the Ratio ($= L_s/(W_s/2)$) are compared with experimental results. The simulated maximum scour depth for all tests is in good agreement with the measurement as shown in Table 5.2. The scour width and the length were also well predicted by the present numerical model.

The simulated scour hole profiles for Test 1 ($0.036\text{ m}^3/\text{s}$), Test 2 ($0.021\text{ m}^3/\text{s}$), Test 3 ($0.012\text{ m}^3/\text{s}$), as well as Test 4 ($0.054\text{ m}^3/\text{s}$) were compared with experimental results. These are shown in Figures 5.14 to 5.20. From these figures, it can be observed that the shape of the simulated lateral and longitudinal bed profiles were well predicted by the present numerical model for all tests. However, the scour depth for cross sections away from the bottom outlet is overestimated by the numerical model for Test 1. For Test 4 the measured cross sections are deeper than the simulated cross sections. Powell (2007) concluded during the experimental tests that the vortex played a major role in the scour process upstream of the bottom outlet. Based on this, the discrepancy between the simulated cross sections and the measurement for test 4 could be due to the fact that the vortex is not fully developed in the numerical model to produce more erosion as observed during the experimental test.

Table 5.2: Summary of result comparisons

	Q (m^3/s)	Ds (m)		Ws (m)		Ls (m)		Ratio	
		Obs.	Sim.	Obs.	Sim.	Obs.	Sim.	Obs.	Sim.
Test 1	0.036	0.12	0.12	0.65	0.61	0.33	0.37	1.02	1.21
Test 2	0.021	0.10	0.09	0.56	0.58	0.29	0.29	1.04	1.00
Test 3	0.012	0.08	0.06	0.46	0.55	0.20	0.17	0.87	0.62
Test 4	0.054	0.10	0.09	0.66	0.72	0.33	0.33	0.91	0.92

Obs. = Observed and Sim. = Simulated

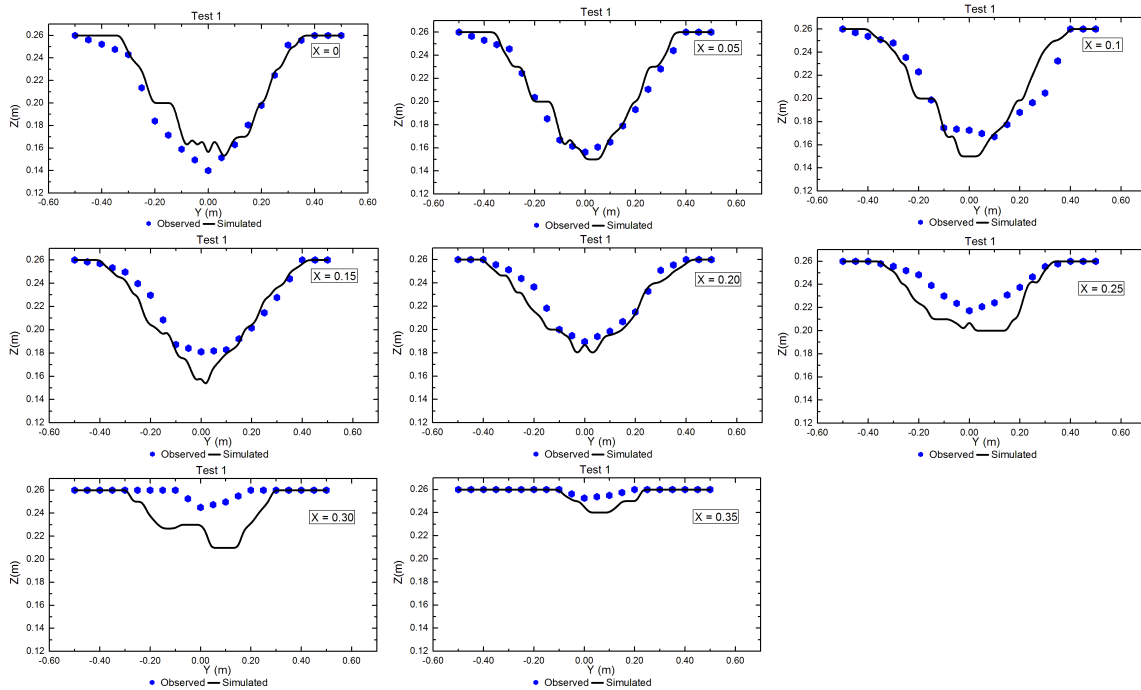


Figure 5.14: Lateral bed profile results comparison for Test1

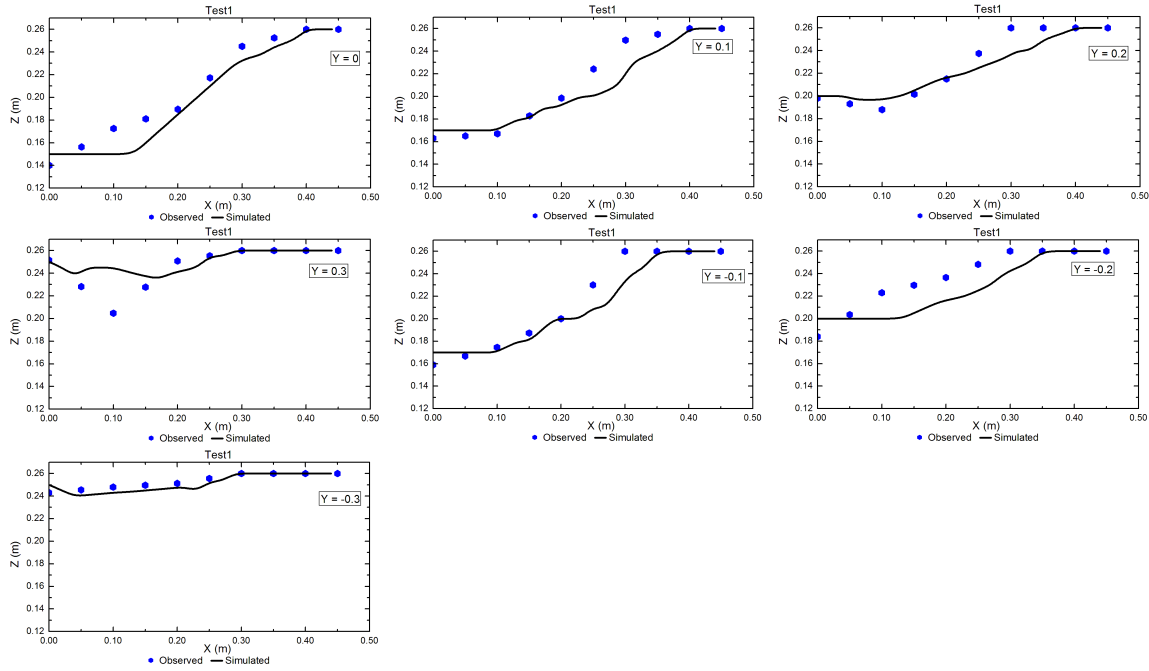


Figure 5.15: Longitudinal bed profile results comparison for Test 1

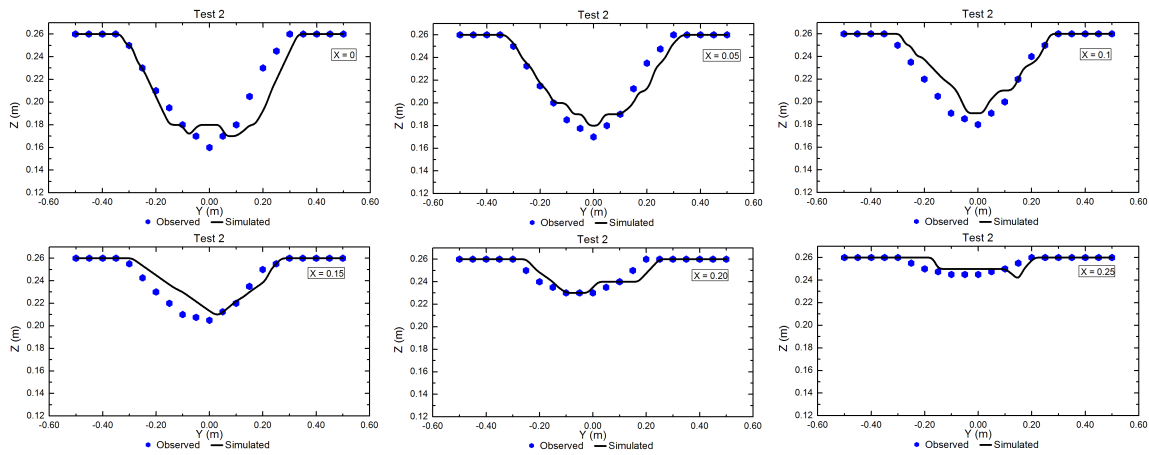


Figure 5.16: Lateral bed profile results comparison for Test 2

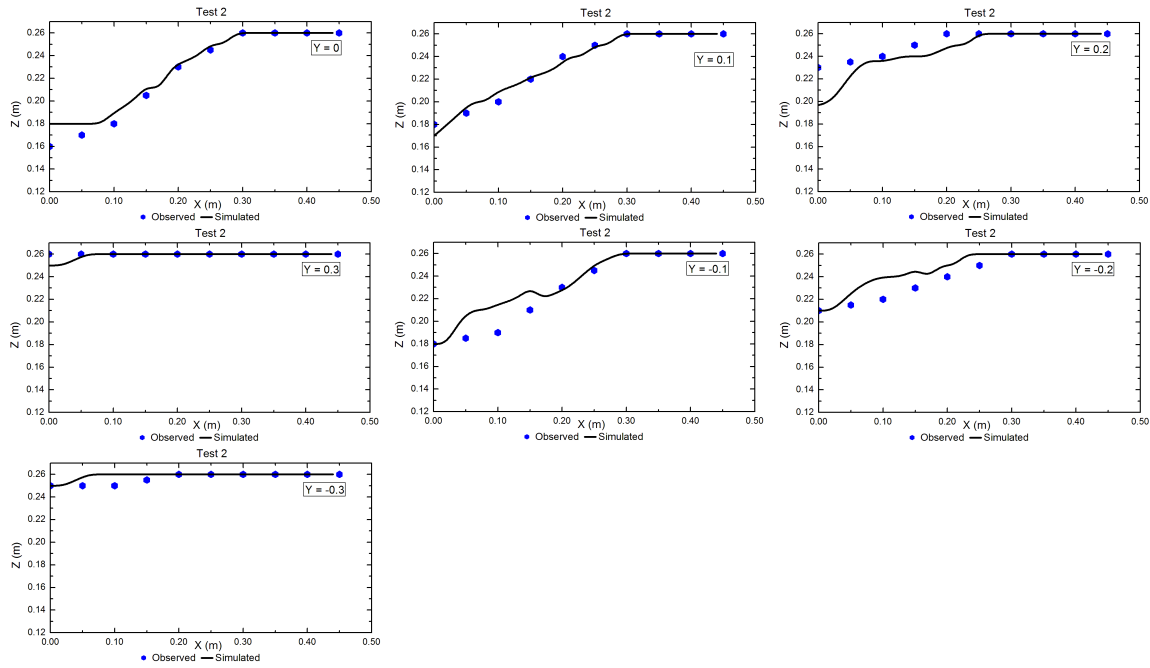


Figure 5.17: Longitudinal bed profile results comparison for Test 2

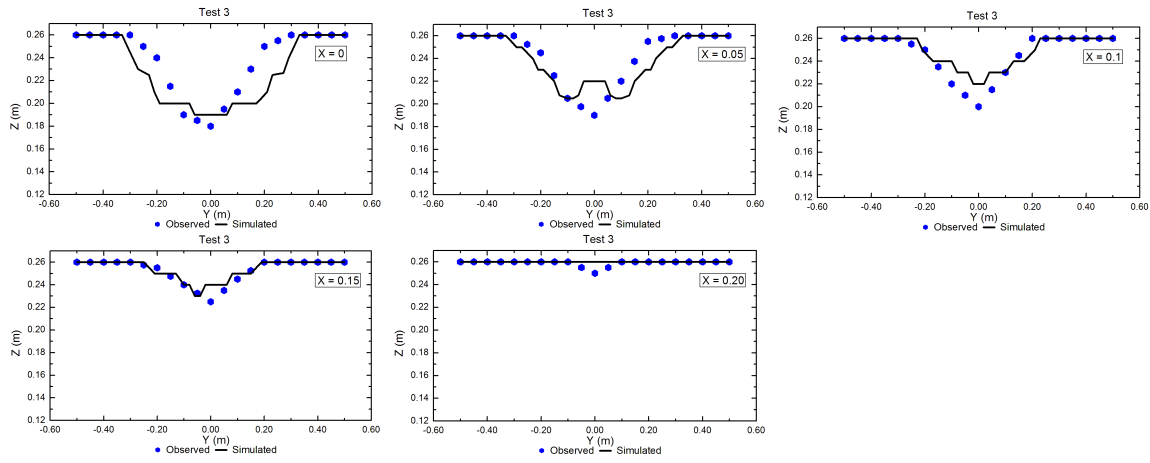


Figure 5.18: Lateral bed profile results comparison for Test 3

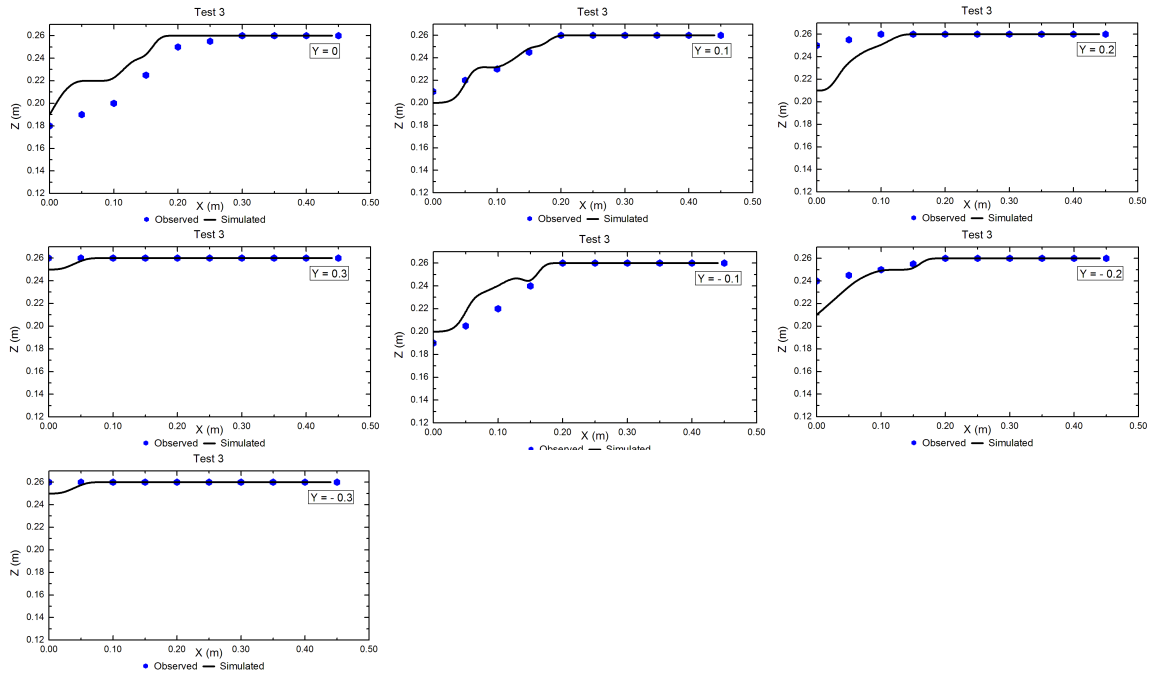


Figure 5.19: Longitudinal bed profile results comparison for Test 3

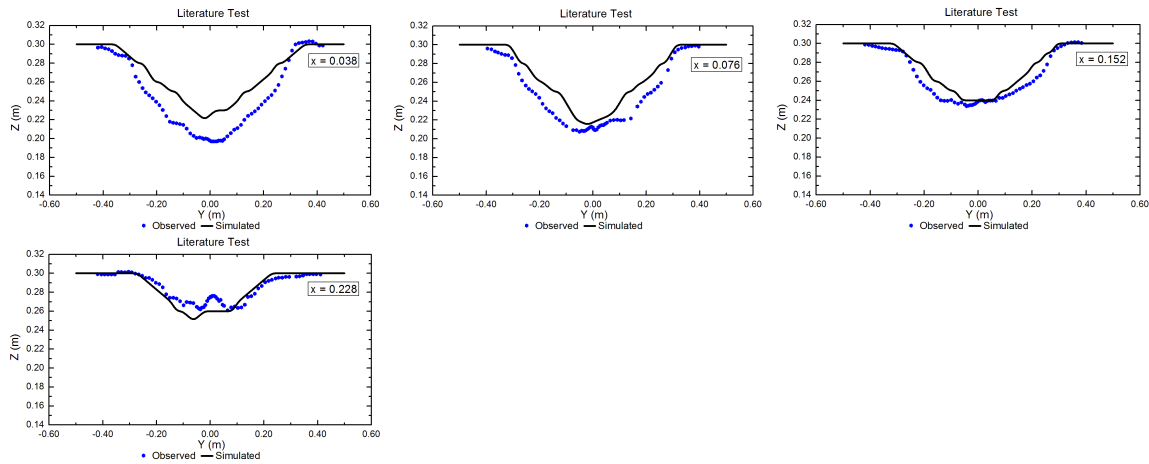


Figure 5.20: Lateral bed profile results comparison for Test 4

5.4.3 Comparison of Flow Velocity

The simulated velocity variations on both vertical and horizontal plane are compared with velocity measurements from Test 4 (Figures 5.21 to 5.23). Overall, the velocity profile shape and values are well predicted by the numerical model, even though velocity is being slightly overestimated for the velocity profiles in both the vertical and horizontal plane away from the bottom outlet. The velocity variation on the centreline is however, in good agreement with the measurements as shown in Figure 5.23.

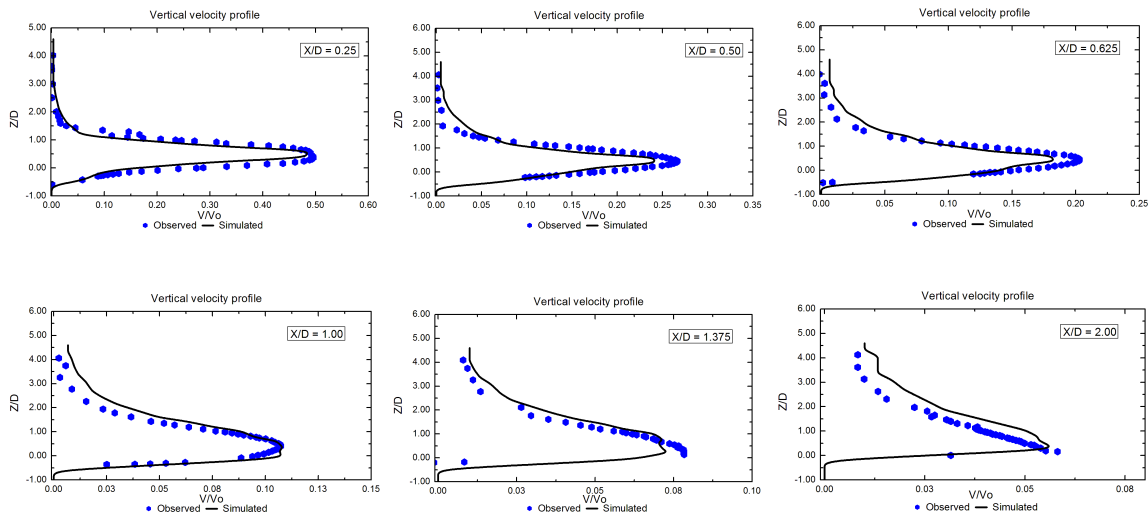


Figure 5.21: Results comparison of velocity variation on the vertical plane

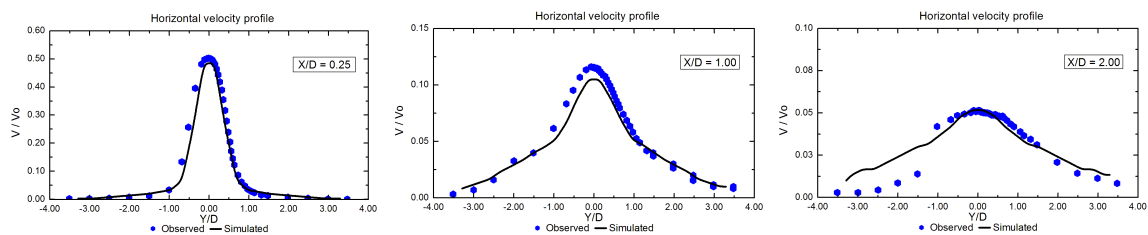


Figure 5.22: Results comparison of velocity variation on the horizontal plane

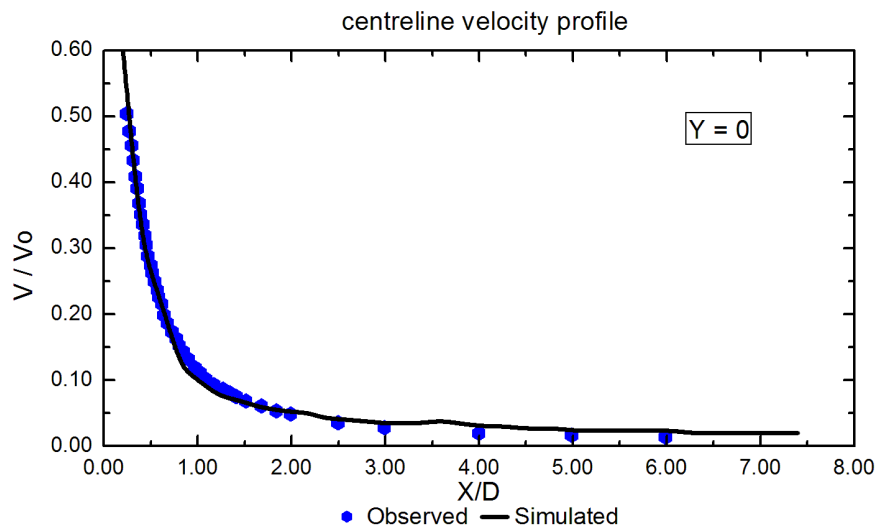


Figure 5.23: Results comparison of velocity variation on the centreline

5.5 Sensitivity Analysis of the Proposed Numerical Model

This section investigates how certain parameters of the proposed numerical model affect the final simulation results. In this regard, only parameters with physical meanings are considered for sensitivity analysis. The sensitivity study consisted of simulating two different values of a given parameter and then comparing the results with the calibration simulation results (Test 1) displayed as reference simulation (Ref) in the following graphs. The following gives more details on the parameters used for sensitivity test as well as the results of this analysis. Results are given under the form of lateral and longitudinal profile as well as the scour hole extent.

5.5.1 Creeping Parameter

The creeping or rolling parameter (Cr) is a parameter in the present numerical model, which gives an indication on the dominant transport mode between the saltating and the rolling particle modes. Its value varies between 0 and 1. It is 1 when particles are exclusively transported through creeping mode and 0 when saltating is the only way by which particles are transported by the flow. Figure 5.24 shows the sensitivity results of the creeping parameter (Cr). Figures 5.24-(a) and 5.24-(b) show that the scour depth increases with increasing creeping coefficient (Cr). Furthermore, the edge of the scour hole becomes wider and longer as the creeping (Cr) value increases as shown in Figure 5.24-(c). This means

that the scour is deeper when the dominant transport mode of particles is saltating. Clearly, a saltating particle is more likely to be entrained by the flow of water than a rolling particle that remains most of the time at the surface of bed. The creeping coefficient (Cr), therefore, is a sensitive parameter in the present numerical model.

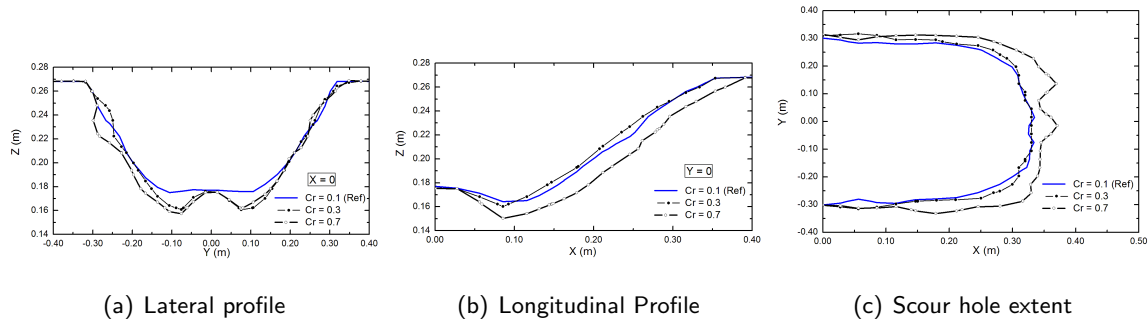


Figure 5.24: Results of sensitivity analysis for creeping parameter

5.5.2 Diffusion Coefficient

The diffusion coefficient (see Equation 4.43) is linked to the volume fraction of the pack bed. Figure 5.25 shows the simulation results done on three different values of the diffusion coefficient. The results show that for a diffusion coefficient ($Diff$) varying from 1 to 10 the scour depth increases rapidly, whereas for a variation of the diffusion coefficient from 10 to 100 the increase of the scour depth is slow (Figures 5.25-[a] and 5.25-[b]). The scour hole extent follows the same trend as above (Figure 5.25-[c]). This could mean that the proposed numerical model is sensitive to the diffusion coefficient value up to a certain point. Beyond this point the numerical model seems not to be affected by the diffusion coefficient. However, more thorough studies need to be done to confirm the above observation.

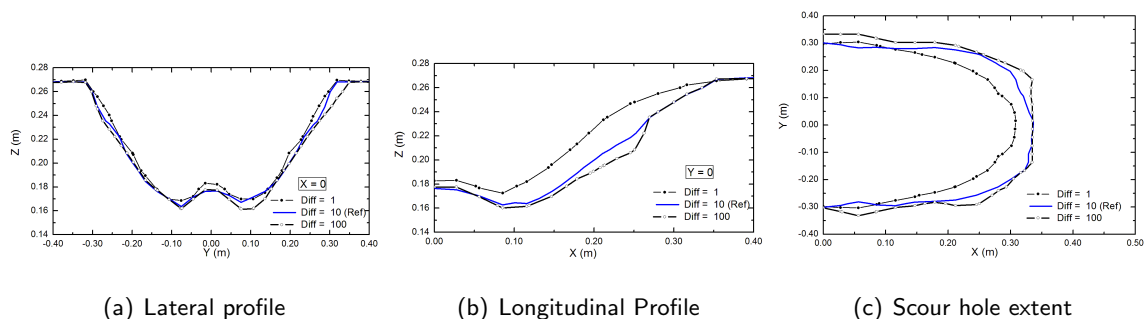


Figure 5.25: Results of sensitivity analysis for diffusion coefficient

5.5.3 Packing Ratio

Packing ratio is defined as ratio of the packed bed density to the particle density. It gives an indication of the compaction of the bed. Figure 5.26 depicts the results of the sensitivity analysis of the packing ratio. Figures 5.26-(a) and 5.26-(b) show that the maximum depth for the simulation occurred at the smallest packing ratio (PR) value. The length of the scour hole increases with a decrease in packing ratio value (Figure 5.26-[c]).

Furthermore, in the simulation with the smallest packing ratio the scour hole profile is not smooth as shown in Figures 5.26-(b) and 5.26-(c). This means that the present numerical model is sensitive to the value of packing ratio (PR) because for a small packing ratio, which is equivalent to a small bed density, the surface of the packed bed becomes more unstable causing an irregular shape of the scour hole.

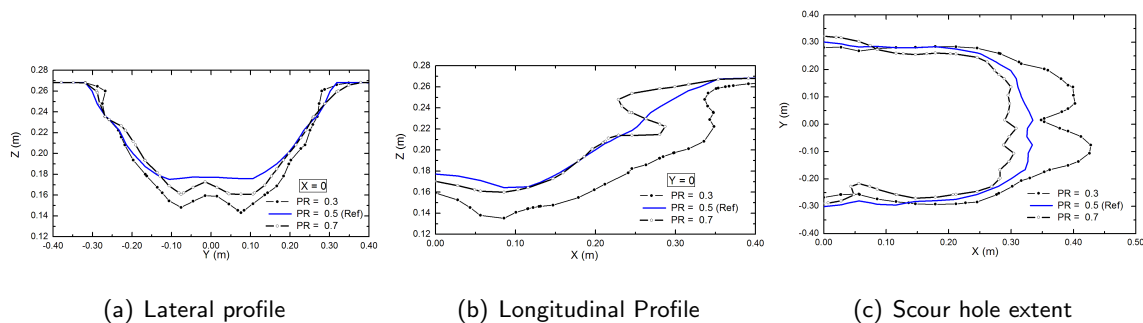


Figure 5.26: Results of sensitivity analysis for packing ratio parameter

5.5.4 Sediment Size

The sensitivity of the numerical model in terms of sediment size is presented in Figure 5.27. The results show that the scour depth increases with the decrease in the sediment size. The extent of the scour hole follows the same trend; that is, the edge of the scour hole is wider for a small sediment size as shown in Figure 5.27-(a). This was expected because particles with small size, and probably with light weight, are more likely to be entrained by the water flow. Sediment size, therefore, is considered as a sensitive parameter for the present numerical model.

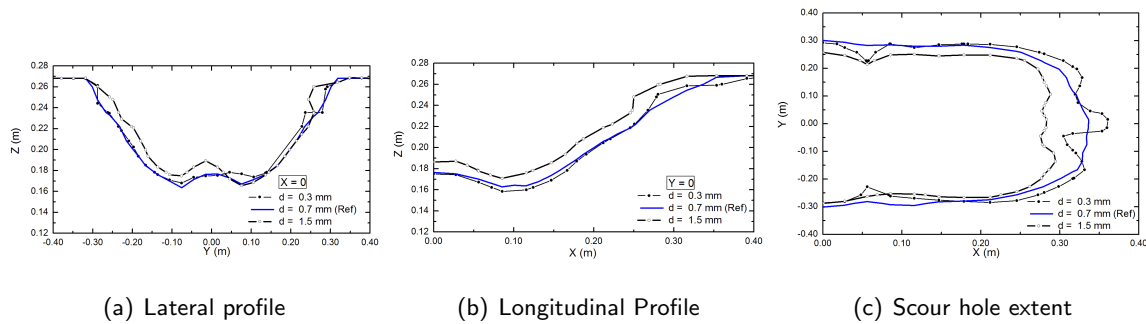


Figure 5.27: Results of sensitivity analysis for sediment size

5.5.5 Sediment Roughness

The sensitivity of the numerical model in terms of sediment roughness is presented in Figure 5.28. Apart from some instability observed on the extent of the scour hole shown in Figure 5.28-(a), the lateral and the longitudinal scour hole profile are similar to the three simulated sediment roughness values. Therefore, it is concluded that the sediment roughness is not a sensitive parameter for the present numerical model. The sediment roughness should have the same order of magnitude with the sediment size.

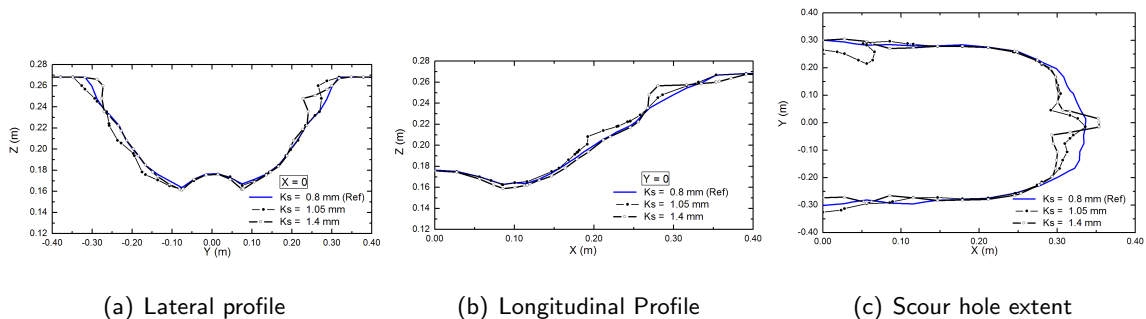


Figure 5.28: Results of sensitivity analysis for sediment roughness

5.5.6 Sediment Density

The sensitivity of the numerical model in terms of sediment density (SD) is presented in Figure 5.29. The results clearly show that the maximum scour depth increases with the decrease in the sediment density. Simulation with high sediment density value was expected to scour deeper. However, the scour hole is unstable at a small value of the sediment density, showing an irregular scour hole profile (5.29). The sediment density is, therefore, a sensitive parameter in the present numerical model.

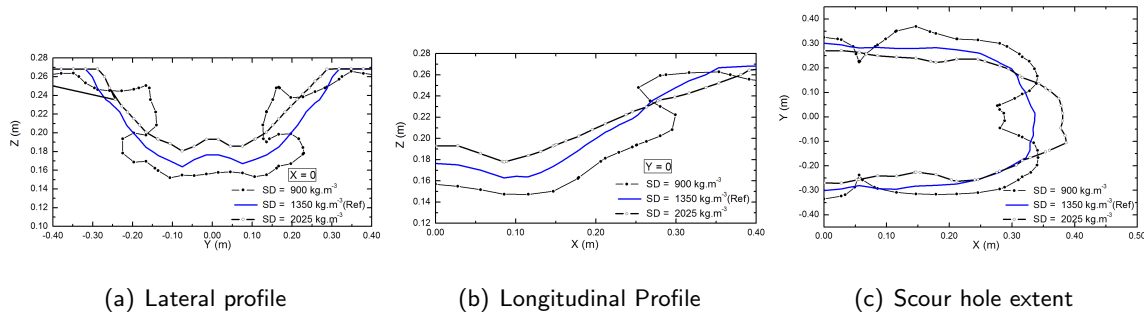


Figure 5.29: Results of sensitivity analysis for sediment density

5.5.7 Mesh Size

Three different mesh sizes were simulated in order to analyse the sensitivity of the choice of the mesh size in the numerical model. Figure 5.30 shows the comparison of simulated results for three mesh sizes. Two different mesh sizes relative to the mesh size in Test 1 were simulated. A finer mesh which was $2/3$ times the reference mesh (Test 1) and a coarser mesh which was 2 times the reference mesh were evaluated. The results for the different mesh size simulations show that the deeper scour hole is observed for simulation with the finer mesh. The results from the same mesh size present a narrow lateral scour cross section (Figure 5.30-[a]). In addition, the scour hole becomes unstable for a small mesh size. Figure 5.30-(c) shows that the mesh size increases with the decrease of the scour length. The large differences between the three simulated mesh sizes clearly show that the mesh size is a very sensitive parameter for the proposed numerical model. Therefore, the choice of the mesh size is very crucial because a coarser mesh can lead to an underestimation of the scour depth and scour length, and an overestimation of the scour width. On the contrary, a finer mesh could result in instability at the surface of the bed causing an irregular shape of the scour hole.

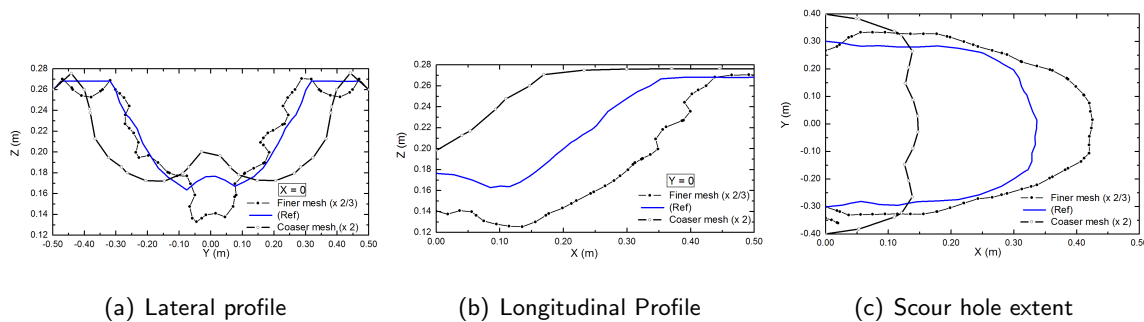


Figure 5.30: Results of sensitivity analysis for mesh sensitivity

5.6 Summary

A coupled and fully three-dimensional numerical model as presented in Chapter 4, was used to simulate the bottom outlet flushing of non-cohesive sediment. The first part of the present chapter consisted of the numerical model setup and model technique and procedure. In the second part, the experimental tests were simulated by the proposed numerical model. The coupled fully three-dimensional model presented in this study successfully predicted the laboratory tests and therefore it was validated against the measurements in terms of sediment transport and velocity fields. It is worth noting that even though the proposed numerical model simulated the bottom outlet sediment flushing which is mainly dominated by erosion processes, both sediment erosion and deposition were considered in the coupled fully three-dimensional numerical model as discussed during the numerical model development in Chapter 4. In the last part of the chapter, the sensitivity analysis was conducted on the numerical parameters. This analysis shows that creeping parameter, the diffusion coefficient, the packing ratio, the sediment size, the sediment density and the mesh size are sensitive parameters for the proposed numerical model. Amongst the sensitive parameters, the mesh size was the most sensitive parameter.

6. Three-Dimensional Suspended Sediment Transport Model Development

6.1 Introduction

Turbulent suspended sediment transport is the dominant mechanism of sediment transport through most reservoirs. One of key objective of this study was the development of a coupled fully 3D numerical model based on Navier-Stokes equations which include both sediment transport and hydrodynamic parameters. With the aid of a finite volume procedure the coupled fully 3D numerical model aims to determine a detailed spatial and temporal pattern of the sediment concentration and also the sediment deposition and erosion in the reservoir.

The hydrodynamic model composed of continuity and momentum equations, turbulence model and the sediment transport model is presented in the next sections. Boundary conditions prescribed in both hydrodynamic and sediment transport model are also described in the following sections.

6.2 Hydrodynamic Modelling

The flow field was obtained by solving the Reynolds-averaged Navier-Stokes equations in a three-dimensional coordinate system. The k - ε model was used for turbulence modelling.

6.2.1 Continuity and Momentum Equations

For an incompressible fluid flow, continuity and momentum equations are given as:

$$\frac{\partial U_i}{\partial x_i} = 0 \quad (6.1a)$$

$$\frac{\partial U_i}{\partial t} + U_j \frac{\partial U_i}{\partial x_j} = \frac{1}{\rho} \frac{\partial}{\partial x_j} \left[- \left(P + \frac{2}{3}k \right) \delta_{ij} + \nu_T \left(\frac{\partial U_i}{\partial x_j} + \frac{\partial U_j}{\partial x_i} \right) \right] \quad (6.1b)$$

where ρ is fluid density, U_j is the component of local time-averaged flow velocities, P is the dynamic pressure, k is the turbulent kinematic energy, δ_{ij} is the Kronecker delta and ν_T is the eddy viscosity.

Since relatively low sediment concentrations were considered in this study, the flow was treated as single phase and buoyancy effects are neglected.

6.2.2 Turbulence Model

The turbulence model used, in the present 3D numerical model, is the standard k - ε model. In this turbulence model, the local state of turbulence is described by two parameters; the turbulent kinematic energy (k) and the rate of its dissipation (ε) which are both related to eddy viscosity by

$$\nu_T = C_\mu \frac{k}{\varepsilon^2} \quad (6.2)$$

where C_μ is a constant value of 0.09 in the standard model. The distribution of (k) and (ε) are determined from the following model transport equations:

$$\frac{\partial k}{\partial t} + U_j \frac{\partial k}{\partial x_j} = \frac{\partial}{\partial x_j} \left(\frac{\nu_T}{\sigma_k} \frac{\partial k}{\partial x_j} \right) + P_k - \varepsilon \quad (6.3a)$$

$$\frac{\partial \varepsilon}{\partial t} + U_j \frac{\partial \varepsilon}{\partial x_j} = \frac{\partial}{\partial x_j} \left(\frac{\nu_T}{\sigma_\varepsilon} \frac{\partial \varepsilon}{\partial x_j} \right) + C_{\varepsilon 1} \frac{\varepsilon}{k} P_k + C_{\varepsilon 2} \frac{\varepsilon}{k} \varepsilon \quad (6.3b)$$

where P_k known as the production of turbulent kinematic energy, is given by

$$P_k = \nu_T \frac{\partial U_j}{\partial x_i} \left(\frac{\partial U_i}{\partial x_j} + \frac{\partial U_j}{\partial x_i} \right) \quad (6.4)$$

and $C_{\varepsilon 1}$, $C_{\varepsilon 2}$, σ_k and σ_ε are empirical constants.

6.2.3 Boundary Conditions

Five types of boundaries were defined; inlet-velocity, outlet-pressure, bed (wall), flume walls (wall) and water surface (symmetry). In the present suspended sediment transport numerical model, the velocity profile and the concentration profile from the experiment data were prescribed in the inlet boundary according to the different simulated cases and presented in Chapter 7. At the water surface, the symmetry condition was applied that includes zero gradients and zero fluxes perpendicular to the boundary. At the flume walls, a wall boundary condition was applied and parameters were set as defaults. At the bed, wall boundary condition was also applied with the standard wall-function approach.

6.3 Transport Model

The suspended sediment concentration was determined by solving the convection-diffusion equation, in which the particle settling velocity was introduced.

6.3.1 Convection-Diffusion Equation

A convection-diffusion equation was used as a transport model for suspended sediment concentration. It was formulated as follows:

$$\frac{\partial C}{\partial t} + U_j \frac{\partial C}{\partial x_j} + \omega_s \frac{\partial C}{\partial z} = \frac{\partial}{\partial x_j} \left(\frac{\nu_T}{\sigma_c} \frac{\partial C}{\partial x_j} \right) \quad (6.5)$$

where C is the sediment concentration, ω_s is the settling velocity of the particles and σ_c is the turbulent Schmidt number.

6.3.2 Boundary Conditions for Sediment Transport

A near-bed reference concentration or a sediment flux near the bed was needed for solving the above mentioned convection-diffusion equation. As proposed by Van Rijn (1984a, 1986), a widely used approach was to set the reference concentration C_b equal to its equilibrium value C_{bmax} . However the equilibrium-concentration assumption was valid only for loose beds with unlimited sediment supply, according to the same author.

The rate of entrainment e is equal to the rate of deposition d when sediment transport reaches its equilibrium condition. On the contrary, under nonequilibrium situations, the flow entrains as much sediment from the bed as long as there is sufficient sediment available on the bed. From this, Celik and Rodi (1988) developed the following entrainment model:

$$e = \omega_s C_{bmax} \quad (\text{for loose bed}) \quad (6.6a)$$

$$e = \min(\omega_s C_b, \omega_s C_{bmax}) \quad (\text{for fixe bed with an upstream sand source}) \quad (6.6b)$$

The same entrainment model approach was adopted in the present study.

For the net-deposition case, the net-deposition rate to the bed was defined in the model as:

$$d - e = a\omega_s C_b \quad (6.7)$$

where d is the deposition rate, e is the entrainment rate and a is defined as the settling probability that a particle reaching the bed is deposited there. This approach was used by Celik (1983) to predict the downstream development of concentration profiles of Jobson and Sayre (1970a,b) experiments. According to Celik and Rodi (1988), once the entrainment rate is known, the settling probability introduced in the above equation can be calculated as $a = 0$ for $C_b < C_{bmax}$ and $a = 1 - C_{bmax}/C_b$ for $C_b > C_{bmax}$. The same approach was followed, in the present study, to model the deposition process at the bed.

6.4 Model Solver: ANSYS FLUENT

In order to solve all these above mentioned equations, a computer code (programm) was needed. Therefore ANSYS FLUENT version 14 code was used in this study. The main reason for using ANSYS FLUENT was to avoid the time consuming necessity of developing a custom software code. As mentioned in Chapter 5, ANSYS FLUENT is a computer programm for fluid analysis in complex geometry using the finite volume method. It provides fast, accurate and robust CFD (computational fluid dynamics) solution. It is worth noting that ANSYS FLUENT is not specifically a sediment transport model. However, unlike other computer programs, ANSYS FLUENT allows users to customise for example materials properties and boundary conditions through its User-Defined Function (UDF). This special tool was extensively used in this study in order to define the sediment transport equation and also the different sediment boundary conditions at the bed.

6.5 Summary

A coupled fully 3D numerical model for turbulent suspended sediment transport was developed in this chapter. The two main components of this numerical models were; the hydrodynamic modelling based on Navier-Stokes equations in conjunction with $k-\varepsilon$ turbulence model. The second part consisted of computing the suspended sediment concentration using the convection-diffusion equation. Furthermore, boundary conditions for sediment transport were modelled using formulas that link both the rate of entrainment and deposition with the settling velocity and the reference concentration. In the next Chapter, the proposed turbulent suspended numerical model is validated against experimental data.

7. Three-Dimensional Suspended Sediment Transport Model Testing and Validation

7.1 Overview on Experimental Cases Simulated by the Model

The present coupled fully three-dimensional numerical model was tested with a wide range of laboratory flume set of data from the study done by Jobson and Sayre (1970a). The main purpose of these experimental tests, according to Jobson and Sayre (1970a) was to measure the turbulent mass transfer coefficients for dye and sediment particles of varied grain size distribution and also the fall velocities of the sand particles in open channel and steady flow. These laboratory experiments utilised a recirculating flume of 2.44 *m* wide by 1.22 *m* deep by 60.96 *m* long. The water depth was held constant at 0.41 *m*.

In order to test the model under various experimental conditions, laboratory flume data from work done by Van Rijn (1981a), and Ashida and Okabe (1982) were also used. Van Rijn (1981a) conducted a net-entrainment experiment in which velocity and concentration measurement were taken under uniform flow conditions without initial sediment load and with a movable bed (fixed to loose). Therefore, sediment load was only supplied from the erosion of the bed. Ashida and Okabe (1982) conducted two experiments namely, a net entrainment and the net deposition case. In the net entrainment experiment, a fixed bed was used and covered with a mixture of gravel and sand in order to avoid scour at the beginning of the experimental test. As for the net-deposition experiment, sand with a diameter of 0.165 *mm* was discharged in the flow and the sediment was distributed over the whole depth of the channel.

These sets of data were found to be suitable for the validation of the model. Furthermore, the work of these authors has been widely used in other research studies such as those conducted by Celik and Rodi (1988) and Campos (2001). It is worth noting that all the laboratory flume dimensions are the same as those used in the numerical model. More experimental data used in this study are compiled in Table 7.1, where h is the water depth, U_m is the mean velocity, U_* is the shear velocity, K_s is the average roughness size, ρ_s is the sediment density and d_m is the mean sediment diameter.

Table 7.1: Experimental measurements

Experiment (Reference)	h (<i>m</i>)	U_m (<i>m/s</i>)	U_* (<i>m/s</i>)	K_s (<i>m</i>)	ρ_s (<i>kg/m</i> ³)	d_m (<i>mm</i>)	ω_s (<i>m/s</i>)	C_{bmax} (<i>mg/l</i>)
Dye-mixing (Jobson and Sayre (1970a))	0.41	0.32	0.03	0.08	-	-	0.00	-
Zero net flux (Jobson and Sayre (1970a))	0.40	1.00	0.10	0.10	2420	0.12	0.01	-
Net deposition (Jobson and Sayre (1970a))	0.41	0.60	0.06	0.10	2650	0.12	0.01	192
Net entrainment (Van Rijn (1981a))	0.25	0.47	0.03	0.01	2650	0.23	0.03	2000
Net deposition (Ashida and Okabe (1982))	0.04	0.37	0.04	0.01	2650	0.17	0.02	295

7.2 Numerical Solution Procedure

A finite-volume method is used for solving the Navier-Stokes equations in this study. These equations are discretised on a three-dimensional grid with $610 \times 12 \times 16$ in the longitudinal, transversal and vertical directions with total number of cells of 117120. Figure 7.1 shows the geometry and the grid used in the simulation.

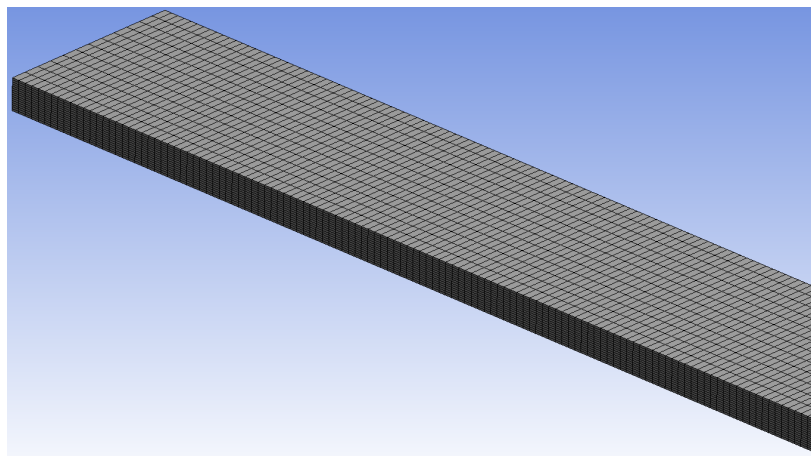


Figure 7.1: Zoomed view of simulated geometry and grid cells

The simulation of the experimental cases consisted of discharging dye as well as various types of sediment particles continuously from a line source located near the water surface into a fully developed channel flow. In some cases, only clear water was discharged over a sand bed leading to suspension of sediment. In most cases considered, the downstream development of the concentration is predicted after prescribing both velocity and concentration profile at the inflow boundary. These boundary conditions were provided by the experimental data. The velocity profile was computed using the von Karman log-law for rough walls:

$$\frac{V}{U_*} = 8.5 + 2.5 \ln \left(\frac{Z}{K_s} \right) \quad (7.1)$$

where V is the velocity, U_* is the shear velocity, Z is the depth and K_s is the average roughness size.

7.3 Dye-Mixing Simulation

In order to determine the value of the turbulent Schmidt number (σ_c) for very fine sediment, Jobson and Sayre (1970a) discharged dye instead of sediment particle. The turbulent Schmidt number is defined as the ratio of momentum turbulent transfer coefficient and sediment mass transfer coefficient. For their experiment, Jobson and Sayre (1970a) found a value of 1.0 as turbulent Schmidt number. Further studies done by Karim (1981) and Celik (1983), have shown that values of σ_c can range from 0.5 to 1.0. According to Celik and Rodi (1988), a value of $\sigma_c = 0.5$ yields better agreement between calculated and measured concentration profile. Therefore this value was used in the present numerical model. Boundary conditions for dye-mixing simulation were defined as follows:

- The measured profile of the dye concentration was used at the inlet as the initial condition.
- The observed flow velocity profile was set at the inlet as the initial condition.
- A zero dye concentration flux was prescribed at the bed.

The settling velocity (ω_s) of the dye, in this simulation, was assumed to be zero. Comparison of downstream development of the predicted dye concentration with measurements is given in Figure 7.2. Due to the available measurements only concentration profiles on the vertical centre plane in the flow direction were compared. The axes of the graphs represent the concentration and the vertical distance, and were made dimensionless with the initial discharge concentration (C_{ref}), and the water depth (h) respectively.

Although the model predicted too much mixing near the free surface, the dye concentration development further downstream is better predicted. As observed in the experimental case, a uniform dye concentration was reached at about $x/h = 24$. The overall prediction of the downstream development of the dye concentration by the present 3D numerical model was in good agreement with the measurements from the experimental case conducted by Jobson and Sayre (1970a).

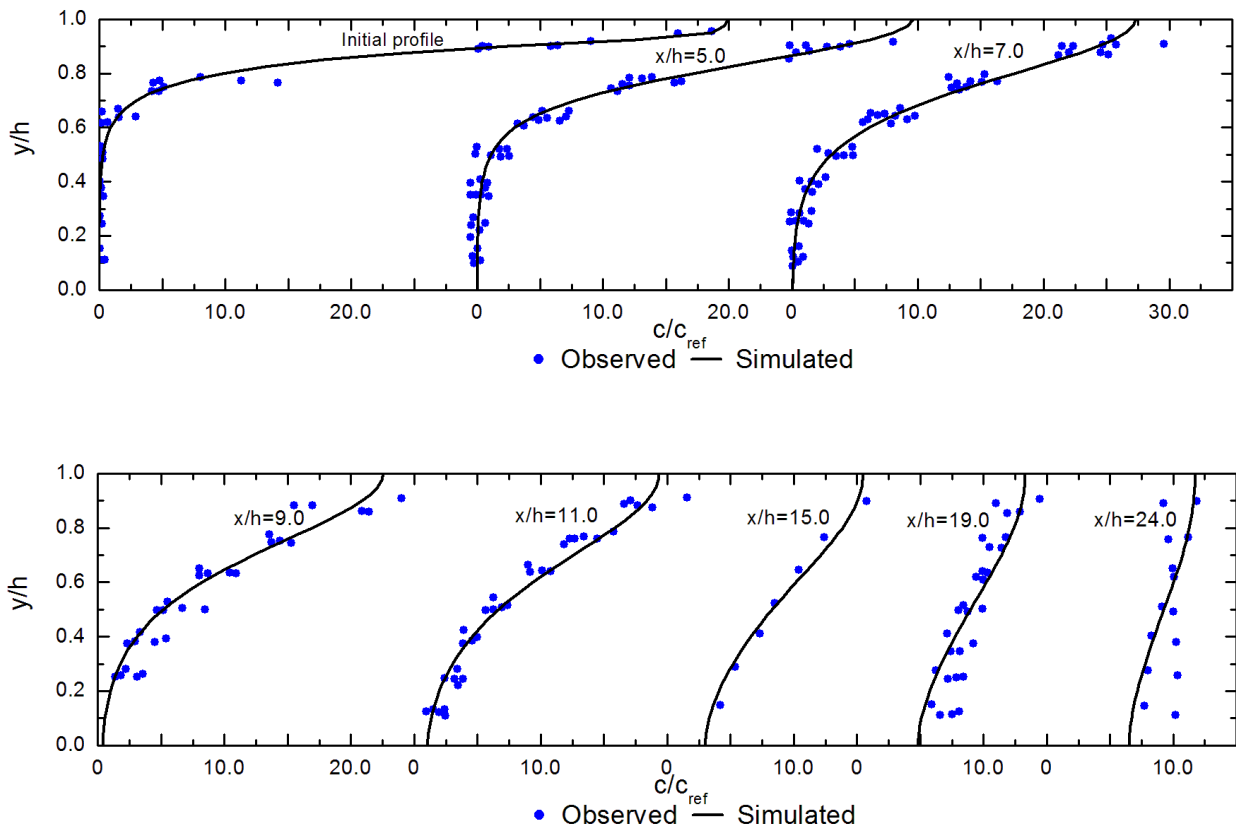


Figure 7.2: Comparison of simulated dye-concentration profiles with experimental data

7.4 Sediment Transport Simulation with Known Net Flux at the Bed

7.4.1 Zero Net Flux at the Bed

In this simulation, the dye was replaced by fine sediment with 0.123 mm of diameter. By prescribing a lower discharged suspended sediment load than the full transport capacity, all the sediment reaching the bed were re-entrained into the flow at the same deposition rate. As a result, a zero sediment flux was set at the bed. Comparisons of the predicted and the measured downstream development of the

concentration profiles are given in Figure 7.3. It can be seen that, the predicted concentration profiles yield a reasonable agreement with the observed data from the experimental case, especially in terms of concentration profile shape.

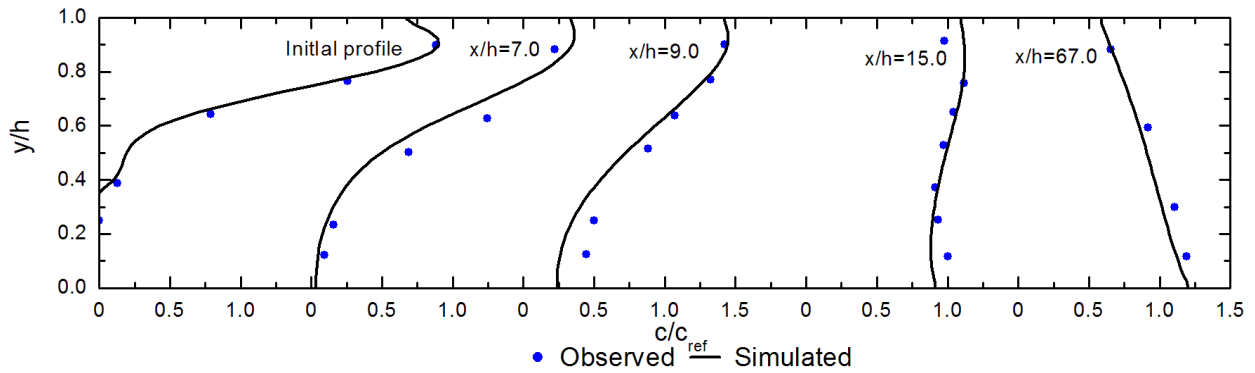


Figure 7.3: Comparison of simulated concentration profiles with experimental data for zero net flux at the bed

7.4.2 Net Deposition to a Fixed Bed

For this simulation, fine sediment (sand) with 0.123 mm of diameter was discharged into the flow with relatively high velocity. However, the velocity was not high enough to transport all the discharged sediment so that net deposition occurred until the suspended load reached the carrying capacity. Furthermore, equilibrium state was reached at the far downstream station from the sand source. Comparisons of the predicted concentration profiles with the measured ones, depicted in Figure 7.4, indicate that both the simulated shape of the profiles and the calculated concentration values are quite similar to those observed during the laboratory experimental case.

Figures 7.5 and 7.6 show the stream wise variation of the suspended load Q_s and the near-bed concentration C_b . Just like in the experiments done by Jobson and Sayre (1970a), the 3D numerical model predicted accurately both the initial increase of the near-bed concentration and the overshooting of the asymptotic equilibrium value. As a result, the model was realistically capable of predicting both the deposition and entrainment processes.

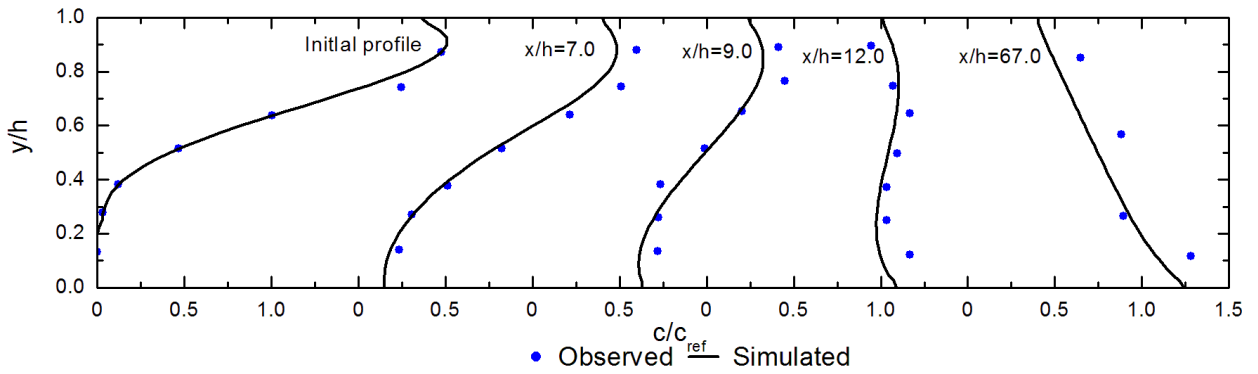


Figure 7.4: Comparison of simulated concentration profiles with experimental data for net deposition to a fixed bed

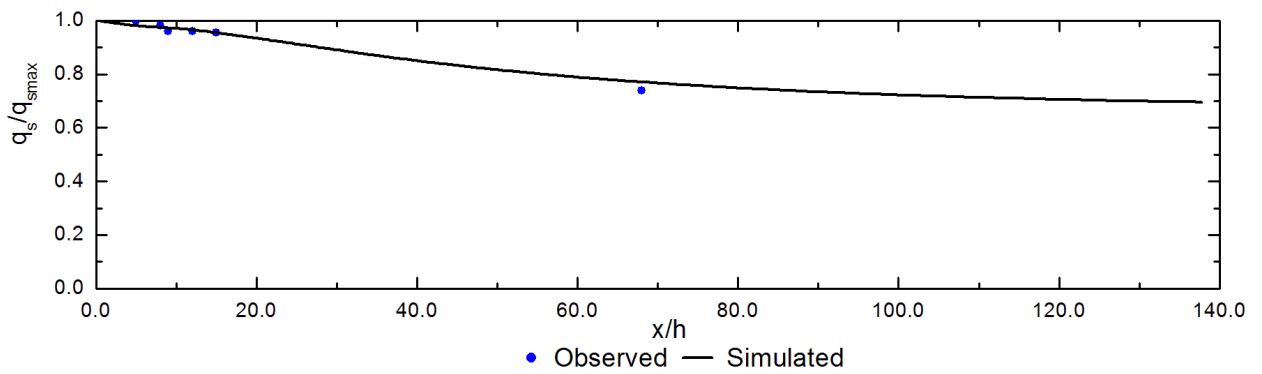


Figure 7.5: Downstream development of suspended load in net deposition case

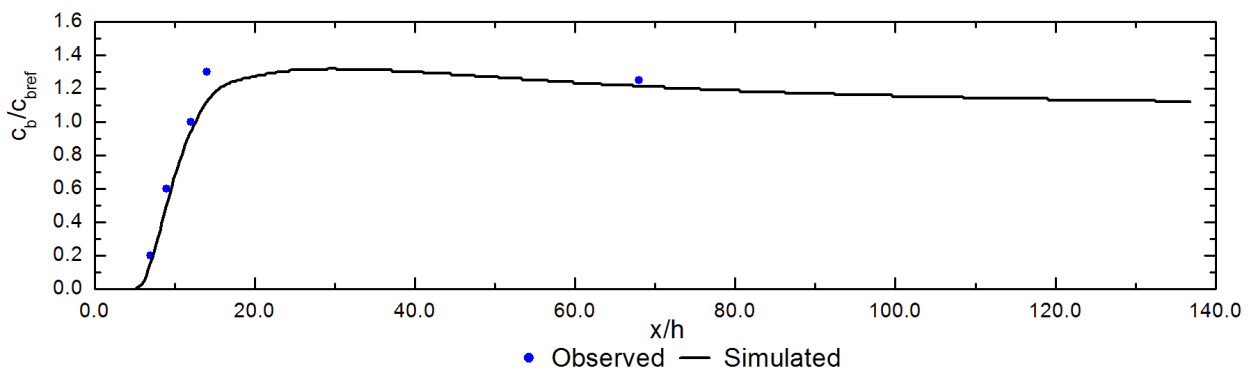


Figure 7.6: Downstream development of near-bed concentration in net deposition case

7.5 Sediment Transport Simulation with Net Entrainment and Net Deposition Model

7.5.1 Net Entrainment from a Loose Bed

This case simulated Van Rijn's (1981a) laboratory experiments in which initially clear water was discharged over a sand bed leading to the suspension of sediment until the full transport capacity was reached. It can be seen in Figure 7.7 that at the beginning of the loose bed the model over predicted both the entrainment and the near bed concentration. Celik and Rodi's (1988) model yielded a similar result and according to them, this could be due to the use of flat bed in the model while in the experimental case a scour hole developed downstream of the beginning of the loose bed. Overall, the development of the concentration profile was simulated fairly well by the 3D numerical model.

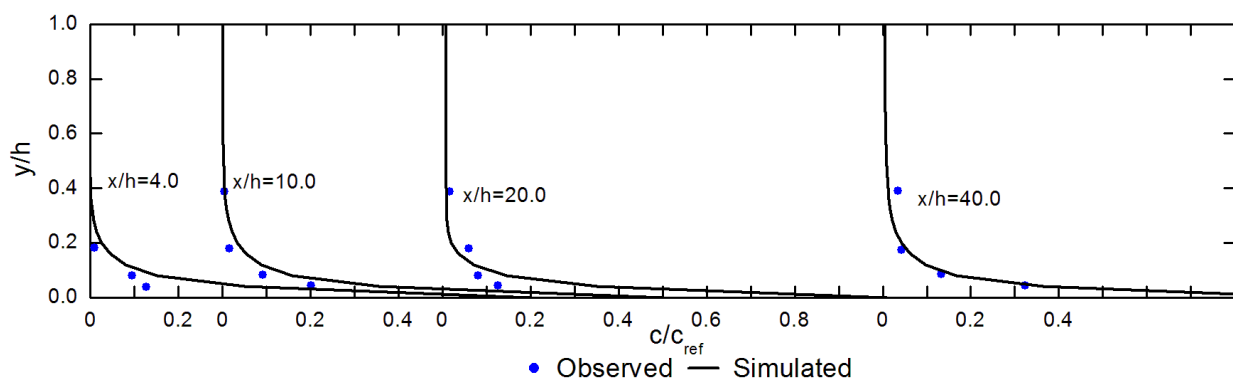


Figure 7.7: Comparison of simulated sediment concentration profiles with experiment data in case of net entrainment from a loose sand bed

7.5.2 Net Entrainment on a Fixed Bed

This case deals with the simulation of experiments done by Ashida and Okabe (1982) in which a section of the upstream bottom part of the channel was made of loose bed (sand source) while in the remaining part, a fixed bed was prescribed. The calculated results of the concentration profiles for this case are compared with the measured ones in Figure 7.8. The 3D numerical model over predicted the entrainment near the beginning of the sand source and further downstream, the model over predicted concentrations at the surface while the near bed concentration was under predicted. These differences between the data

and the predictions could be due to the use of a fixed value for roughness characteristics, which tends to vary as sand erosion occurs during the experimental test. However, from the predicted results of concentration profiles, the 3D numerical model proposed in this study, showed its ability to realistically simulate the net-entrainment process.

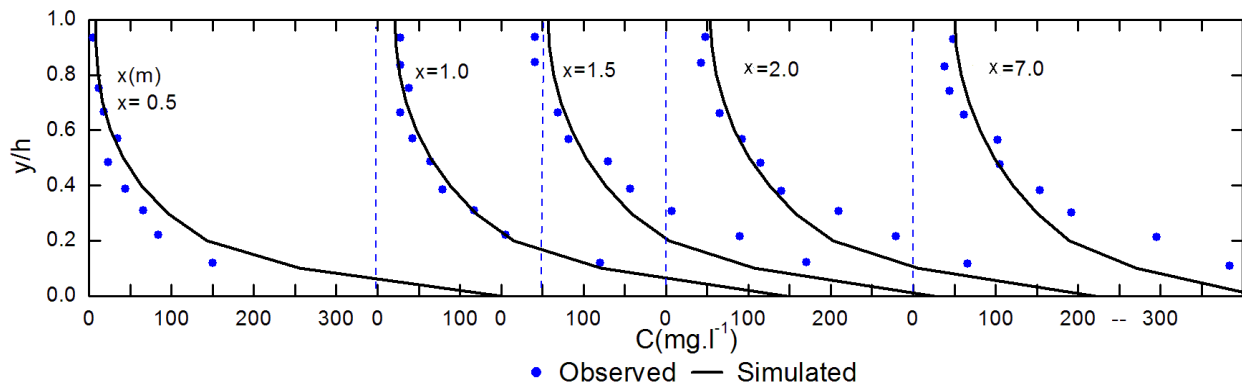


Figure 7.8: Comparison of simulated sediment concentration profiles with experiment data in case of net entrainment on a fixed bed

7.5.3 Net Deposition on a Fixed Bed

During the experimental tests of this case done by Ashida and Okabe (1982), a vertical sand concentration profile at the upstream end of the flume and a fixed bed at the downstream end of the flume were prescribed. Comparisons of the predicted and the measured downstream development of the sediment concentration profiles for this case are given in Figure 7.9. As seen in Figure 7.9, concentration profiles were predicted fairly well in terms of the shape and the sediment concentrations.

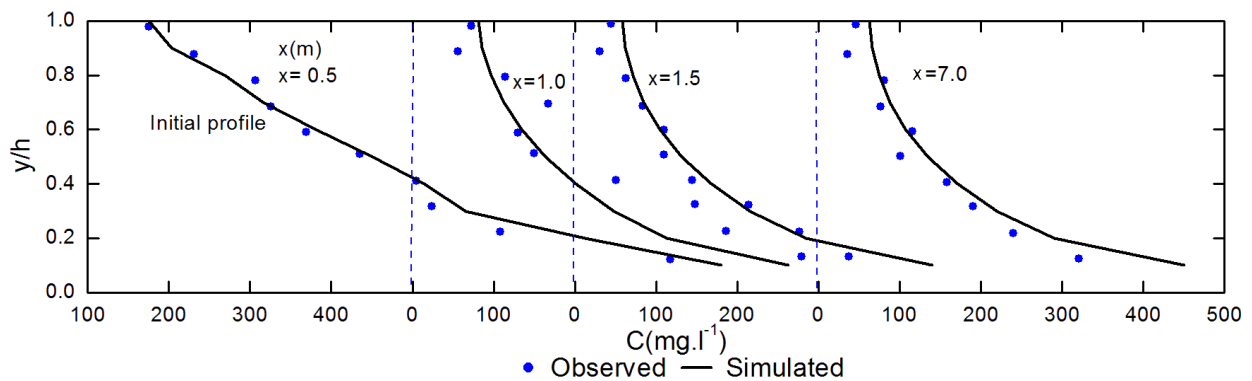


Figure 7.9: Comparison of simulated sediment concentration profiles with experiment data in case of net deposition on a fixed bed

7.6 Summary

This chapter presented a fully coupled 3D numerical model based on Navier-Stokes equations in conjunction with a turbulent model and the convection-diffusion equation for the suspended sediment transport. To validate this numerical model, a range of experimental cases conducted in a laboratory flume, were simulated. These experimental cases can be divided into two groups. The first experiments involved discharging a dye as well as various types of sediment particles continuously from a line source located near the water surface into a fully developed channel flow. While the second group of experiments consisted of discharging clear water under uniform flow conditions, over movable bed causing erosion followed by the suspension of sediment. Subsequently in both cases, the downstream development of the suspended sediment concentration profiles and flow conditions were determined. These laboratory sets of data were compared with results from CFD simulations that were carried out under the same experimental conditions. The overall predictions of the downstream development of the suspended sediment concentration by the present 3D numerical model were in good agreement with the measurements. Both the shape and the sediment concentrations profiles were predicted reasonably well. Consequently, the model was also capable of predicting both the deposition and entrainment processes. Note that the present suspended sediment transport 3D numerical model was validated against 2D laboratory tests because they were the only available experimental data on suspended sediment transport. The bottom outlet sediment flushing simulations have, however, shown that the present numerical model can simulate a 3D sediment flushing conditions. As a result, the proposed 3D numerical model in this study can be used to predict turbulent suspended sediment transport processes in reservoirs.

8. Conclusions and Recommendations

The investigation of reservoir sedimentation has become an important and valuable research topic in engineering practice. Sediment deposition in reservoirs can affect flood levels, drainage for agriculture land, pumpstation and hydropower operation and navigation.

An extensive review of the technical literature pertaining to suspended sediment transports as well as deposited sediment flushing from reservoir under hydraulic condition has shown that most studies on sediment are still based on empirical formulas and experimental work, despite the availability of sophisticated computers. This is because sediment transport, particularly sediment deposition and erosion are complex processes, that involve the interaction of many physical factors which are not easily modelled numerically. In addition, most of the existing three-dimensional numerical models are not coupled hydrodynamic and sediment transport models. They simulate first, the velocity field and water depth and thereafter concentration and bed change are calculated. Furthermore, they are not fully three-dimensional models for using a layer-averaged approach in conjunction with Saint-Venant equations.

The key objective of the present research was to develop a coupled fully 3D numerical model based on Navier-Stokes equations which include both sediment transport component and hydrodynamic parameters. In this regard, a physical model was set up in the laboratory flume in order to investigate the bottom outlet flushing in a controlled environment. The proposed 3D numerical model was calibrated against experimental data, then executed and the simulation results were satisfactory.

Note that the 3D numerical model which has been developed in this study is able to simulate both sediment erosion and deposition at the same time. However, the validation of this numerical model was done separately for deposition and erosion processes. Measurements from experimental investigation conducted in this research were mainly used to validate the proposed numerical model in terms of sediment erosion, while data from laboratory flume study found in literature were used for the validation of sediment deposition and entrainment component of the numerical model. The later validation was based on suspended sediment transport and did not include bed change simulation.

8.1 Physical Modelling of the Bottom Outlet Flushing under Pressure

Laboratory tests were carried out in the present study to investigate scour processes upstream of the bottom outlet. The physical model was set up in a rectangular flume in which sediment from crushed peach pips was packed in the way that the bed surface was levelled with the invert of the bottom outlet. Three different flow rates were tested, namely, $0.036 \text{ m}^3/\text{s}$, $0.021 \text{ m}^3/\text{s}$ and $0.012 \text{ m}^3/\text{s}$. The results showed that the shape of the scour hole was directly dependent on the discharge at the bottom outlet. The scour depth, the scour width as well as its length increase as the flow rate increases.

8.2 Coupled and Fully 3D Numerical Modelling of the Bottom Outlet Flushing under Pressure

The fluid dynamics were modelled in this study using the Navier-Stokes equations in conjunction with $k-\varepsilon$ turbulence model. The sediment erosion and deposition were modelled by considering the following mechanisms of sediment transport; particle rolling due to the hydrodynamic shearing, particle rebound after impact, particle entrainment due to shear stresses, particle erosion due to impacting particles, particle deposition and accumulation, and landslide shearing mode of transport. Finally, an immersed boundary method was used to model the surface deformation of a packed bed. It is worth noting that the standard ANSYS FLUENT code was used to solve flow and turbulent model equations. In contrast, the sediment transport component and the modelling of the deformation of the packed bed's surface were executed using the User Defined Functions (UDF), a special feature of ANSYS FLUENT which allows the user to define his own functions or code as well as to specify customised model parameters.

The proposed coupled and fully 3D numerical model was used to simulate the experimental tests. Results from these simulations were in good agreement with the measurements. The geometric features of the scour hole upstream of the bottom outlet were reasonably well predicted compared to the experimental data. Furthermore, the velocity field upstream of the bottom outlet was in good agreement with measurements. The proposed numerical model for bottom outlet flushing was, therefore, validated because of its ability to accurately predict the temporal and spatial scour hole development during flushing process. The proposed numerical model can be considered reliable provided that the model is correctly calibrated and set up to reflect the condition of a particular case study. The sensitivity to certain simulation parameters such as mesh size, diffusion coefficient and packing ratio should be

considered in the proposed numerical modelling.

8.3 Coupled and Fully 3D Numerical Modelling of Suspended Sediment Transport

In this study, the suspended sediment transport was modelled using the convection-diffusion equation. The hydrodynamic and turbulence model equations in the present suspended sediment transport model were solved using the standard ANSYS FLUENT code whereas the convection-diffusion equation and boundary conditions for sediment transport equations were solve through the User Defined Function (UDF).

A range of experimental cases found in the literature and conducted in a laboratory flume, were simulated for model validation. The overall predictions of the downstream development of the suspended sediment concentration by the present coupled and fully 3D numerical model were in good agreement with the laboratory test results. Both the shape and the sediment concentration profiles were predicted reasonably well. Furthermore, the proposed numerical suspended sediment transport model was capable of predicting both the deposition and entrainment processes. As a result, the proposed numerical model can be used to predict turbulent suspended sediment transport processes in reservoirs.

8.4 Recommendations for Further Research

The coupled and fully 3D numerical models discussed in this study, with sufficient resources can be improved in several ways as follows:

- The present experimental setup can be improved by including the use of Acoustic Doppler Velocimeter (ADV), which is useful in providing a 3D flow velocity data to be used for the verification of the 3D numerical modelling of the bottom outlet flushing.
- The bottom outlet numerical model could be modified so that it is able to simulate more than one sediment fraction size as well as a cohesive sediment case.
- The bottom outlet flushing numerical model can be altered in order to simulate the case of packed bed levelled above the invert of the bottom outlet.

-
- In order to fully capture the effect of the turbulence upstream of the bottom outlet, a more robust turbulence model could be used such as; Detached Eddy Simulation (DES) model, a scale resolving large eddy model and a Reynolds stress model.
 - Finally the coupled and fully 3D numerical model for bottom outlet flushing, developed in this study, can serve as a framework for investigation of local scour that could occur at hydraulic structures such as bridge piers and abutments. It could also be used for the validation of sediment transport models in case of a 3D reservoir sedimentation as well as a laboratory flume 3D data.

References

- Ackers, P. and White, W. R. 1973. Sediment Transport: New Approach and Analysis. *Journal of Hydraulics Division, ASCE*, 99(11):2041–2160.
- Alfrink, B. J. and Van Rijn, L. C. 1983. Two-equation Turbulence Model for Flow in Trenches. *Journal of Hydraulic Engineering*, 109:941–958.
- Anderson, R. and Haff, P. 1991. Wind Modification and Bed Response During Saltation of Sand in Air. In *Aeolian Grain Transport 1*, pages 21–51. Springer.
- Andreotti, B. 2004. A Two-Species Model of Aeolian Sand Transport. *Journal of Fluid Mechanics*, 510:47–70.
- Andreotti, B., Claudin, P., and Douady, S. 2002. Selection of Dune Shapes and Velocities Part 1: Dynamics of Sand, Wind and Barchans. *The European Physical Journal B-Condensed Matter and Complex Systems*, 28(3):321–339.
- Ashida, K. and Okabe, T. 1982. On Calculation Method of the Concentration of Suspended Sediment under Non- equilibrium Condition. In *26th Conference on Hydraulics, JSCE*, pages 153–158.
- Bagnold, R. A. 1966. An Approach to the Sediment Transport Problem from General Physics. *U.S Geological Survey Professional Paper*, 422(1).
- Basson, G. R. and Rooseboom, A. 1997. Dealing with Reservoir Sedimentation. Technical Report TT 91/97, Water Research Commission.
- Basson, G. R. and Rooseboom, A. 1999. Dealing with Reservoir Sedimentation: Guidelines and Case Studies. Bulletin 60, ICOLD.
- Basson, G. R. and Rooseboom, A. 2008. Mathematical Modelling of Sediment Transport and Deposition in Reservoirs. Bulletin, ICOLD.
- Bouvard, M. 1992. *Mobile Barrages and Intakes on Sediment Transporting Rivers*. Balkema, Rotterdam.
- Bryant, D. B., Khan, A. A., and Aziz, N. M. 2008. Investigation of Flow Upstream of Orifices. *Journal of Hydraulic Engineering*, 134(1):98–104.
- Campos, R. 2001. *Three-Dimensional Reservoir Sedimentation Model*. PhD thesis, Departement of Civil Engineering, University of NewCastle.

- Celik, I. 1983. Numerical Modelling of Sediment Transport in open Channel Reservoir. *Mechanics of Sediment Transport*, Sumer, B. M. and Muller, A., eds. A. A. Balkema Publishers, Rotterdam, The Netherlands,, pages 173–181.
- Celik, I. and Rodi, W. 1988. Modeling Suspended Sediment Transport in Nonequilibrium Situations. *Journal of Hydraulic Engineering*, 114(10):1157–1191.
- Cheng, N. S. 1997. Simplified settling velocity formula for sediment particle. *Journal of Hydraulic Engineering, ASCE*, 123(2):149–152.
- Chepil, W. S. 1959. Equilibrium of Soil Grains at the Threshold of Movement by Wind. *Soil Science Society of America Proceedings*, 23(6):422–428.
- Delft 1992. *The Control of Reservoir Sedimentation – A Literature Review*. Ministry of Development Co-operation, Government of the Netherlands, Delft Hydraulics.
- Delft 1999. *Delft3D Users Manual*. Delft Hydraulics. The Netherlands.
- DHI 2003. *MIKE 21C River Hydrodynamics and Morphology, User Guide*. DHI Water & Environment.
- Dodaran, A. A., Park, S. K., Mardashti, A., and Noshadi, M. 2012. Investigation of Dimension Changes in Under Pressure Hydraulic Sediment Flushing Cavity of Storage Dams Under Effect of Localized Vibrations in Sediment Layers. *International Journal of Ocean System Engineering*, 2(2):71–81.
- Emamgholizadeh, S., Bina, M., Fathi-Moghadam, M., and Ghomeyshi, M. 2006. Investigation and Evaluation of the Pressure Flushing Through Storage Reservoir. *ARPJ Journal of Engineering and Applied Sciences*, 1(4):7–16.
- Engelund, F. and Hansen, E. 1972. A Monograph on Sediment Transport in Alluvial Streams. Teknisk Forlag, Technical Press, Copenhagen, Denmark.
- Fan, H. 1985. *Methods of Preserving Reservoir Capacity*. Methods of Computing Sedimentation in Lakes and Reservoirs., UNESCO, Paris. 65-164.
- Fang, H. and Wang, G. 2000. Three-Dimensional Mathematical Model of Suspended-Sediment Transport. *Journal of Hydraulic Engineering*, 126(8):578–592.
- Fluent 2011. 14.0 Theory Guide. ANSYS inc.

- Gauer, P. 1999. *Blowing and Drifting Snow in Alpine Terrain: a Physically-Based Numerical Model and Related Field Measurements*. PhD thesis, Diss. Techn. Wiss. ETH Zürich, Nr. 13053, 1999. Ref.: L. Kleiser; Korref.: D. Issler.
- Gauer, P. 2001. Numerical Modeling of Blowing and Drifting Snow in Alpine Terrain. *Journal of Glaciology*, 47(156):97–110.
- Gauer, P. and Issler, D. 2004. Possible Erosion Mechanisms in Snow Avalanches. *Annals of Glaciology*, 38(1):384–392.
- Gerber, G. 2008. *Experimental Measurement and Numerical Model of Velocity, Density and Turbulence Profiles of a Gravity Current*. PhD thesis, University of Stellenbosch.
- Graf, W. H. 1998. *Fluvial hydraulics: Flow and Transport Processes in Channels of Simple Geometry*. Wiley, Chichester.
- Graf, W. L. 1971. *Hydraulic of Sediment Transport*. McGraw-Hill, New York.
- Itakura, T. and Kishi, T. 1980. Open Channel Flow with Suspended Sediments. *American Society of Civil Engineers*, 106(HY8):1325–1343.
- Jacobsen, F. and Rasmussen, E. B. 1997. MIKE 3 MT: A Three-Dimensional Mud Transport Model. Technical Report DG-12, Commission of the European Communities.
- Jobson, H. E. and Sayre, W. W. 1970a. Predicting Concentration Profiles in Open Channels. *Journal of Hydraulic Engineering*, 96(HY10):1983–1996.
- Jobson, H. E. and Sayre, W. W. 1970b. Vertical Transfer in Open Channel flow. *Journal of Hydraulic Engineering, ASCE*, 96(HY3):703–724.
- Kantoush, S., Sumi, T., and Murasaki, M. 2012. Evaluation of Sediment Bypass Efficiency by Flow Field and Sediment Concentration Monitoring Techniques. *Journal of Japan Society of Civil Engineers, Serie B1 (Hydraulic Engineering)*, 67.
- Karim, M. F. 1981. *Computer-based Predictors for Sediment Discharge and Friction Factor of Alluvial Streams*. PhD thesis, University of Iowa, Iowa City, Iowa.
- Khadra, K., Angot, P., Parneix, S., and Caltagirone, J.-P. 2000. Fictitious Domain Approach for Numerical Modelling of Navier–Stokes Equations. *International journal for numerical methods in fluids*, 34(8):651–684.

- Lai, J. S. and Shen, H. W. 1996. Flushing Sediment through Reservoirs. *Journal of Hydrologic Research*, 34(2):237–255.
- Lauder, B. E. and Spalding, D. 1974. The Numerical Computation of Turbulent Flows. *Computer methods in applied mechanics and engineering*, 3(2):269–289.
- Lew, A. J., Buscaglia, G. C., and Carrica, P. M. 2001. A Note on the Numerical Treatment of the k-epsilon Turbulence Model. *International Journal of Computational Fluid Dynamics*, 14(3):201–209.
- Mahmood, K. 1987. Reservoir Sedimentation: Impact, Extent and Mitigation. Technical Report 71, World Bank, The World Bank, Washington D.C.
- Meshkati, M. E., Dehghani, A. A., Naser, G., Emamgholizadeh, S., and Mosaedi, A. 2009. Evolution of Developing Flushing Cone during the Pressurized Flushing in Reservoir Storage. *World Academy of Science, Engineering and Technology*, 58:1107–1111.
- Meshkati, M. E., Dehghani, A. A., Sumi, T., Naser, G., and A., A. 2010. Experimental Investigation of Local Half-Cone Scouring against Dam. In (eds), A. . G., editor, *River Flow 2010*, pages 1267–1273, Dittrich, Koll.
- Miller, R. L. and Byrne, R. J. 1966. The Angle of Repose for a Single Grain on a Fixed Rough Bed. *Sedimentology*, 6(4):303–314.
- Morris, G. L. and Fan, J. 1997. *Reservoir Sedimentation Handbook: Design and Management of Dams, Reservoirs, and Watersheds for Sustainable Use*. McGraw-Hill, New York.
- Olsen, N. R. 1994. SSIIM: A Three-Dimensional Numerical Model for Simulation of Water and Sediment Flow. In *HYDROSOFT 94*, Porto Carras, Greece.
- Olsen, N. R. 1999. Two-dimensional numerical modelling of flushing processes in water reservoirs. *Journal of Hydraulic Research*, 37(1):3–16.
- Ouriemi, M., Aussillous, P., and Guazzelli, E. 2009. Sediment Dynamics. Part 1. Bed-Load Transport by Laminar Shearing Flows. *Journal of Fluid Mechanics*, 636:295–319.
- Papanicolaou, A. N., Elhakeem, M., and Krallis, G. 2008. Sediment Transport Modelling Review: Current and Future Developments. *Journal of Hydraulic Engineering*, 134(1):1–14.

- Patankar, N. A., Singh, P., Joseph, D. D., Glowinski, R., and Pan, T.-W. 2000. A New Formulation of the Distributed Lagrange Multiplier/Fictitious Domain Method for Particulate Flows. *International Journal of Multiphase Flow*, 26(9):1509–1524.
- Pettijohn, F. J. 1975. *Sedimentary Rocks*. Harper and Row, New York.
- Pope, S. B. 2000. *Turbulent Flows*. Cambridge University Press.
- Powell, D. N. 2007. *Sediment Transport Upstream of Orifices*. PhD thesis, Graduate School of Clemson University, U.S.A.
- Quartier, L., Andreotti, B., Douady, S., and Daerr, A. 2000. Dynamics of a Grain on a Sandpile Model. *Physical Review E*, 62(6):8299.
- Rajaratnam, N. and Humphries, J. A. 1982. Free Flow Upstream Of Vertical Sluice Gates. *Journal of Hydraulic Research*, 20(5):427–437.
- Raudkivi, A. J. 1998. *Loose Boundary Hydraulics*. A.A. Balkema.
- Rice, M., Willetts, B., and McEwan, I. 1995. An Experimental Study of Multiple Grain-Size Ejecta Produced by Collisions of Saltating Grains with a Flat Bed. *Sedimentology*, 42(4):695–706.
- Rouse, H. 1936. *Fluid Mechanics for Hydraulic Engineers*. McGraw Hill, New York.
- Rouse, H. 1937. Modern Conceptions of Mechanics of Turbulence. *American Society of Civil Engineers*, 102:463–543.
- Rubey, H. 1933. Settling Velocities of Gravel, sand and Silt Particles. *American Journal of Sciences*, 225:325–338.
- SANRAL 2013. *Drainage Manual*. The South Africa National Road Agency, Pretoria.
- Scheuerlein, H. 1993. Estimation of Flushing Efficiency in Silted Reservoir. In *Proceeding of The International Conference on Hydro-Science an Engineering*, Washington, DC.
- Scheuerlein, H. 2004. Numerical and Physical Modelling Concerning the Removal of Sediment Deposits from Reservoirs. In Yazdandoost, F. and Attari, J., editors, *Hydraulics of Dams and River Structures*, pages 245–254. Balkema. A. A.
- Schmidt, R. 1980. Threshold Wind-Speeds and Elastic Impact in Snow Transport. *Journal of Glaciology*, 26:453–467.

- Schneiderbauer, S. 2012. Illustrative Experiments of the Erosion of Sand and Accompanying Theoretical Considerations. *Physics Education*, 47(6):693.
- Schneiderbauer, S. and Pirker, S. 2010. Modeling Erosion and Sedimentation of a Packed Bed by Immersed Boundary (IB) and Arbitrary Lagrangian Eulerian (ALE) Methods. In Curtis, J. S. and Balachandar, S., editors, *Proceedings of the International Conference on Multiphase Flow*, page 6, Tampa, Florida.
- Schneiderbauer, S. and Pirker, S. 2014. Immersed Boundary (IB) and Arbitrary Lagrangian Eulerian (ALE) Methods for Modeling Erosion and Sedimentation of a Packed Bed in the Vicinity of an Obstacle. Christian Doppler Laboratory on Particulate Flow Modelling, Department of Particulate Flow Modelling, Johannes Kepler University, Austria.
- Schneiderbauer, S. and Prokop, A. 2011. The Atmospheric Snow-Transport Model: SnowDrift3D. *Journal of Glaciology*, 57(203):526–542.
- Shammaa, Y., Zhu, D. Z., and Rajaratnam, N. 2005. Flow Upstream of Orifices and Sluice Gates. *Journal of Hydraulic Engineering*, 131(2):127–133.
- Shao, Y. and Li, A. 1999. Numerical Modelling of Saltation in the Atmospheric Surface Layer. *Boundary-Layer Meteorology*, 91(2):199–225.
- Shen, H. W. 1999. Flushing Sediment Through Reservoirs. *Journal of Hydraulic Research*, 37(6):743–757.
- Simons, D. B. and Sentürk, F. 1992. *Sediment Transport Technology: Water and Sediment Dynamics*. Water Resources Publications: Littleton, Colorado.
- Spasojevic, M. and Holly, F. M. 1990. Mobed2: Numerical Simulation of Two-Dimensional Mobile-Bed Processes. Technical Report 344, Iowa Institute of Hydraulic Research, University of Iowa, Iowa.
- Stephan, K. 2013. Hydropower Dam Sediment Flushing Outlet. Bachelor's degree final report, University of Stellenbosch.
- Stull, R. B. 1988. *An Introduction to Boundary Layer Meteorology*, volume 13. Springer.
- Sumi, T., Okano, M., and Takata, Y. 2004. Reservoir Sedimentation Management with Bypass Tunnels in Japan. In *Proceedings of the Ninth International Symposium on River Sedimentation*, volume 2, pages 1036–1043.

- Talebeydokhti, N. and Naghshineh, A. 2004. Flushing Sediment through Reservoir. *Iranian Journal of Science & Technology*, 28(B1):119–136.
- Thomas, W. A. and McAnally, W. H. 1985. *Users Manual for the Generalised Computer Program System Open-Channel Flow and Sedimentation, TABS-2*. U.S. Army Corps of Engineers, Vicksburg, Miss.
- Uhlmann, M. 2005. An Immersed Boundary Method with Direct Forcing for the Simulation of Particulate Flows. *Journal of Computational Physics*, 209(2):448–476.
- U.S Army Corps of Engineers 1972. *HEC-6 Scour and Deposition in Rivers and Reservoirs, Users Manual*. Hydrologic Engineering Centre, Davis, California.
- USBR 1987. *Design of Small Dam*. United States Bureau of Reclamation: Government Printing Office, Washington, D. C.
- Van Rijn, L. 1984a. Sediment Transport, Part II: Suspended Sediment Load Transport. *Journal of Hydraulic Engineering*, 110(11):1613–1641.
- Van Rijn, L. 1984b. Sediment Transport, Part I: Bed Load Transport. *Journal of Hydraulic Engineering*, 110(10):1431–1456.
- Van Rijn, L. C. 1981a. Entrainment of Fine Sediment Particles; Development of Concentration Profiles in a Steady, Uniform Flow without Initial Sediment Load. Technical Report M1531, Part II, Delft Hydr. Lab.
- Van Rijn, L. C. 1981b. The Development of Concentration Profiles in a Steady, Uniform Flow without Initial Sediment Load. In *Proc. of IAHR Workshop on Particle Motion and Sediment Transport Measurement Techniques and Experimental Results*, pages 5.1–5.8.
- Van Rijn, L. C. 1986. Mathematical Modeling of Suspended Sediment in Non-uniform Flows. *Journal of Hydraulic Engineering, ASCE*, 112:433–455.
- Van Rijn, L. C. and Tan, G. L. 1985. Sutrench Model: Two-Dimensional Vertical Mathematical Model for Sedimentation in Dredged Channels and Trenches by Currents and Waves. In *Rijkswaterstaat communications*, volume 41.
- Werner, B. and Haff, P. 1988. The Impact Process in Aeolian Saltation: Two-Dimensional Simulations. *Sedimentology*, 35(2):189–196.

-
- White, B. R. and Schulz, J. C. 1977. Magnus Effect in Saltation. *Journal of Fluid Mechanics*, 81(03):497–512.
- White, W. R., Milli, H., and Crabbe, A. D. 1975. Sediment Transport Theories: a review. In *Proc. Institute of Civil Engineers*, volume 59(Part 2), pages 265–292.
- Wu, W. 2001. CCHE2D Sediment Transport Model. Technical Report NCCHE-TR-2001-3, National Center for Computational Hydroscience and Engineering (NCCHE).
- Wu, W. 2008. *Computational River Dynamics*. Taylor & Francis/Balkema, National Center of Computational Hydroscience and Engineering, University of Mississippi, MS, USA.
- Wu, W. and Viera, D. A. 2002. One-Dimensional Channel Network Model CCHE1D. Version 3.0. Technical Report NCCHE-TR-2002-1, School of Engineering, University of Mississippi.
- Yang, C. and Molinas, A. 1982. Sediment Transport and Unit Stream Power Function. *Journal of Hydraulic Division. American Society of Civil Engineers*, 108(HY6):774–793.
- Yang, C. and Simoes, F. J. 2003. *GSTARS3 Reference Manual*. Technical Service Centre, U.S. Bureau of Reclamation, Denver.
- Yang, C. T. 2003. *Sediment Transport : Theory and Practice*. Krieger Publishing Company, Malabar, Florida.

Appendix A. Experimental Test Results

A.1 Experimental Results for Test 2



Figure A.1: Scour hole for Test 2

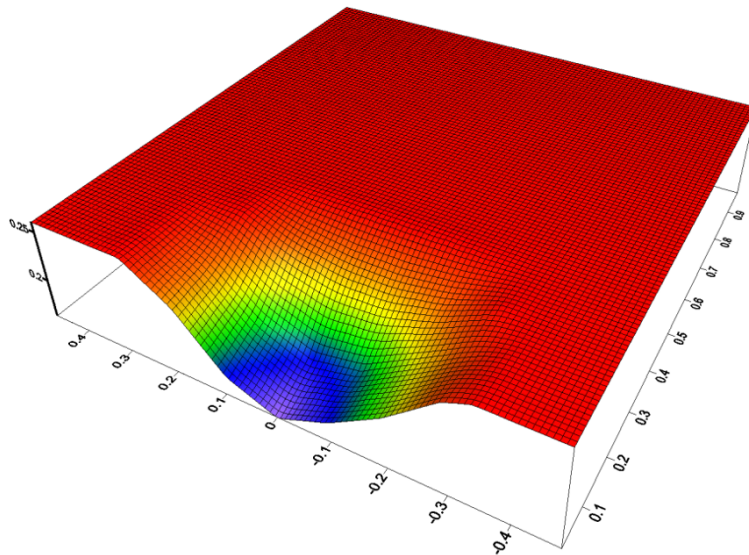


Figure A.2: 3D bed surface mapping for Test 2

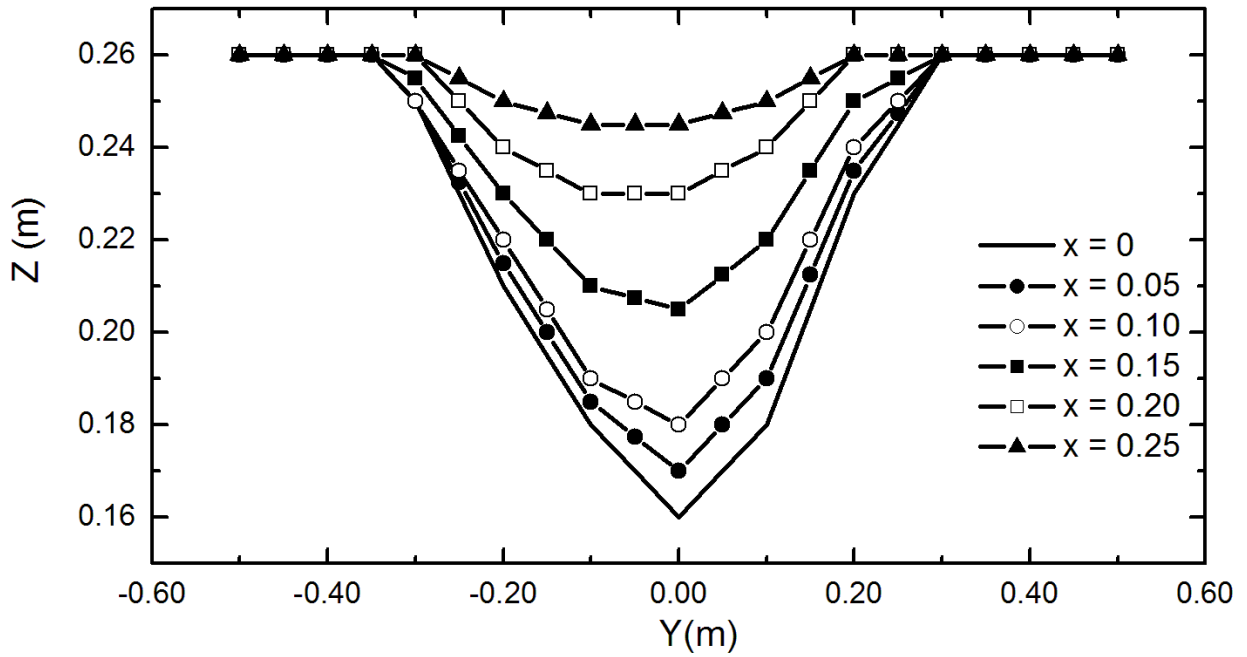


Figure A.3: Observed lateral cross sections of the scour hole for Test 2

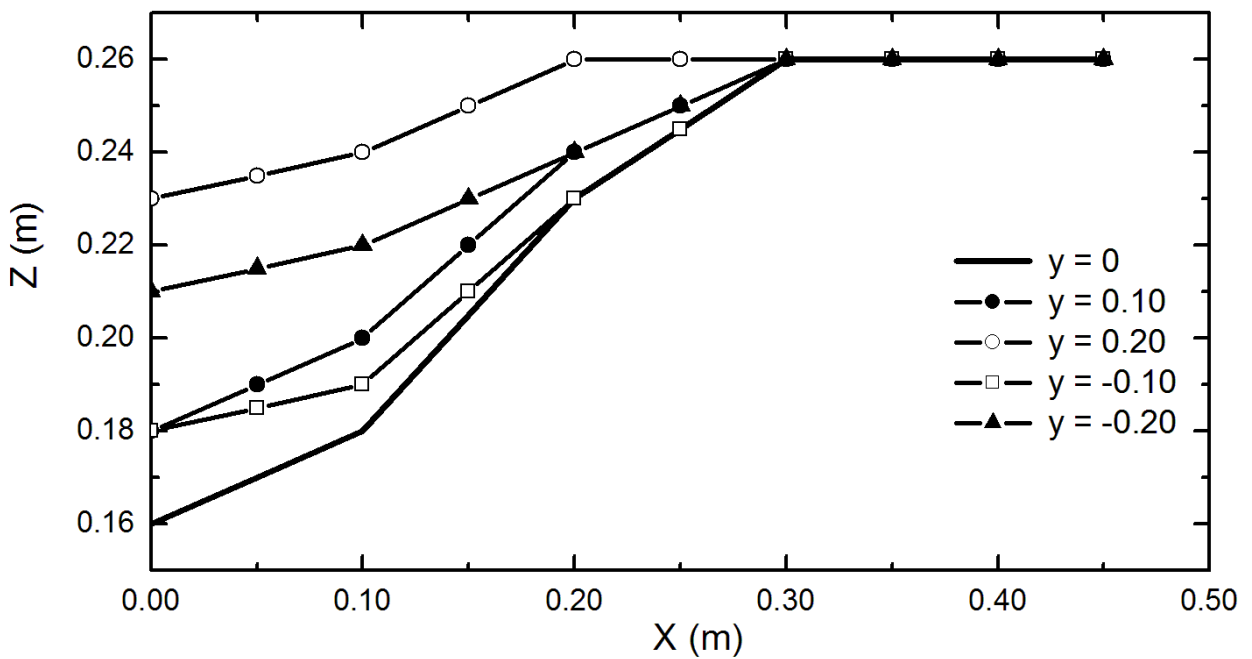


Figure A.4: Observed longitudinal cross sections of the scour hole for Test 2

A.2 Experimental Results for Test 3



Figure A.5: Scour hole for Test 3

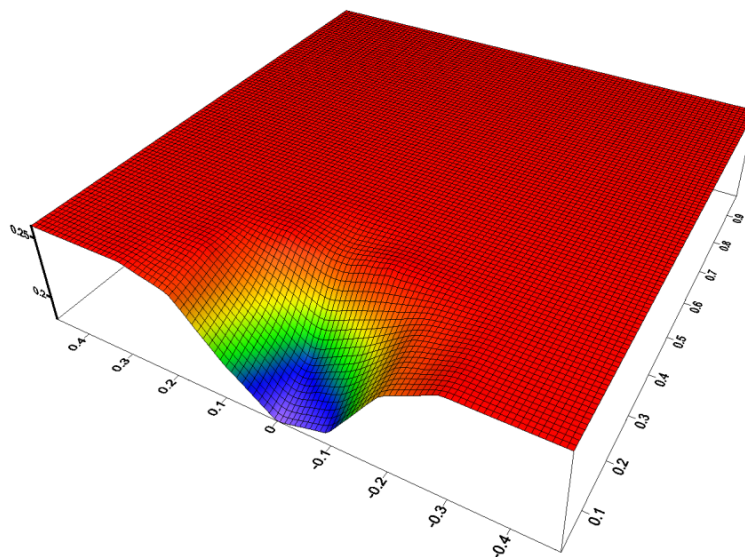


Figure A.6: 3D bed surface mapping for Test 3

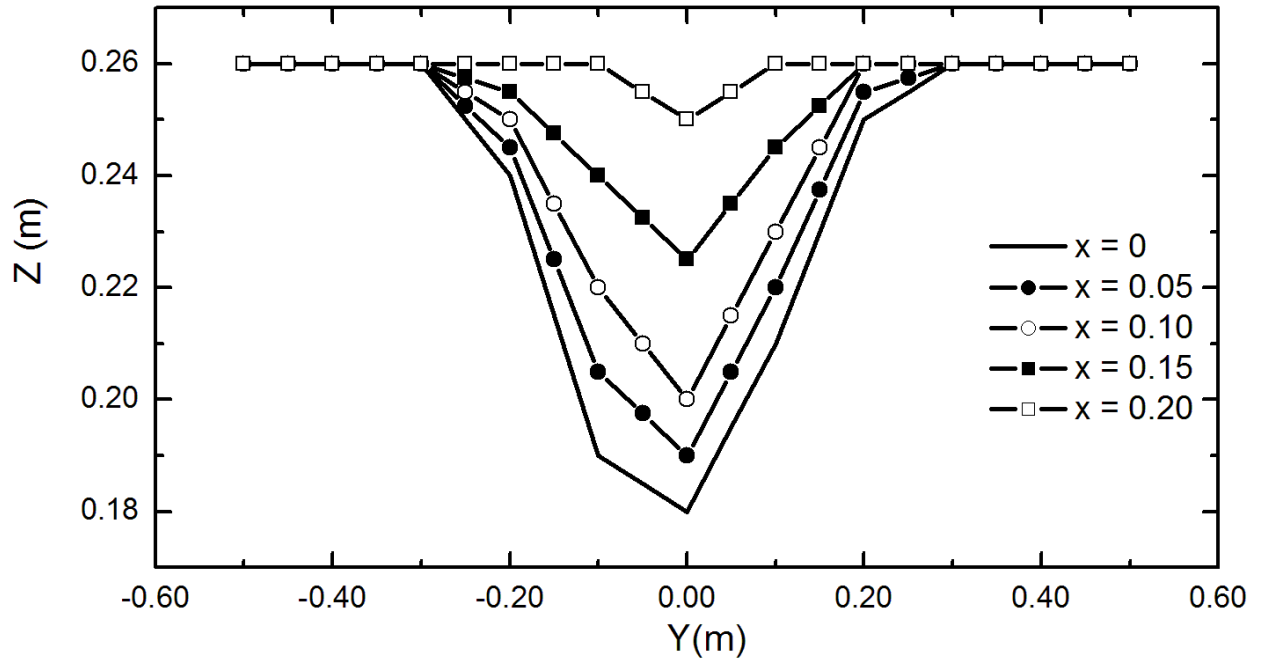


Figure A.7: Observed lateral cross sections of the scour hole for Test 3

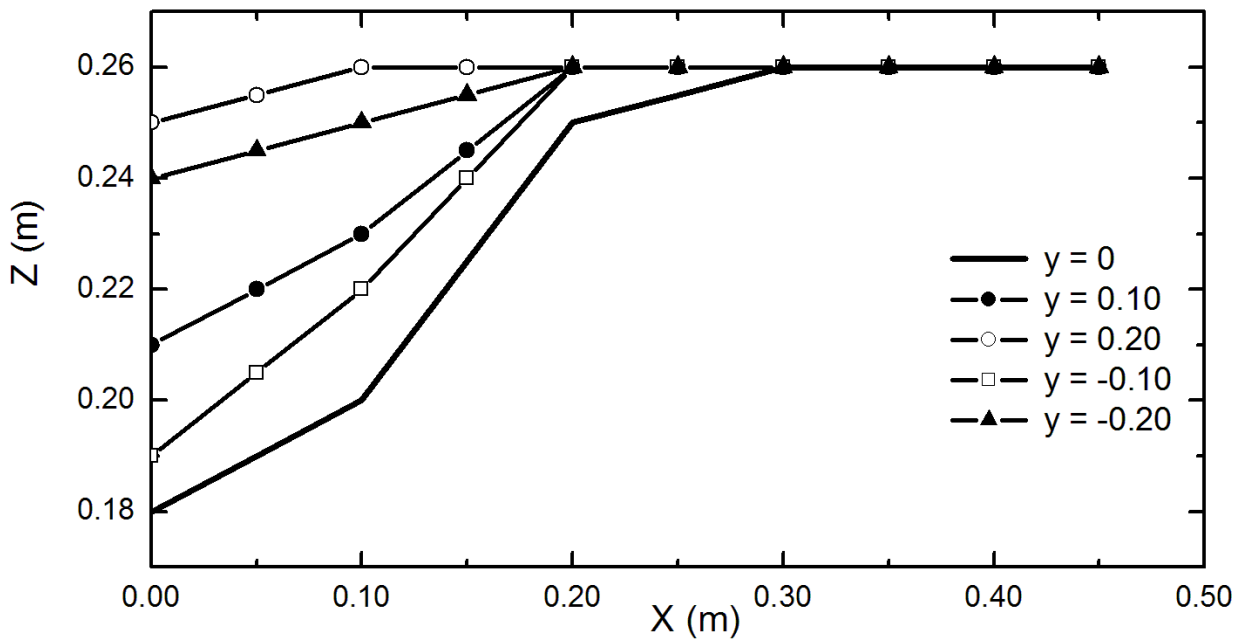


Figure A.8: Observed longitudinal cross sections of the scour hole for Test 3

Appendix B. Simulation Test Results

B.1 Simulation Results for Test 2

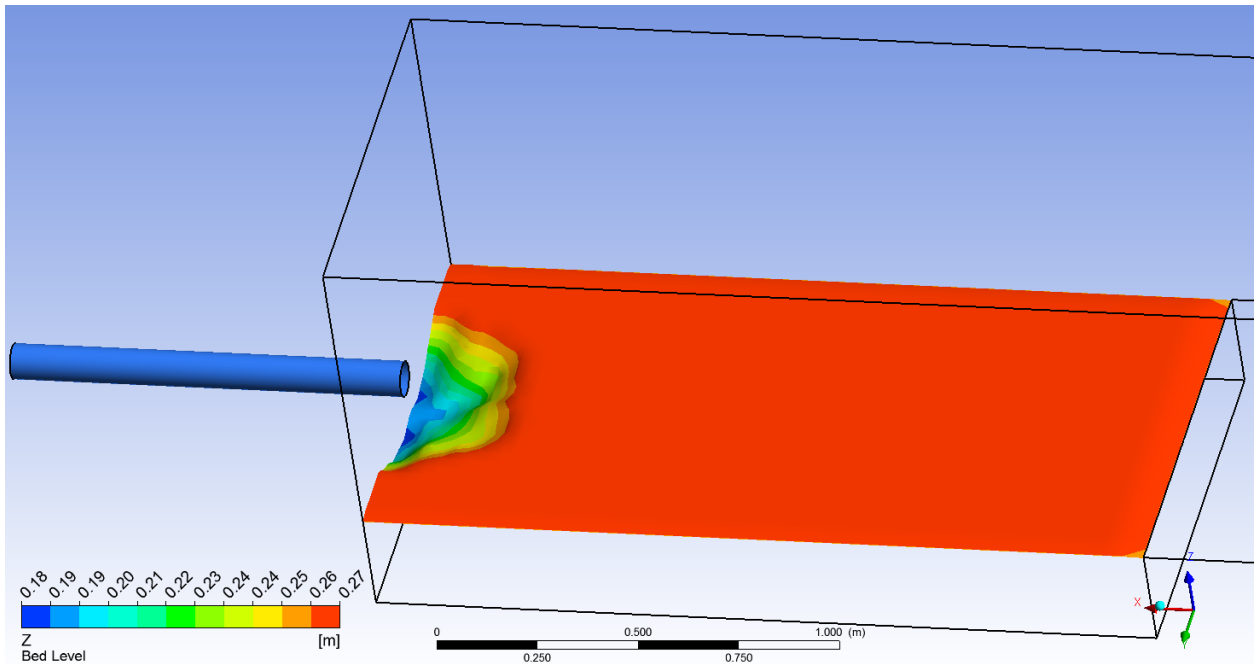


Figure B.1: Simulated scour hole for Test 2

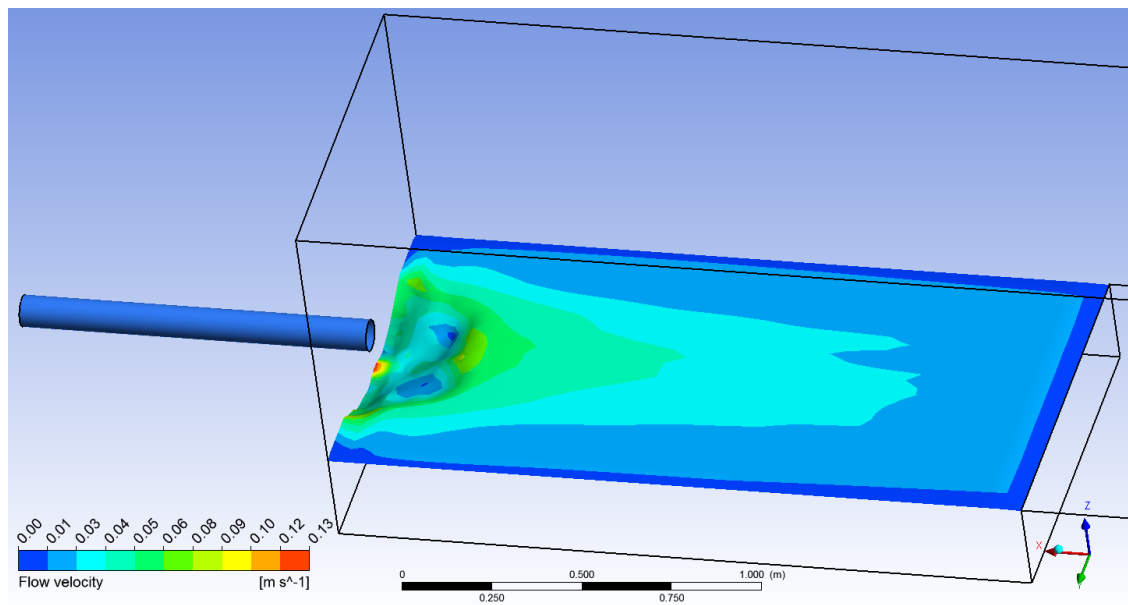


Figure B.2: Contours of simulated flow velocity for Test 2

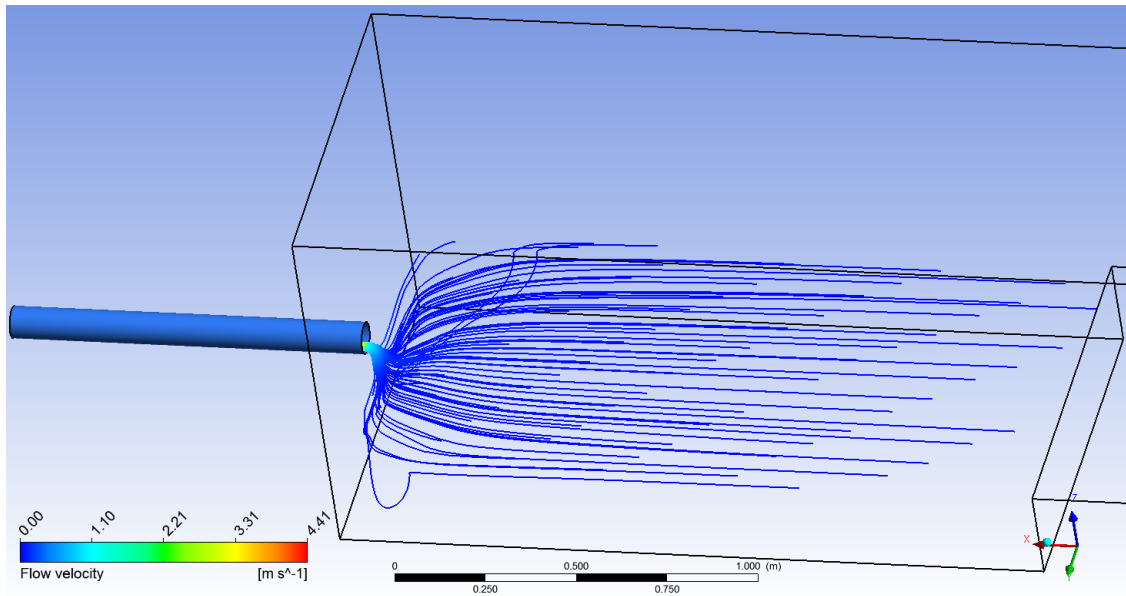


Figure B.3: Simulated flow streamline for Test 2

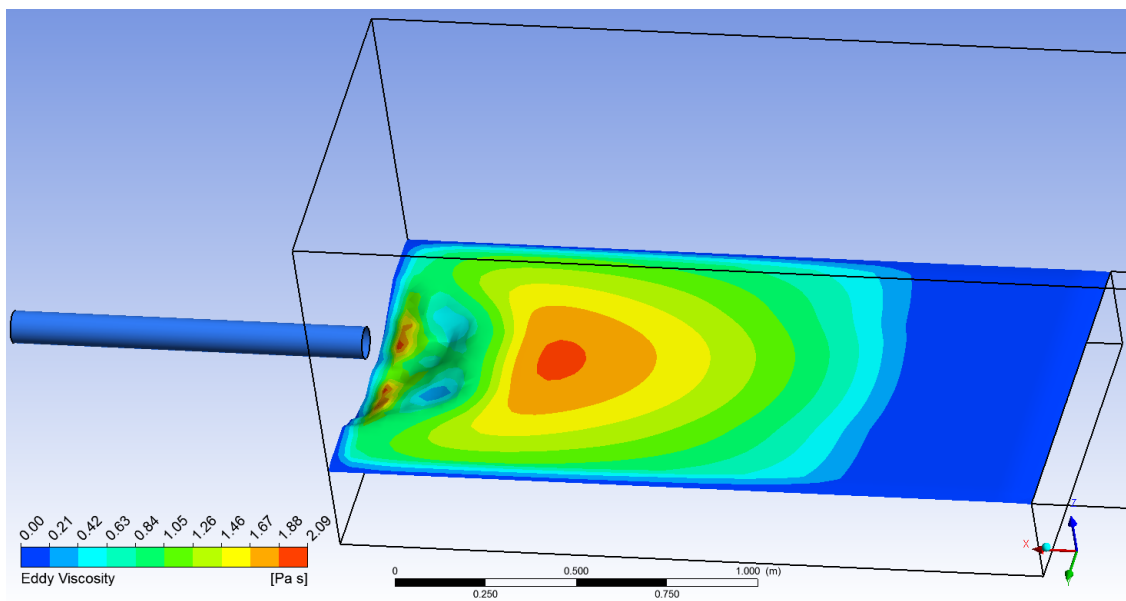


Figure B.4: Contours of the simulated eddy viscosity for Test 2

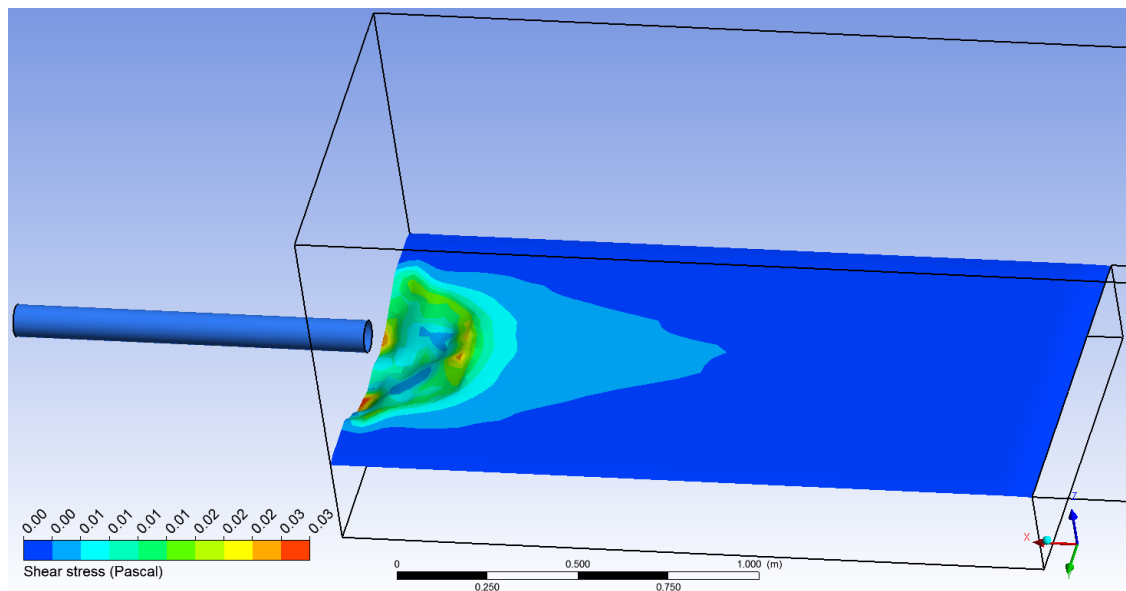


Figure B.5: Contours of the simulated bed shear stress for Test 2

B.2 Simulation Results for Test 3

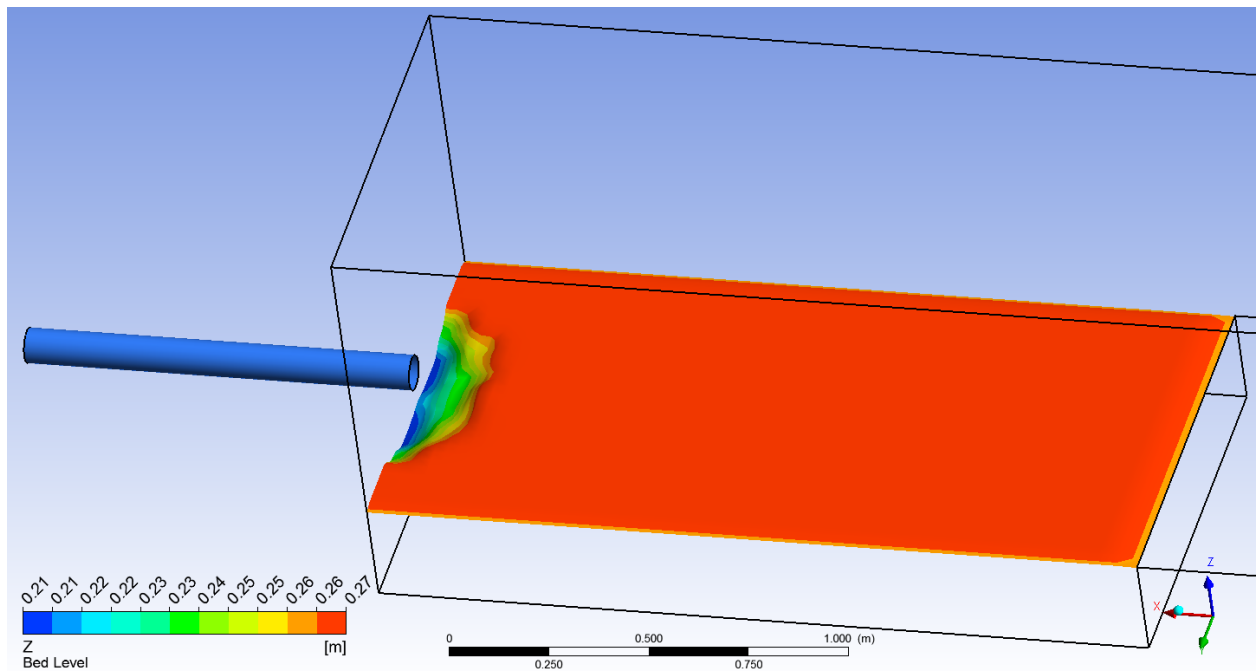


Figure B.6: Simulated scour hole for Test 3

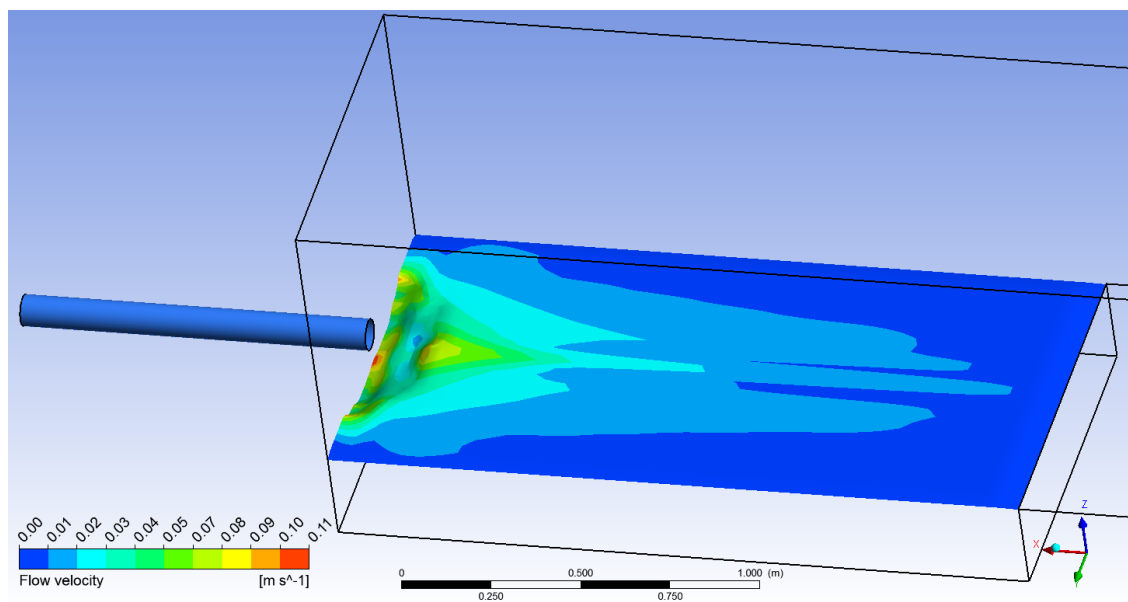


Figure B.7: Contours of simulated flow velocity for Test 3

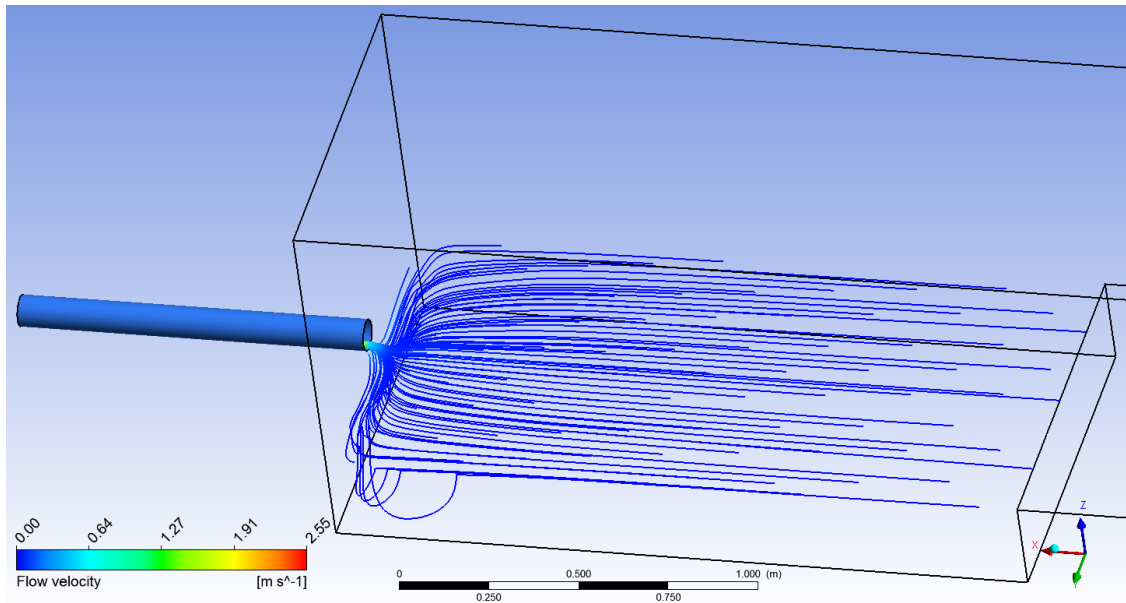


Figure B.8: Simulated flow streamline for Test 3

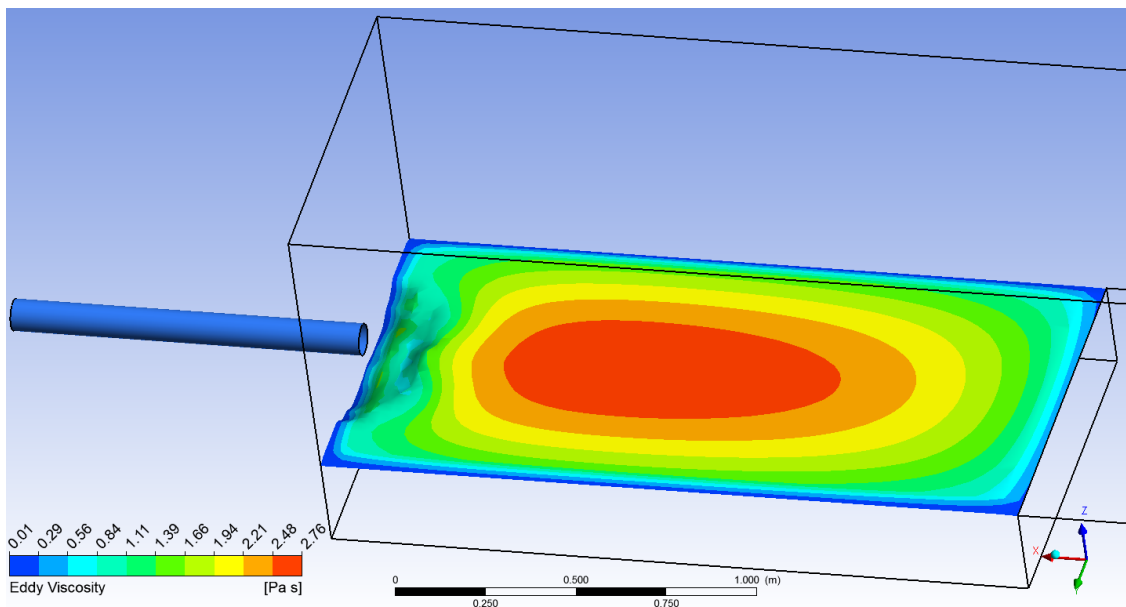


Figure B.9: Contours of the simulated eddy viscosity for Test 3

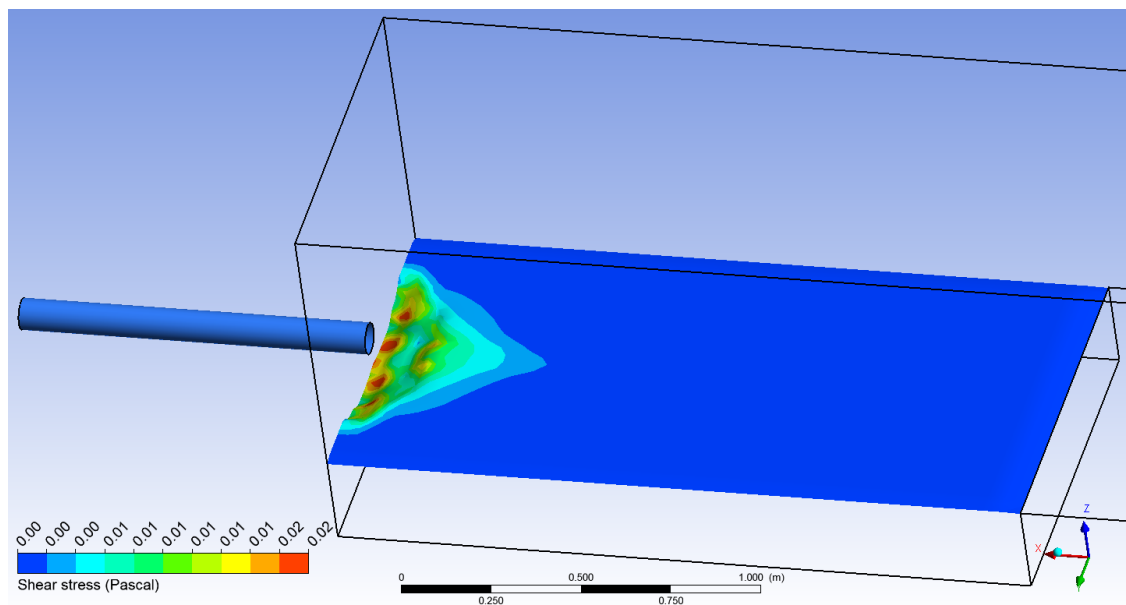


Figure B.10: Contours of the simulated bed shear stress for Test 3

B.3 Simulation Results for Test 4

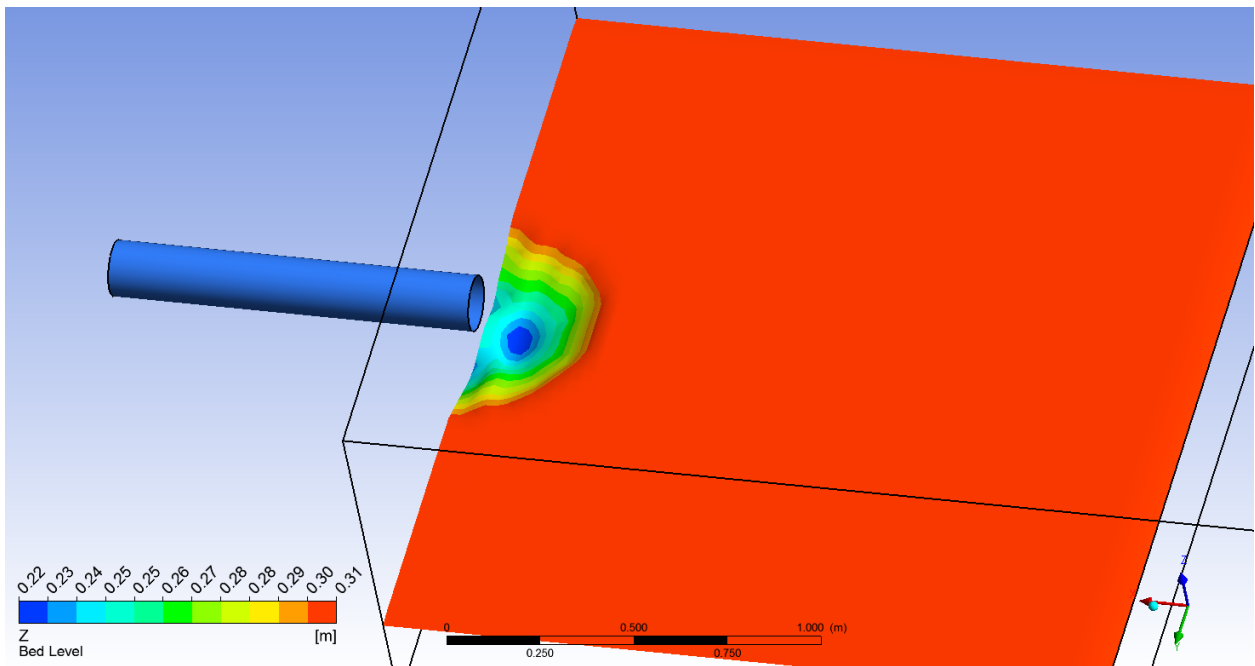


Figure B.11: Simulated scour hole for Test 4

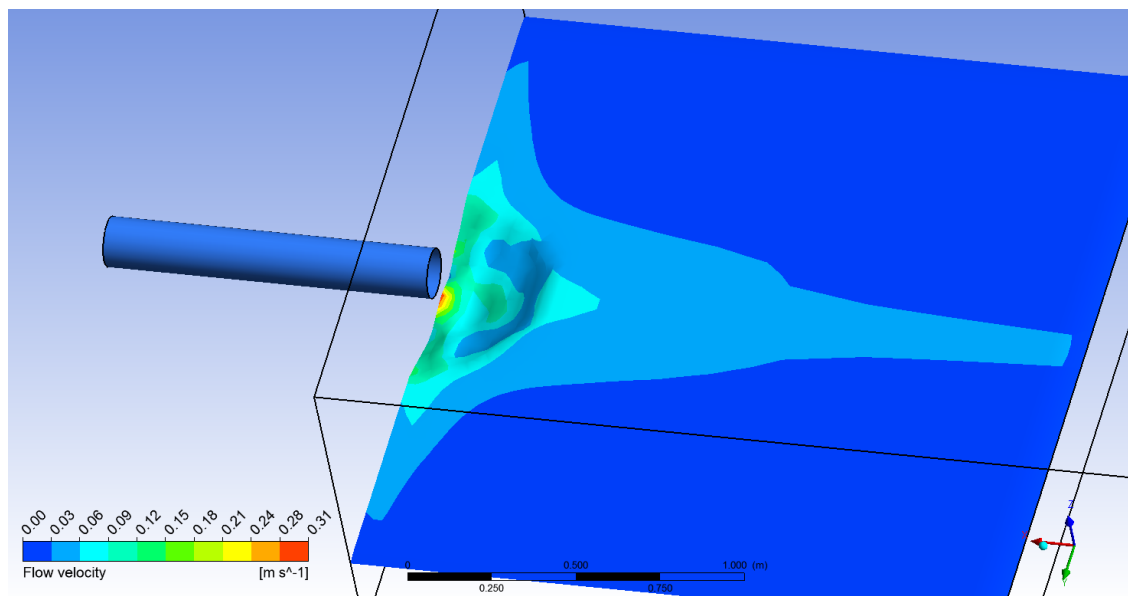


Figure B.12: Contours of simulated flow velocity for Test 4

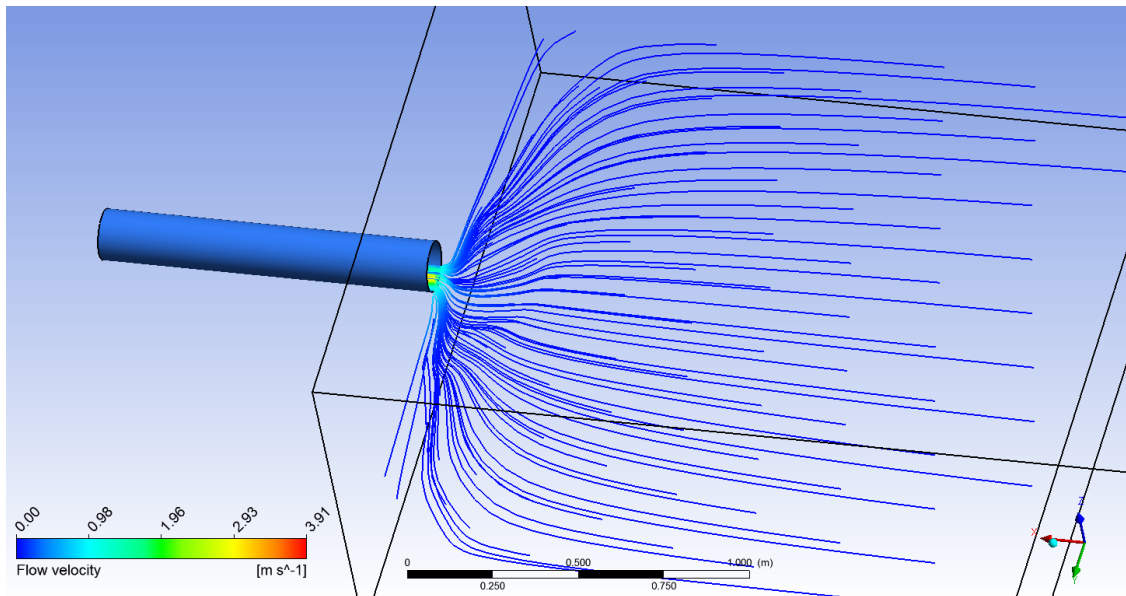


Figure B.13: Simulated flow streamline for Test 4

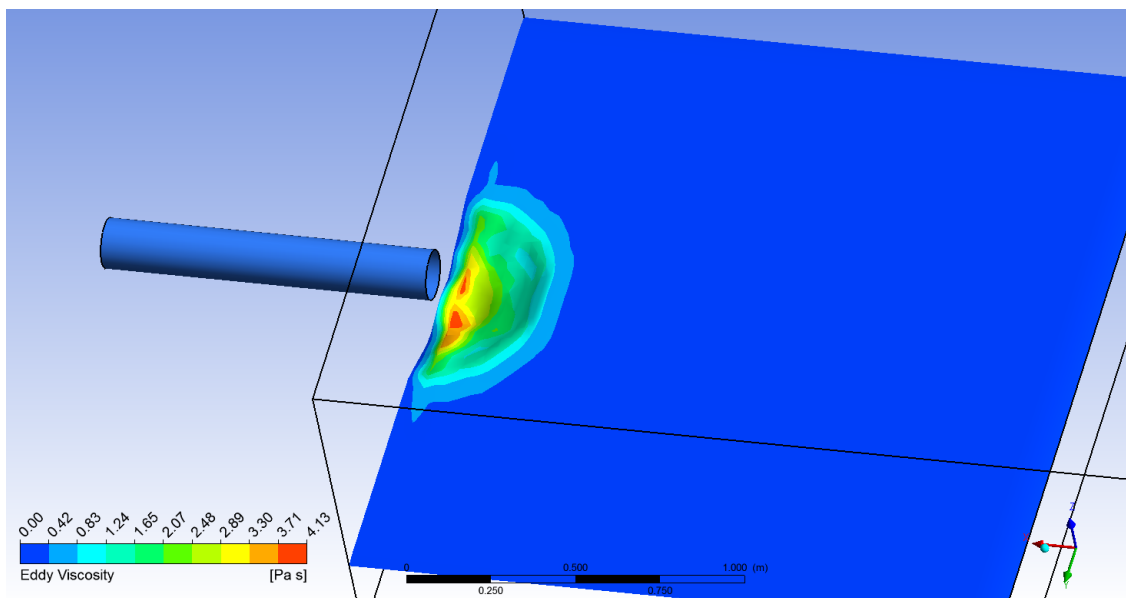


Figure B.14: Contours of the simulated eddy viscosity for Test 4

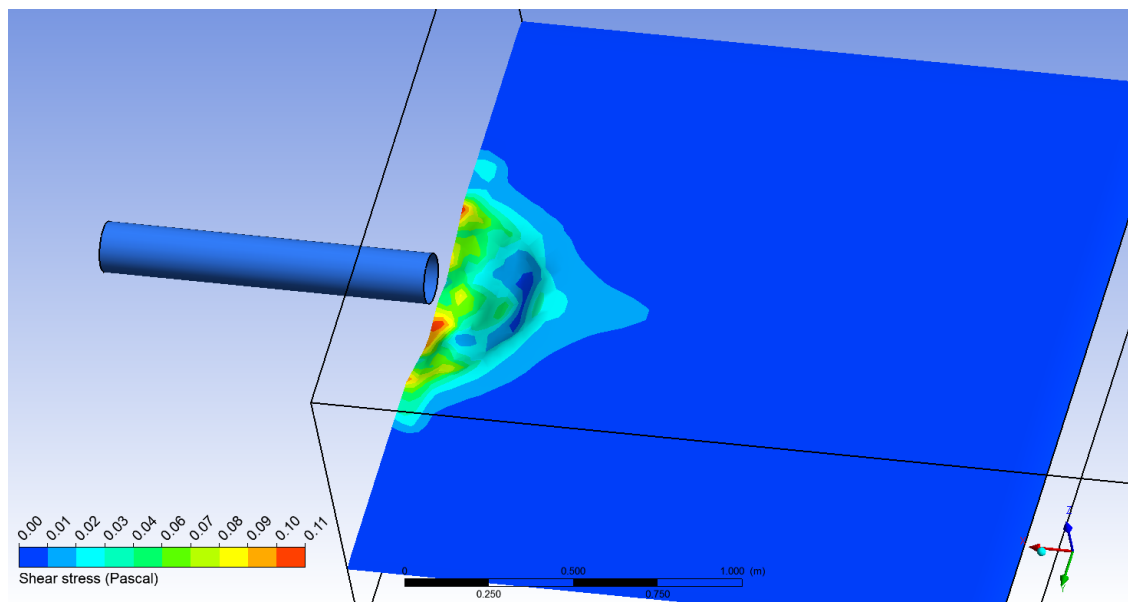


Figure B.15: Contours of the simulated bed shear stress for Test 4